18

Applications of Synchrotron-Based Spectroscopic Techniques in Studying Nucleic Acids and Nucleic-Acid-Based Nanomaterials

Peiwen Wu[1], Yang Yu[2], Claire E. McGhee[3], Li H. Tan[3], Abhijit Mishra[4], Gerard Wong[5], and Yi Lu[1,3]

[1] *University of Illinois at Urbana-Champaign, Department of Biochemistry, 600 S Mathews Ave, Urbana, IL 61801, USA*
[2] *Chinese Academy of Sciences, Tianjin Institute of Industrial Biotechnology, 32 W 7th Ave, Tianjin Airport Economic Area, Tianjin 300308, China*
[3] *University of Illinois at Urbana-Champaign, Department of Chemistry, 505 S Mathews Ave, Urbana, IL 61801, USA*
[4] *Indian Institute of Technology Gandhinagar, Department of Materials Science and Engineering, Palej, Gandhinagar, Gujarat 382355, India*
[5] *University of California, Department of Bioengineering, Department of Chemistry & Biochemistry, California NanoSystems Institute, 420 Westwood Plaza, Los Angeles, CA 90095, USA*

18.1 Introduction

The history of synchrotrons can be traced back to 1873, when James Clerk Maxwell came up with the theory of electromagnetism that changed our understanding of light. Since its discovery in 1895, X-ray has enjoyed fast development in physical, medical, and biological research. To expand the field of applications even further to include areas such as high-energy physics, scientists and engineers around the world have designed and realized many ways to accelerate particles, including synchrotron radiation facilities that provide researchers with extremely high-flux electromagnetic radiation, at broad energy ranges from the infrared through the ultraviolet and into the X-ray region. Synchrotron light sources have enabled tremendous breakthroughs in physics, chemistry, and biology, especially structural biology [1]. Thousands of biomolecular structures are deposited in the Protein Data Bank every year, and more than 80% of them have been determined with the use of synchrotron-based methods.

A major class of biomolecules is nucleic acids, which play central roles in the storage and transfer of genetic information. Even though nucleic acids were first discovered in 1869 by Johannes Friedrich Miescher, the structure of nucleic acids remained a mystery until X-ray diffractograms of DNA crystals were recorded by Rosalind Franklin and the double-helix model was proposed by Watson and Crick in 1953. The characterization of the double helical structure of DNA paved the way for explaining how genetic information is stored and then copied to the next generation. With the discoveries of various types of RNA molecules with distinct functions, such as messenger RNA, transfer RNA, noncoding RNA, small

Synchrotron Radiation in Materials Science: Light Sources, Techniques, and Applications, First Edition. Edited by Chunhai Fan and Zhentang Zhao.
© 2018 Wiley-VCH Verlag GmbH & Co. KGaA. Published 2018 by Wiley-VCH Verlag GmbH & Co. KGaA.

interfering RNA, ribozyme, and ribosome, it was revealed that RNA molecules can not only serve as a template for protein synthesis, but also form complex three-dimensional (3D) structures for a wide range of functions, including protein synthesis, enzymatic reactions, and gene regulation. High-resolution structures of these RNA molecules play a key role in furthering our understanding of the structural features and mechanisms behind these functions.

In addition to the DNA and RNA molecules discovered in nature, systematic evolution of ligands by exponential enrichment (SELEX), or *in vitro* selection [2–5], has been used to obtain RNA or DNA molecules in test tubes that can either bind numerous molecules selectively (called aptamers) or can catalyze specific reactions (called ribozymes for catalytic RNA or deoxyribozymes or DNAzymes for catalytic DNA) [6–14]. Many of these aptamers, ribozymes, and DNAzymes have been transformed into sensors [15] based on fluorescence [16–21], colorimetry [22–24], electrochemistry [25], or enzymatic activity [26–28]. More recently, due to the intrinsic programmability of DNA caused by precise base-pairing with complementary strands, DNA molecules are emerging as promising candidates to be used in various areas in nanotechnology, such as DNA-directed self-assembly of colloidal nanoparticles [29, 30], DNA origami [31–35], microchips, and DNA-based computation [36–39]. Given the wide variety of DNA and RNA molecules and their diverse functions, it is important to characterize their structures in order to understand them. It is not surprising that synchrotron-based techniques, such as X-ray spectroscopy, X-ray footprinting, and small-angle X-ray scattering (SAXS) play key roles in achieving this goal (Figure 18.1).

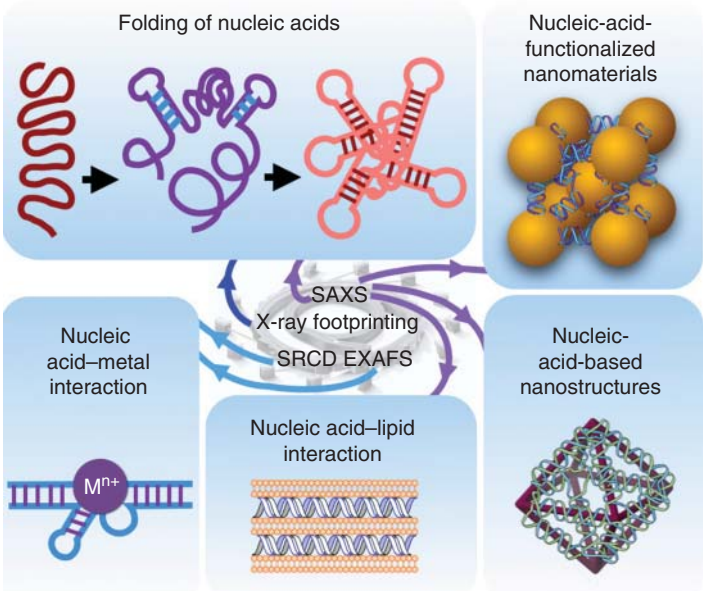

Figure 18.1 Synchrotron-based techniques for characterizing nucleic acids and nucleic-acid-based nanomaterials.

In this chapter, we summarize the applications of synchrotron-based spectroscopic techniques used to characterize nucleic acids. Instead of giving a comprehensive review on numerous high-resolution crystal structures of nucleic acids obtained using a synchrotron light source, we emphasize the different types of synchrotron-based spectroscopic studies that helped elucidate the properties of nucleic acids, including electronic structures, electrostatic properties, folding pathways, overall 3D nanostructures, and crystal lattices in the DNA-directed self-assembly of nanoparticles.

18.2 Synchrotron-Based Spectroscopic Techniques in the Characterization of Nucleic Acids

Synchrotron facilities can provide electromagnetic radiation ranging from infrared to X-ray with high brightness, high collimation, and wide tunability [40]. These properties make synchrotron radiation an ideal light source for a number of spectroscopic applications. Among different synchrotron-based techniques [41], X-ray absorption spectroscopy (XAS), X-ray emission spectroscopy (XES), X-ray photoelectron spectroscopy (XPS), SAXS, and synchrotron radiation circular dichroism (SRCD) are widely used in characterizing conformations and electronic structures of nucleic acids.

X-rays are often described in terms of the energy they carry, which can range from less than 1 keV to greater than 100 keV. The X-ray with energies above 10 keV is often referred to as the hard X-ray, while the lower energy X-ray is referred to as the soft X-ray. When the absorption coefficient of a given element is measured over a range of excitation energies, a sharp increase in the absorption coefficient at a certain energy level can be observed. Such an absorption increase is referred to as the absorption edge, which occurs when the core electron absorbs energy equal to or greater than its binding energy. The naming of the edges depends on which shell the core electron is ejected from, with the principal quantum number $n = 1–3$ corresponding to the *K*-, *L*-, and *M*-edge, respectively. From the edge to about 50 eV above the edge is the X-ray absorption near-edge structure (XANES) region, while an extended X-ray absorption fine structure (EXAFS) region extends to approximately 1 keV above the edge (Figure 18.1). Near-edge X-ray absorption fine structure (NEXAFS) deals with analysis of soft X-ray 1s XANES spectra and is more relevant for nucleic acid research [42]. Analyses of pre-edge, edge, XANES, and EXAFS regions reveal information about the electronic structures and the local metal coordination information of the samples [43, 44].

The fundamental principle of XAS and XES is based on the ability of X-ray to excite core electrons from an atom (Figure 18.2). Under high-intensity X-ray radiation, atomic core energy level electrons in the material can absorb X-ray photons and be promoted to a higher unoccupied energy level, leaving a core hole. XAS measures the fraction of X-ray photons that are absorbed by the sample. When an outer-shell electron decays to fill the core hole, a photon will be emitted. XES captures the energy and intensity of emitted photons. Both XAS and XES are

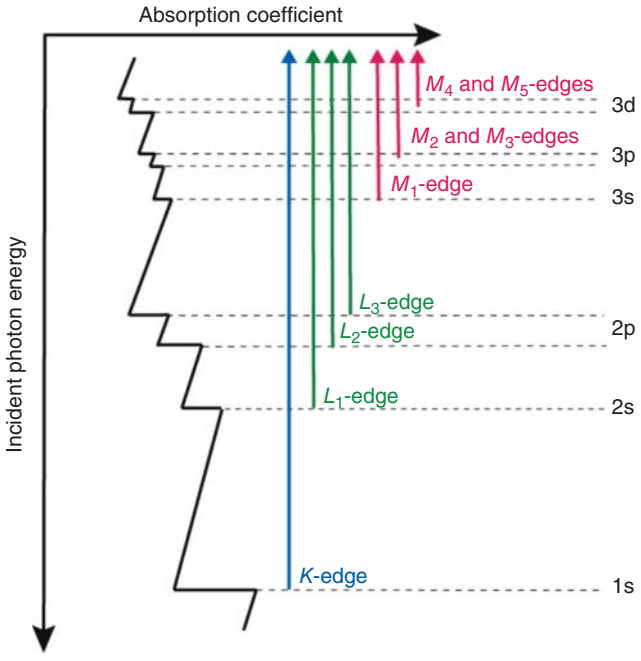

Figure 18.2 The relationship between energy transitions and X-ray absorption edges. (Rehr 2000 [45]. Reproduced with permission of John Wiley & Sons.)

element-specific and site-specific, and they reveal the electronic structures of the samples [44, 46]. XPS, on the other hand, studies energy distribution of electrons emitted from X-ray-irradiated materials [47–49]. From this measurement, element composition, chemical formula, and the electronic state of materials can be deduced.

18.2.1 Use of XAS and XES Spectroscopy in Studying Electronic Structures of Nucleobases

DNA molecules have been used in constructing various nanodevices such as molecular wires [50], and therefore their electronic properties are essential for the design and optimization of these devices [51, 52]. In nature, DNA contains four nucleobases, adenine (A), guanine (G), cytosine (C), and thymine (T). To gain a better understanding of the electronic properties of DNA molecules, the chemical structures of nucleobases have been extensively characterized using XAS and XES. By determining the transitions from the inner-shell atomic orbitals to virtual molecular orbitals, information about the electronic structures of a particular element of interest in a nucleobase can be readily obtained. As nucleobases are composed of light atoms, mainly carbon, nitrogen, and oxygen, with low electron-binding energies (284 eV for carbon, 410 eV for nitrogen, and 543 eV for oxygen), soft X-ray is often used to characterize nucleobases. The nitrogen atom, as the only element that appears exclusively in nucleobases but not in the ribose or the phosphate backbone, provides the clearest fingerprint of

DNA, and has therefore caught more attention in the early work on nucleobase characterization [53].

Kirtley *et al.* used XANES to study the electronic environment of nitrogen in different nucleobases, nucleotides, polynucleotides, and calf thymus DNA [54]. In their study, they changed the chemical environment around nitrogen atoms by introducing oxygen or halogen substitutions on the carbon atoms of the aromatic ring to modify the ring. Spectral perturbations were observed in these cases, revealing that the fine structures shown in the photoabsorption spectrum of DNA near the nitrogen *K*-edge depended highly on the chemical structure of the nitrogen atom. Moewes *et al.*, on the other hand, used carbon *K*-edge XAS and XES to study electronic structures of B-DNA and its four nucleobases [55]. In addition, they performed a systematic study to investigate how different buffer conditions might affect the electronic structure of B-DNA using XAS and XES. On the other hand, MacNaughton *et al.* carried out a more comprehensive study on the four nucleobases by obtaining XAS and XES spectra for all three elements (C, N, and O) [56]. Combined with theoretical calculations, they were able to identify the main energy transitions of these nucleobases in the XAS and XES spectra. By comparing the XES and XAS experimental data on a common energy axis, the energy gap between the highest occupied molecular orbital (HOMO) and the lowest unoccupied molecular orbital (LUMO) was determined for all four bases. Furthermore, Zubavichus *et al.* reported a detailed analysis of high-quality NEXAFS spectra of five nucleotide bases, including three pyrimidine (cytosine, uracil, and thymine) and two purine (adenine and guanine) for carbon, nitrogen, and oxygen *K*-edges [57]. All these studies have provided electronic structures of the nucleobases and reference data that can be useful for the analysis of XAS or XES spectra of DNA molecules with different sequences, as discussed in the next section.

18.2.2 XAS and XES in Characterizing Electronic Structures of Double-Stranded DNA

Although the DNA molecules use nucleotides as their basic building blocks, interactions between nucleobases, such as hydrogen bonding, make their electronic structures different from those of an individual nucleotide. Therefore, it is not surprising that the spectra of double-stranded DNA (dsDNA) exhibited significant differences from the sum of individual spectrum of the nucleotides, supporting the hypothesis that the interactions affect the electronic structure of the nucleotides [54, 55]. By studying Poly(dG)·Poly(dC) and Poly(dA)·Poly(dT) DNA duplexes separately, Hua *et al.* proposed that the spectral properties of dsDNA of mixed bases could be expressed as linear combinations of those of dG · dC and dA · dT base pairs, suggesting that hydrogen bonding, rather than stacking between base pairs, affected the electronic structure [58]. The electronic structures of the DNA molecules were found to be sensitive to their environment, since XAS and XES spectra and the HOMO–LUMO gap were found to change in different buffers [55, 59]. Several studies suggested that the HOMO–LUMO gap of a DNA duplex is closely related to charge hopping phenomenon [60–64]. Guo *et al.* and Kummer *et al.* determined that the band

gap of a DNA duplex was 2.6 eV and was associated with a transition between the π and π* orbitals [65, 66].

18.2.3 SRCD for Probing the Secondary Structure of DNA Molecules

Circular dichroism (CD) is a commonly used technique for studying the secondary structure of nucleic acids [67–71]. In order to obtain more information about the nucleic acids, the wavelength of CD has been extended to the vacuum ultraviolet (VUV) region in order to achieve stronger electron coupling between bases [68, 72]. Although advanced experimental setups were able to record CD spectra in the wavelength between 170 and 200 nm, low photon fluxes were often a limitation due to strong absorption by air, solvent, buffer, salts, and cuvette. To overcome this limitation, synchrotron radiation was used to provide high VUV flux, making it possible to obtain SRCD data with high signal-to-noise ratios [73].

Nielsen, Holm, and coworkers carried out systematic SRCD spectral studies on various types of DNA, including single-stranded DNA (ssDNA), dsDNA with different combinations of nucleobases, adenine–thymine triplex, i-motifs, and G-quadruplexes [74–78]. G-quadruplexes have been known to adopt different topologies when their structural elements are different. Figure 18.3a illustrates four common quadruplex folding motifs formed by different DNA sequences. Homologous guanine oligonucleotides $d(G)_n$ are known to form quadruplexes with four parallel strands (Figure 18.3a, A(4)), while d(G4T4G4) yields a bimolecular antiparallel G-quadruplex with diagonal loops (Figure 18.3a, B(2)). On the other hand, d(TAGGGUTAGGGT) results in a bimolecular parallel G-quadruplex with double-chain-reversal loops (Figure 18.3a, C(2)), and d(GGTTGGTGTGGTTGG) adopts a self-folded chair-type structure (Figure 18.3a, D(1)). By examining the G-quadruplexes with distinct topologies, Holm *et al.* found that the SRCD signal from a G-quadruplex was proportional to its length [75], indicating that the CD signal originated from the G quartets. As G-quadruplexes with different conformations (anti or syn) or handedness displayed similar SRCD signals, Holm *et al.* proposed that the SRCD signal was not related to the topology of the G-quadruplex.

In another study, Gao *et al.* used SRCD to monitor structural changes of DNA molecules wrapped around single-walled carbon nanotubes (SWCNTs) upon Hg^{2+} binding (Figure 18.4) [79]. The DNA molecules have been known to exhibit strong induced circular dichroism (ICD) signals when they are wrapped around SWCNTs, due to the coupling between the transition dipole moments of the optically chiral SWCNTs and the transition dipole moments of DNA. Hg^{2+}-induced extending of the DNA caused partial detachment of the DNA from the SWCNTs, resulting in a decrease of the ICD signal. By taking advantage of this property, the authors have transformed the DNA–SWCNT system into a sensor for Hg^{2+} with a nanomolar detection limit.

More recently, Brazier and coworkers characterized thermal and pH stability of i-motif constructs with different loop length using SRCD and UV [80]. It has been shown that i-motif exists in gene promoter regions and can form a quadruplex structure to modulate gene expression. Results from SRCD and UV suggest that shorter loops give more stable structures than longer loops. In addition, the

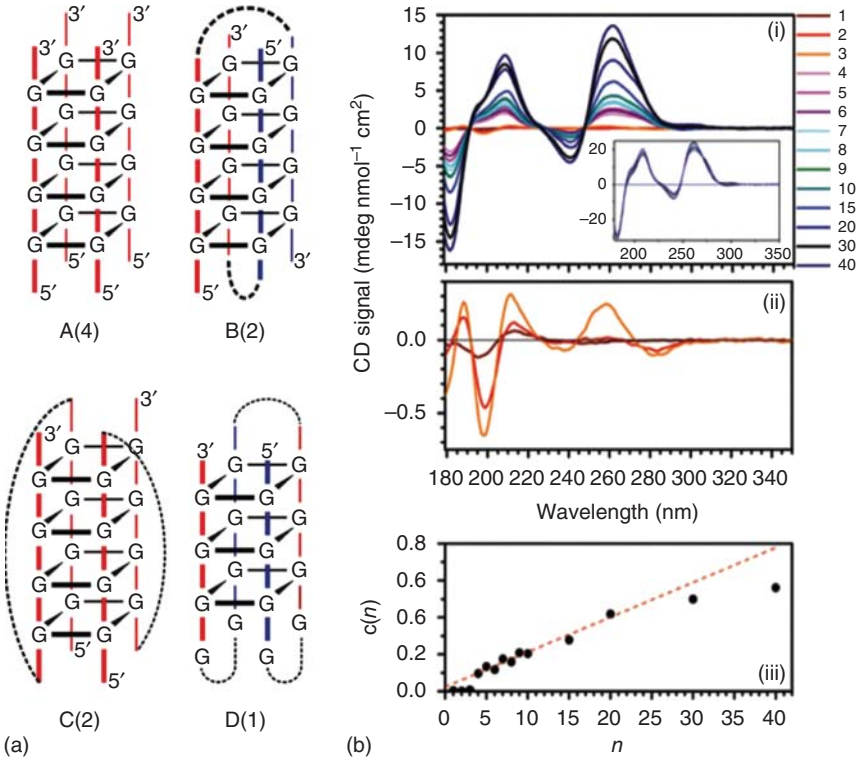

Figure 18.3 (a) Different G-quadruplex structures with strand directions indicated by red (up) or blue (down). The number in parentheses is the number of individual strands in the complex. (b) SRCD spectra for G-quadruplexes of different lengths, showing that signal is linearly correlated with length. (Holm *et al*. 2010 [75]. Reproduced with permission of John Wiley & Sons.)

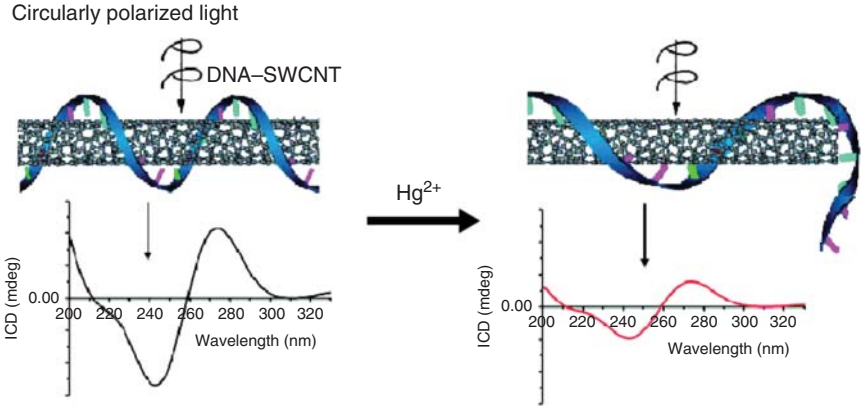

Figure 18.4 Illustration of Hg^{2+}-induced ICD signal intensity change of DNA–SWCNTs. Strong ICD signal was observed for DNA wrapped around SWCNTs. When the Hg^{2+} ions bind to the DNA bases, part of the DNA disassociates from the SWCNTs, leading to a significant decrease in the ICD signal. (Gao *et al*. 2008 [79]. Reproduced with permission of American Chemical Society.)

center loop contributes less to the overall stability of the structure compared with the first and last loops.

18.2.4 Synchrotron-Based Spectroscopic Methods for Studying the Structures of Surface-Bound Nucleic Acids

Immobilization of nucleic acids on solid surfaces is a fast-growing research area that has given birth to numerous cutting-edge biotechnological applications, such as DNA microarrays [81, 82] and biosensors for medical diagnosis and pathogen detection [83–85]. To retain the full function after immobilization, nucleic acids must be oriented with proper densities and correct conformations on the surface. In order to characterize the structures of nucleic acids at these surfaces, XAS, XPS, reflection absorption infrared spectroscopy (RAIRS), and X-ray diffraction (XRD) have been widely applied to provide structural information.

Fujii *et al.* studied evaporated thin films of nucleobases on Au-coated Si surfaces and calculated the angles of different bases with respect to the flat surface using NEXAFS [86]. They found that purines were orientated to the surface, with an angle of $15 \pm 6^{\circ}$ for adenine and $38 \pm 1^{\circ}$ for guanine. Uracil had an orientation of $16 \pm 4^{\circ}$, but thymine and cytosine were randomly orientated with respect to the surface. NEXAFS and XPS have also been used for studying DNA bases on Cu(110), Si(111), and Au(111) surfaces. Furukawa *et al.* compared the orientation of purine nucleobases (G and A) on Cu(110) surfaces, and found that adenine adsorbates laid almost flat while guanine adsorbates were tilted up on the surface [87]. Seifert *et al.* determined the average tilt angles of three nucleobases (A, C, and G) deposited on hydrogen passivated Si(111) surfaces by NEXAFS spectra of the carbon *K*-edge [88]. Their results revealed that adenine and guanine both laid almost flat on the substrate surface, while cytosine adopted a more upright orientation. The adsorption geometry of thymine on Au(111) and Cu(110) surfaces was characterized by Plekan *et al.* using XPS and NEXAFS [89]. These spectroscopic results suggested that thymine oriented almost parallel to the Au(111) surface, while it tilted at a steep angle on the Cu(110) surface.

Since the early work of Tarlov and coworkers on DNA immobilization onto gold surfaces using thiol-terminated ssDNA (thiol-ssDNA), many spectroscopic characterizations have been carried out in order to understand the surface structures of bound DNA [90–92]. Surface coverage of the DNA molecules has been demonstrated to be an important factor in maximizing hybridization efficiency. Hybridization of complementary DNA to densely packed HS-ssDNA on a gold surface was found to be impeded due to steric and electrostatic factors. To maximize the hybridization, spacer molecules were often introduced into the system to vary the coverage of ssDNA on a materials surface [90]. Lee *et al.* studied the kinetics of 11-mercapto-1-undecanol (MCU) displacing HS-ssDNA on a gold surface with NEXAFS, and proposed that the thiol-ssDNA oligomers reoriented toward a more upright position upon MCU incorporation [93]. As shown in Figure 18.5, during short-term backfill of MCU, the vacant surface sites surrounding the loosely packed HS-ssDNA were occupied by the MCU immobilization. Upon extending the MCU backfill time, the DNA molecules

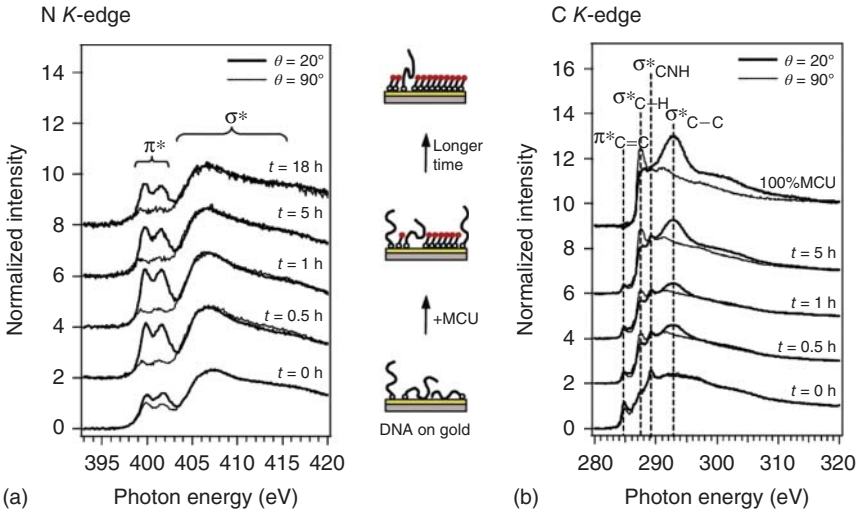

Figure 18.5 Nitrogen (a) and carbon (b) *K*-edge NEXAFS spectra from pure DNA and mixed DNA/MCU monolayers on gold at normal (90°) and glancing (20°) incident X-ray angles with increasing backfill time. In the nitrogen *K*-edge NEXAFS spectra (a), the increase in polarization dependence indicates that DNA bases are oriented more parallel to the surface than bases in the pure DNA monolayer and that ssDNA oligomers reorient on average toward a more upright orientation on the surface upon MCU addition. In the carbon *K*-edge NEXAFS spectra (b), the decrease in the intensity of the $\pi^*_{C=C}$ and $\sigma^*_{C—NH}$ peaks with longer MCU backfill time is consistent with DNA displacement from the surface. (Lee *et al*. 2006 [93]. Reproduced with permission of American Chemical Society.)

were gradually replaced and nonspecific interactions between the nucleobase nitrogen and gold were also weakened, leading to the overall change of ssDNA orientation toward a more upright position. The NEXAFS spectra have also been measured to reveal the orientation and electronic structures of DNA or peptide nucleic acid (PNA) molecules on gold [94], pyrite [95], and InAs [96] surfaces.

18.2.5 XAS in Characterizing the Structures of Metal–Nucleic Acid Complexes

XAS has served as an important tool to provide structural information of metal-binding sites in metal–nucleic acid complexes. The interaction between metal ions and nucleic acids involves mostly nitrogen and oxygen atoms. Owing to the inability of EXAFS to differentiate between oxygen and nitrogen, it is challenging to pinpoint coordinating residues. However, the use of model complexes as references provides the possibility to differentiate between different coordination atoms [97, 98]. Moreover, the EXAFS can provide valuable structural information about metal–ligand distances, as well as coordination numbers.

As the most abundant transition metal ion in cells, iron serves as the metal cofactor for many enzymes that catalyze redox reactions. However, when in excess, iron is believed to generate oxidative stress that can induce damage to cell structures and nucleic acids by converting hydrogen peroxide (H_2O_2) into

highly reactive hydroxyl radicals (•OH) through the Fenton reaction [99–101]. In mammalian cells, Fe(II) has been found to form a complex with DNA and generate •OH from H_2O_2. The •OH can then attack nearby residues and cause oxidative damage to DNA. To understand the coordination of the iron–DNA complex and its implication in mutagenesis, Bertoncini *et al.* studied Fe–DNA interaction using XANES and EXAFS, and found that only oxygen coordinated with Fe(III) while nitrogen and oxygen could bind to Fe(II) [97, 98].

In addition to metal–DNA complexes, metal-binding sites in RNA molecules have also been identified and their specific catalytic functions have been characterized. Ribonuclease P (RNase P) is a type of ribonuclease that cleaves RNA. Unlike other protein-based RNases, RNase P is unique since it is a ribozyme that uses RNA to perform catalytic reactions in the same way as protein-based enzymes. RNase P cleaves off a precursor sequence of RNA on tRNA, and this reaction has been found to be metal ion dependent. Koutmou *et al.* combined NMR and XAS spectroscopy to identify and characterize inner-sphere metal-binding sites in a stem-loop RNA that served as a model for the most highly conserved P4 helix of RNase P [102]. EXAFS spectra revealed inner-sphere binding of Zn^{2+} to one or more of the bases of P4 helix with six-coordinate geometry. Together with NMR characterization, they identified the localization of the metal-binding residues in the active site of P4 helix. Such an approach can also be used as a general method for characterizing inner-sphere metal-binding sites in other nucleic acids.

Cisplatin, as well as many other related platinum (Pt) complexes, is known to be a potent anticancer drug through its interactions with DNA [103, 104]. To understand the formation of the drug–DNA complex, the interaction between the platinum complexes and DNA has been studied using EXAFS as well as X-ray crystallography [105] and NMR [106–109]. Teo *et al.* used EXAFS to reveal the interaction between Pt and DNA [110]. Their findings suggested that four Pt—N (or O) bonds at 2.03 Å were present in the complex in presumably square planar geometry. Hitchcock *et al.* reported the EXAFS study of a DNA complex with a Pt dimer, revealing that the likely binding sites of the Pt dimer were guanine bases. Binding of the Pt dimer to these sites interfered with the hydrogen bonding between DNA strands and impeded the replication process [111]. Kobayashi *et al.* showed that a complex made of DNA and chloroterpyridine platinum (PtTC) could potentially behave as a radiosensitizer for radiotherapy, since it could bind to plasmid DNA and result in an increased yield of strand breaks under X-ray irradiation [112]. Besides cisplatin, bleomycin, an antitumor antibiotic used in cancer chemotherapy, has been characterized in its complex form with Fe(II) using XAS and magnetic circular dichroism (MCD) by Solomon and coworkers [113]. Their results suggest that the general interaction of the Fe(II)–BLM complex with DNA alters the ligand field of BLM, leading to a reaction with O_2 to cleave DNA.

In addition to naturally occurring DNA and RNA molecules, many of the *in vitro* selected functional nucleic acids, such as ribozymes, DNAzymes, and aptamers, can also use metal ions as their cofactors [6, 15]. However, structural characterization, especially X-ray crystallography of functional nucleic acids, is challenging in many cases, probably due to the more dynamic nature of these functional nucleic acids than those of proteins. Therefore, only a limited number

of crystals or NMR structures of functional nucleic acids have been reported. As an alternative approach, XAS has been shown to be a versatile technique to probe the structure of metal sites in these functional nucleic acids in solution.

Thrombin-binding aptamer (TBA) is a 15-mer DNA oligonucleotide that binds thrombin and inhibits thrombin activity [114, 115]. It folds into a unimolecular quadruplex in the presence of K^+. It has been revealed that TBA can fold in the presence of Pb^{2+}, with its conformation similar to that obtained in the presence of K^+. Smirnov *et al.* utilized EXAFS to study the DNA–metal binding site in TBA [116]. Their results indicated that the Pb^{2+} was located in the region between the two quartets in TBA, which was consistent with the structure model in which Pb^{2+} was present between two layers of G-quadruplex and coordinated by eight guanine oxygen atoms.

Mercury is a toxic heavy metal ion in water and soil. dsDNA molecules with consecutive T–T mispairs have been shown to display a strong binding affinity to mercury. Based on this property, DNA-based mercury sensors have been developed [117–126]. Ravel, Lu, and coworkers performed EXAFS study on Hg(II)-binding to the T–T mispairs [127]. They observed a significant difference in EXAFS spectra of mercury in the presence and in the absence of DNA (Figure 18.6). Further fitting with IFEFFIT [128] showed that mercury directly bound to a six-membered ring at 2.04 Å, likely to be a thymine pyrimidine ring. The data is consistent with a thymine–mercury–thymine model based on NMR studies [129–131].

18.3 SAXS for Studying Electrostatics of Nucleic Acids

All nucleic acids are charged and hence electrostatics plays an important role in determining materials behavior. However, electrostatic interactions in biologically relevant physical situations are quite different from those in vacuum. Electrostatic interactions are strongly impacted by the frequency-dependent dielectric response of water. For many situations, we can approximate and use the static zero frequency dielectric constant of water, which attenuates electrostatic interactions by a factor of ~ 80. When one thinks of the additional screening from ions normally found in most biologically relevant solution conditions, it is tempting to draw the conclusion that electrostatic interactions are weak in biological systems. However, ions can make large contributions to electrostatic interactions in ways that are distinct from screening. The entropy of counterions can result in surprisingly strong interactions between charged objects in water despite strong screening. The reason for this is the coupling between osmotic and electrostatic interactions. Many experiments have demonstrated that like-charged objects repel because of the osmotic pressure of counterions confined between charged surfaces, and oppositely charged objects attract because of the entropy gain upon release of counterions. For example, the free energy gain upon binding between two macroions scales as the number of counterions released multiplied by kT, which can impart a massive thermodynamic driving force for the assembly of highly charged objects,

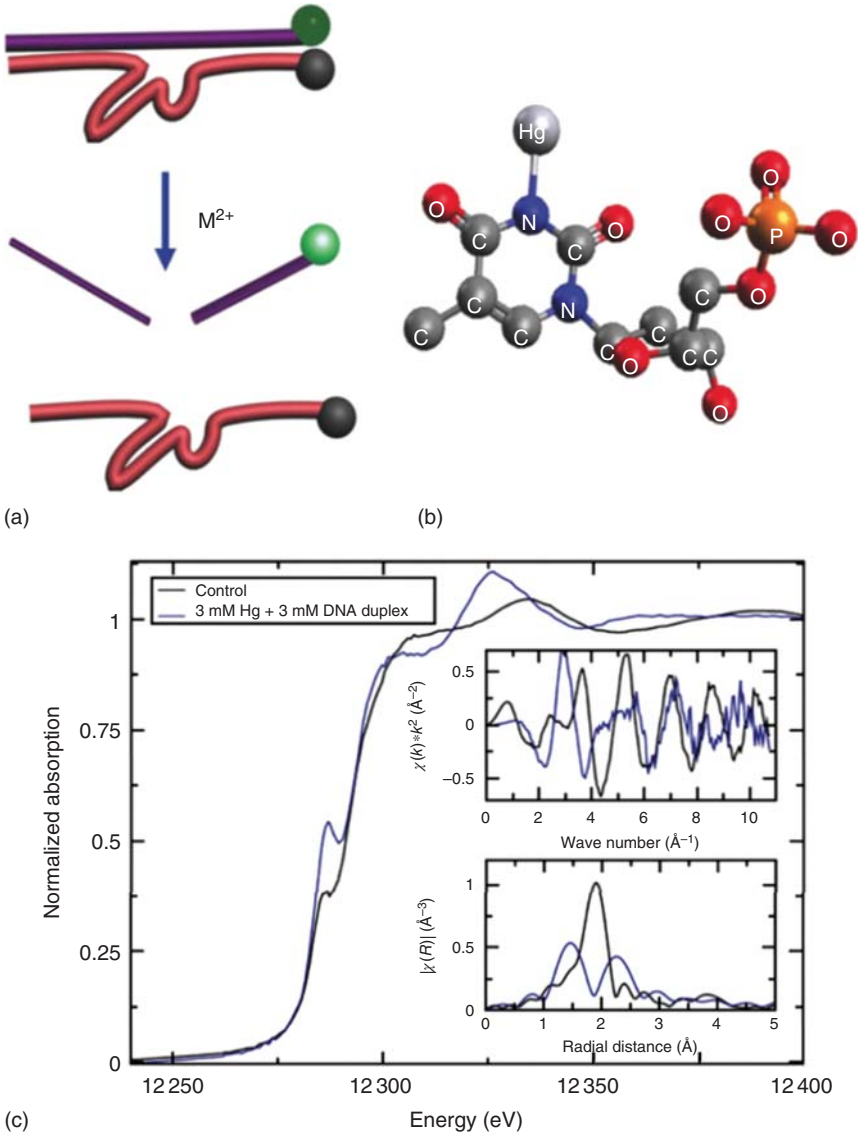

Figure 18.6 (a) Schematic representation of the interaction of the DNA sensor and the target metal. (b) Proposed binding mode of mercury. (c) EXAFS data measured on the Hg control (black) and the sample with 3 mM of Hg and 3 mM duplex DNA (blue). (Ravel *et al*. 2009 [127]. Reproduced with permission of Elsevier.)

such as nucleic acids and cationic lipids used for gene delivery [132]. These are many examples of self-assembled nucleic acid materials systems, and it is beyond the scope of this review to cover all of them with justice. In this section, we aim to review a few examples that illustrate some of the important principles governing the assembly of nucleic-acid-based materials systems.

18.3.1 Theories for Counterion Distribution

As an initial starting point, mean-field theories, such as the Poisson–Boltzmann (PB) approximation, are often used to describe electrostatics. Considering a biological polyelectrolyte in water, such as DNA, the polyelectrolyte will have a distribution of counterions associated with it. The most basic way to describe the counterion distribution around a charged polymer is the PB theory, where Poisson's equation for a Boltzmann distributed charge density is solved [133]:

$$\nabla^2\varphi(\vec{r}) = -\frac{en(\vec{r})}{\varepsilon\varepsilon_o},$$
$$n(\vec{r}) = Ae^{-e\varphi(\vec{r})/kT},$$
$$N = A\int n(\vec{r})e^{-e\varphi(\vec{r})/kT}d^3\vec{r},$$

where e is the elementary charge of a single electron, r is the distance away from the polymer, ε is the dielectric constant of the solvent, ε_0 is the permittivity of free space, n is the number density per rod of counterions (condensed and free), and N is the total number of counterions per rod. These can be solved exactly for stiff, infinitely long rods with no externally added salt. The solution shows that there is a significant enhancement of counterion concentration near the polyelectrolyte surface. The Debye–Hückel theory uses an approximate linearized treatment of the PB equation and defines the Debye screening length, $1/\kappa$, which is the thickness of the cloud of condensed counterions:

$$\frac{1}{\kappa} = \left(\frac{N}{\nu}\frac{e^2}{\varepsilon\varepsilon_o}\frac{1}{kT}\right)^{\frac{1}{2}},$$

where k is the Boltzmann constant, T is the equilibrium temperature of the system, N is the total number of counterions per rod, and ν is the effective volume of a rod.

However, the PB theory has many limitations. For example, it fails for highly charged systems, for the existence for multivalent salts, for strong dielectric heterogeneity, and for any situation where fluctuations and correlations are important. Therefore, it cannot explain many electrostatic properties regarding self-assembled nucleic acids.

Another interesting and intuitive description of polyelectrolyte electrostatics was given by Manning [134]. The "Manning condensation" theory treats a polyelectrolyte as a stiff, charged rod of length L, radius a, and consisting of Z uniformly spaced charged sites – each of charge q. Counterions of concentration $\rho_c = Z\rho_p$ (ρ_p is the concentration of the polyelectrolyte) are treated as point charges of charge q. The interaction potential between a long cylinder and a counterion is

$$\phi = -\frac{2q\lambda_0}{\varepsilon}\ln\left(\frac{r}{r_0}\right),$$

where $\lambda_0 = -q/b$ is the line-charge density, b is the separation between charges, and r_0 is the arbitrarily chosen point of zero potential. A polyion–counterion

two-body partition function is

$$\zeta_1 = L\int_a^R e^{-\beta q\phi(r)}d^2r = \pi L r_0 \frac{(R/r_0)^{2-2\xi} - (a/r_0)^{2-2\xi}}{1-\xi},$$

where $\beta = 1/kT$ and R is the cut-off distance below which counterions are bound to the polyion. The Manning parameter ξ is defined as

$$\xi = \frac{q^2}{\varepsilon kTb}.$$

For infinitesimally thin rods, $a = 0$ and the integral diverges as $\xi \to 1$. This divergence was taken as an indication of counterion condensation. For $\xi > 1$, n counterions condense onto the polyion reducing the effective charge density to

$$\lambda_n = \lambda_0 \frac{Z-n}{Z}.$$

The number of condensed counterions is given by

$$n = Z\left(1 - \frac{1}{\xi}\right) \quad \text{for } \xi > 1$$
$$n = 0 \quad \text{for } \xi \leq 1.$$

The Manning theory predicts that the final charge density of the polymer is compensated by the counterions and depends only on the valence of the ions. Besides PB theory and Manning theory, other mean-field theories have also been formulated. They provide information on quantitative distribution of ions, but they consider neither finite ion sizes nor the correlations between ions [135–137]. In general, mean-field theories predict that like-charged polyelectrolytes always repel irrespective of the salt conditions. Changing the valence of the ions reduces the repulsion strength but never leads to attraction. This clearly does not agree with experimental observations in the last few decades [138, 139].

18.3.2 Contemporary Theoretical Approaches to Polyelectrolyte Electrostatics

Nucleic acids are examples of highly charged polyelectrolytes. Assembly of polyelectrolytes by multivalent ions or/and macroions is widely observed in biology and bioengineering. Nucleic acids can collapse into a compact phase from solution as the concentration of oppositely charged multivalent ions or macroions increases. Examples include DNA packaging in viruses [140, 141] and in bacteria [142, 143]. Synthetic molecules that package DNA for delivery are also good examples [144–148]. From a considerable body of theoretical and computational work, we have a better idea as to why nucleic acids can form aggregates, a behavior that seems to require overcoming large electrostatic repulsions [140, 149–153]. In situations with high surface charge densities or with multivalent ions, the organization and dynamics of condensed ions are important [154]. A series of insightful Monte Carlo simulations demonstrated attraction between like-charged DNA molecules [155, 156]. In the last two decades, a large number of theoretical investigations have focused on the physical origins of these types of "like-charge attraction" [157–163] and on the structures of

the induced polyelectrolyte organization [164–168]. Correlations between condensed counterions on the polyelectrolyte can be the basis of attractions and generate ordered structures of polyelectrolytes. Oosawa showed that thermal fluctuations of the condensed counterion layers on different polyelectrolytes can be correlated and thereby induce like-charge attractions [169]. These ideas have been improved upon by various groups [170, 171]. As the polyelectrolytes approach one another and the distances between them become smaller, local fields due to the geometric arrangement of charges on a polyelectrolyte can lead to spatial patterns of counterion binding [152, 172]. In principle, if these ions are ordered into a periodic lattice, attractions can result as counterions on opposing surfaces arrange themselves into complementary patterns. This elegant picture of interacting Wigner crystals was due to the work of Rouzina and Bloomfield [157], Shklovskii [173], and Lau *et al*. [174]. Recent work in the "strong coupling" limit [175, 176], where the counterion valence or surface charge density is higher than what PB theories can handle [177] and where correlations between counterions are strong, has predicted the spatial dependence of attractive interactions [163, 177, 178]. Using a new analytical Wigner-crystal-based formulation of strong coupling, Šamaj and Trizac were able to eliminate divergences from the earlier virial expansion approach and obtain theoretical results on charged surfaces that agree well with Monte Carlo simulations for the first time [179].

18.3.3 Ordered DNA Structures with Multivalent Ions

dsDNA has a linear charge density of $-2e/0.34$ nm and is a semiflexible polymer rather than a rigid rod. Deformations (such as bending and twisting) of DNA molecules are linked to its function and its elasticity can be an important parameter in DNA condensation [180, 181]. Genomic DNA molecules are long but can be efficiently packaged. For example, DNA in the T4 phage genome contains 160 kbp and has a contour length approaching 54 μm, yet it can be packaged into a viral capsid of 100-nm diameter [182]. The high linear charge density leads to strong Coulomb repulsion between adjacent strands. A number of packaging strategies can be seen in nature. For example, DNA packaging in bacteriophages sometimes requires assistance from ATP-powered motors that pump DNA into the capsid against high pressures [183], while in eukaryotic genomes, multiple proteins such as histones are involved in DNA packaging.

One common way to package anionic DNA is the use of multivalent cations [184]. Short DNA strands can form liquid crystalline aggregates [185], either hexagonal or cholesteric, in the presence of spermidine or spermine [186, 187]. The interhelical spacing of DNA within such complexes is observed to depend on the precise ionic conditions [188]. Osmotic pressure can also be used to drive DNA into ordered arrays [189, 190]. In addition to electrostatics and osmotic pressure, chemical interactions between ions and specific binding sites on DNA can also be important [191]. Ions with the same valence can have different interaction modes or prefer different binding sites on the DNA [191]. Ion size and geometry [192, 193], ion hydration [194], and site-specific binding also contribute to DNA condensation. (Mn^{2+} binds in the grooves. In contrast, Ca^{2+}

and Mg^{2+} bind to the sugar phosphate backbone.) Additionally, the structure of the underlying surfaces, such as the geometry of the grooves and the helical pitch of the backbone, can also contribute [195]. For example, in polymer-condensed arrays of parallel DNA helices in monovalent salt solutions, positional disorder in DNA helices leads to molecular repulsions even at large separations due to increase in configurational entropy. It is also observed that the electrostatic double-layer decay length is approximately twice the Debye length except at high ionic strengths [196].

18.3.4 Measurements of Counterion Distributions around DNA

Anomalous SAXS has been used to study spatial distributions of condensed counterions around DNA (Figure 18.7) [197–200]. This technique enables measurement of nonlocalized counterions but requires counterions with high valency. Short DNA duplexes, 25 bp in length, were used as these are much shorter than the duplexes' persistence length and can be accurately modeled. Condensation of these duplexes was induced by adding multivalent cations. It was observed that with ions of comparable size but mixed valence, DNA charge is neutralized more effectively by divalent ions than by monovalent ions [198]. Similarly, trivalent ions displace monovalent ions [201]. These observations are consistent with the expectation that condensation of trivalent ions by polyelectrolytes is preferred from an entropic standpoint, since each condensed trivalent ion can liberate three monovalent ions for a large entropy gain. Very small amounts of trivalent ions are needed to induce attractive forces in the duplexes. The spatial distribution profiles of the ions also indicate a tighter binding to the DNA for higher valence counterions; however, the ion size modifies the distance of closest approach. Steric interactions prevent ions from attaining electrostatic free energy minimum [197, 202].

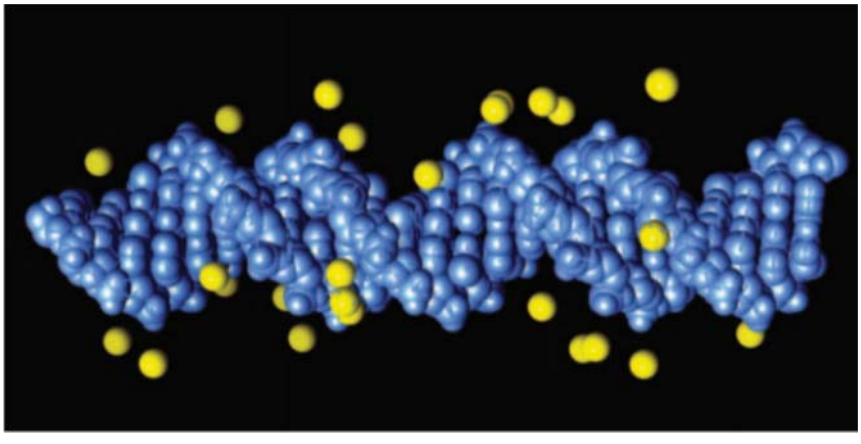

Figure 18.7 Spatial distribution of monovalent ions (yellow) around DNA (blue) determined by computing the electrostatic potential around the DNA, using anomalous SAXS. (Adapted from Wong and Pollack 2010 [132].)

18.3.5 Folded RNA Structures with Multivalent Ions

Compared with DNA duplexes, the spatial distribution of monovalent and divalent ions is different for RNA duplexes. The structural variations in the DNA and RNA helices may account for this difference. RNA duplexes form an A-form helix while the DNA duplexes form a B-form helix. The A-form helix is also right-handed but is thicker than the B-form helix and has shorter distance between base pairs. It also has a deeper and narrower major groove and a very shallow minor groove. The RNA major groove has a high negative potential [203], which results in more ions at a shorter distance from the RNA helix as compared to the DNA helix. Therefore, RNA helices are fully screened at shorter distances than DNA helices [195].

Unlike DNA, many examples of physiological RNAs are single-stranded molecules. Functional RNA structures contain rigid, short helical regions joined by more flexible single-stranded regions, loops, hinges, or junctions [204]. Most RNAs fold into compact tertiary structures stabilized by small, typically millimolar quantities of Mg^{2+} [136, 205]. Fully hydrated ions follow the electrostatic field of the RNA. Therefore, their concentration is proportional to the magnitude of electrostatic potential with the highest concentration being in the region of the major groove where the potential is highest. These ions screen the charge on the RNA backbone, enabling the close approach of RNA helices, but they do not generate attractive forces on their own. Strong connections between different regions of the RNA chain are forged by ions that make specific contact with the backbone. To make specific contacts, the ions must be partially dehydrated. Secondly, they must overcome the repulsive electrostatic forces with the remaining hydrated ions. There are very limited sites where the interaction is favorable enough to overcome the large penalties of dehydration and repulsion. At these sites, the ion is in a deep pocket with an electrostatic potential an order of magnitude higher. Thus, very few ions of this type are found in RNA structures [206–210].

18.3.6 DNA Compaction by Osmotic Pressure

Condensation of polyelectrolytes by oppositely charged multivalent ions is not the only way to generate ordered arrangements of nucleic acids. For example, condensed phases of DNA can also be obtained by applying osmotic pressure. This can be achieved either by increasing DNA concentration in the presence of monovalent ions or by removing water by adding molecules such as PEG or dextran [189, 190, 211]. With increasing DNA concentrations, a rich liquid crystalline phase behavior is observed. The isotropic solution first transforms into a precholesteric or blue phase, then into a cholesteric phase, which turns into a columnar hexagonal phase and finally into crystalline phases [189, 212]. Structural information about these condensed phases can be obtained by XRD. In a columnar hexagonal phase, DNA molecules are aligned parallel with respect to one another and form a hexagonal arrangement. These molecules, however, are free to slide against each other and can rotate around their long axes. In the cholesteric phase, DNA molecules are locally aligned with one another in sheets, but their orientation rotates continuously along the cholesteric axis. Two

different crystalline phases have been observed – a 3D hexagonal phase and a 3D orthorhombic phase. As the DNA concentration is increased, the interhelix distance decreases and the helix pitch decreases from 34.6 to 30.2 Å. Since the distance between base planes is constant, the number of nucleotides per turn decreases continuously from 10.3 to 9.0 bp per turn. Therefore, the DNA helix can progressively change its twist state in condensed ordered phases even though it remains B-type [189, 190].

With increase in concentration of DNA, the parallel alignment of DNA molecules into a hexagonal network competes with the tendency of DNA helices to form chiral structures. The interhelix distance decreases with increasing concentration and the condensed phase goes from a double twist configuration (in precholesteric phase) to a simple twist configuration (in cholesteric phase). Eventually, the twist is prevented everywhere except along particular defect lines (screw dislocations). The average twist angle between adjacent molecules varies from 2° in the blue phase to 0.7–0.46° in the cholesteric phase and 0° in the columnar phase. The double twist configurations can reappear when the cholesteric phase is subjected to external constraints resulting in a mosaic of domains with the double twist configuration. In the columnar phase too, twist walls may be observed between hexagonal domains that probably relax the twist constraints [189, 213].

It is interesting to note that osmotic effects in mixtures of polyelectrolytes can manifest in unexpected ways. Interaction between DNA coils and F-actin rigid rods can produce striking liquid crystalline behavior. In a recent study, phase behavior of DNA chains and actin rods (both negatively charged) was examined using synchrotron XRD. An entangled percolating network of elongated nematic actin domains threading through a mesh of random DNA coils was observed. The inter-actin spacing in the nematic domains is strongly dependent on DNA concentration. Upon addition of salt, the system evolves from a counterion-controlled osmotic pressure regime to a depletion-controlled regime: the nematic phase disappears as DNA infiltrates into the elongated actin domains, thereby reorganizing them into "comb-like" structures with smaller actin domains surrounded by DNA [214].

18.3.7 Liquid Crystalline DNA Complexes and Autoimmune Diseases

Recent work has shown that nucleic acids and innate immunity peptides play an important role in autoimmune diseases such as psoriasis and lupus. Antimicrobial peptides (AMPs) such as α-defensins and the cathelicidin LL37 [215–219] are overproduced in autoimmune diseases such as psoriasis. LL37 allows plasmacytoid dendritic cells (pDCs) to recognize self-DNA through Toll-like receptor TLR9, potently activating the pDCs to overproduce type I interferons (IFN) [220, 221]. Endosomal TLR7 and TLR9 are major innate receptors that activate pDCs to secrete type I IFN [222, 223]. TLR7 and TLR9 recognize RNA and DNA viruses, respectively [224, 225]. Self-nucleic acids usually have limited access to intracellular compartments, but gain endosomal entry under pathological conditions. These nucleic acids released by dying cells are often associated with cationic proteins (including antimicrobial peptide

LL37), or bound by autoantibodies in immune complexes that interact with Fc receptors on cell surfaces [223, 226, 227]. In autoimmune diseases such as psoriasis [221] and lupus [228], anionic self-nucleic acids can form electrostatic complexes with cationic AMP LL37 and potently activate pDCs to produce type I IFNs and exacerbate disease [220]. Recent findings show that this effect is more general: Human defensins HBD2 and HBD3 [229] can also convert self-DNA into an activator of TLR9 in pDCs [229], and several chromatin-derived proteins form complexes with DNA and contribute to TLR9 binding [230] and activation [231, 232]. Complex formation can protect self-DNA from enzymatic degradation [233], and enable endosomal access required for TLR9 receptor binding. However, this process is not sufficient for pDC activation, since other DNA complexes with such access are unable to activate TLR9.

We have recently shown that self-DNA can form liquid crystalline complexes with overexpressed antimicrobial peptide LL37, and investigated the relationship between the ordering of these self-DNA complexes and pDC production of IFN (Figure 18.8) [234]. Such AMPs are characterized by strong cationic charge and amphiphilicity, so they are in principle capable of multiple modes of ordering when they interact with nucleic acids. Using synchrotron X-ray scattering, we demonstrated how a broad range of cationic molecules besides LL37 can complex with DNA and trigger pDC interferon production, while many other cationic molecules do not. Electrostatic interactions between TLR9 and DNA are optimized when these complexes have inter-DNA spacings that are comparable to the steric size of TLR9 receptors, which allows "interdigitation" of multiple receptors and ligands similarly to teeth in a zipper. Furthermore, the presentation of multiple DNA chains recruits more TLR9 receptors for binding, resulting in a drastic increase in the number of *active*, ligand-bound receptors and amplification of

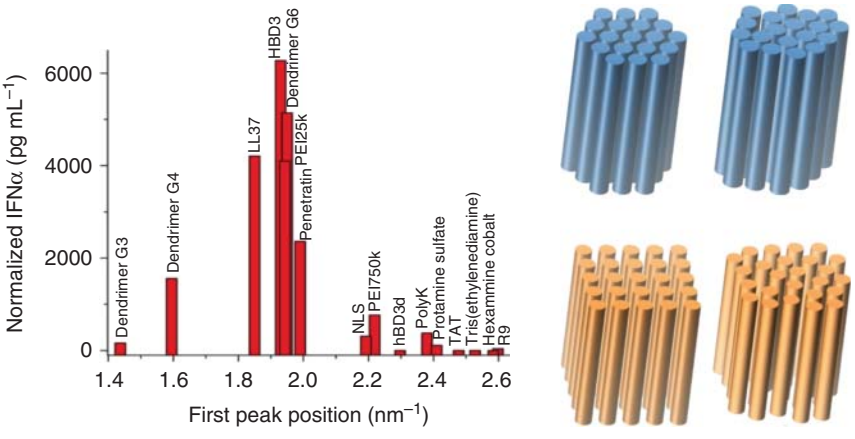

Figure 18.8 DNA complexes with a specific range of inter-DNA spacing that match up well with the steric size of TLR-9 receptors (orange arrangements of rods) will lead to high levels of immune activation, as measured by interferon production from harvested human plasmacytoid dendritic cells. DNA complexes with smaller inter-DNA spacings (blue arrangements of rods) do not. The same is true for complexes with much larger inter-DNA spacings. (Adapted from Schmidt *et al*. 2015 [234].)

pDC IFN production. The results on the liquid crystalline ordering of nucleic acids are surprising: they suggest the possibility of a quantitative understanding of how biological molecules assemble with self-DNA to break our immune system's tolerance to it, which is valuable and enabling to the fundamental science of immunity.

18.4 SAXS in Studying Conformations of Nucleic Acids

SAXS is a technique that can be used to probe the structures and interactions of biomolecules in solution at a low resolution (1–2 nm). The main principle of SAXS was developed by André Guinier in the 1930s, following his studies of metallic alloys. SAXS was found to provide not just information on the sizes and shapes of particles but also information on the internal structures of disordered and partially disordered systems. The method was adopted for characterizing biomolecules in solution in the 1960s. Since most biomolecules, such as proteins and nucleic acids, have sizes larger than the wavelength of X-rays, they can give a relatively good SAXS scattering pattern. Information about the size, shape, compactness, and molecular weight of molecules in solution can be readily obtained using this method. Therefore, it is a powerful probe for examining protein and nucleic acid conformations. Compared with crystallization and NMR spectroscopy, SAXS does not require high-quality crystals as in crystallography, nor does it have strict limits on the molecular weight of the sample as in NMR spectroscopy. SAXS can also tolerate a variety of conditions for measurement, ranging from physiological to highly denaturing conditions. Breakthrough in SAXS data analysis methods, such as those reported by Svergun and Stuhrmann in the 1990s, had a significant impact on the use of SAXS for scattering studies of a wide range of molecules in solution. Their procedures allowed extraction of meaningful three-dimensional details from one-dimensional scattering data, resulting in reliable *ab initio* shape and domain structure determination for the first time. Meanwhile, the increasing availability of third generation synchrotron sources [235], accompanied by improvement in time resolutions down to the submilliseconds, has largely increased the number of users of SAXS and created excellent opportunities for a variety of biological applications in the past decade [236, 237]. Here, we focus on the recent development and applications of SAXS in structural studies of nucleic acids.

18.4.1 Use of SAXS for Probing Intermediates in RNA Folding

The discovery by Cech and Altman in the early 1980s that RNA can act as an enzyme [238, 239] has led to considerable interest in elucidating the structure and function of RNA molecules. In addition, there is also an emerging awareness of the extensive involvement of RNA machineries in gene control processes. Numerous riboswitches with complex folded domains have been identified in the noncoding region of mRNAs in prokaryotes [240, 241]. These riboswitches change their structures upon binding of specific metabolites and influence transcription or translation at different levels, thereby controlling many biological

processes. The complex tertiary structures of ribozymes and riboswitches and folding process of their tertiary structures have been extensively studied during the past two decades [242, 243]. To build the relationship between structure and function of these special RNA molecules, X-ray crystallography has served as a powerful tool for obtaining structural information with atomic resolution. However, to probe the intermediates in the folding pathways, unfolded or partially folded conformations commonly coexist in the system, resulting in a complex system where X-ray crystallography cannot be readily applied. Instead, SAXS has been shown to be one of the major tools for obtaining global information on the size and shape of folding intermediates of RNA molecules in solution, since it provides quantitative characterization of mixtures by measuring the radius of gyration (R_g) of molecules with 1–3 nm resolution [244]. Moreover, time-resolved experiments carried out with rapid-mixing methods to trigger folding can provide unique information about the structures of transient intermediates populated during the folding process.

One fundamental question in RNA folding is the nature of the rate-limiting step. The early effort in understanding how ribozymes fold dates back to the 2000s. Russell *et al*. reported an initial study using SAXS to monitor the changes in the overall size and shape of the intermediates as *Tetrahymena* group I ribozyme folds (Figure 18.9a) [245, 246]. By measuring the R_g using SAXS, they found that the native ribozyme, formed in the presence of Mg^{2+}, adopted a more compact and globular conformation than the unfolded ribozyme. Moreover, time-resolved measurements suggested that the ribozyme collapsed into a compact intermediate within a few milliseconds after addition of Mg^{2+}, with a rate constant at least 20-fold faster than the overall rate constant for folding (Figure 18.9b). This fast compaction was found to last on the order of 100 ms, before slower rearrangements of misfolded intermediates took place. The fully functional state eventually formed on the timescale of about 100 s. Their results indicate that there is a kinetic trap involved in the folding process, and rearrangement of misfolded structures is the rate-limiting step.

In a subsequent study of the ribozyme folding process, Das *et al.* designed a quintuple mutant of the *Tetrahymena* ribozyme to destabilize the tertiary contacts within the folded ribozyme [247]. Time-resolved SAXS measurements showed that collapse to the compact intermediate upon the addition of salt still occurred, even in the absence of the specific tertiary interactions. These results suggested that the initial compaction was a result of nonspecific shielding of the Coulomb forces by the added counterions. However, the tertiary hydrogen bond contacts were found to be important in the subsequent compaction on the timescale of 100 ms.

Similarly, the compaction process of yeast $tRNA^{phe}$ [248], the catalytic domain of the *Bacillus subtilis* RNase P RNA [249], the *Candida* group I ribozyme (Ca.L-11) [250], and the *Azoarcus* group I ribozyme [251] were investigated using SAXS or small-angle neutron scattering (SANS) by different groups. In contrast to the *Tetrahymena* ribozyme, these ribozymes exhibited rapid folding processes from the initial collapse to the native state, suggesting that the folding pathways did not involve long-lived kinetic traps.

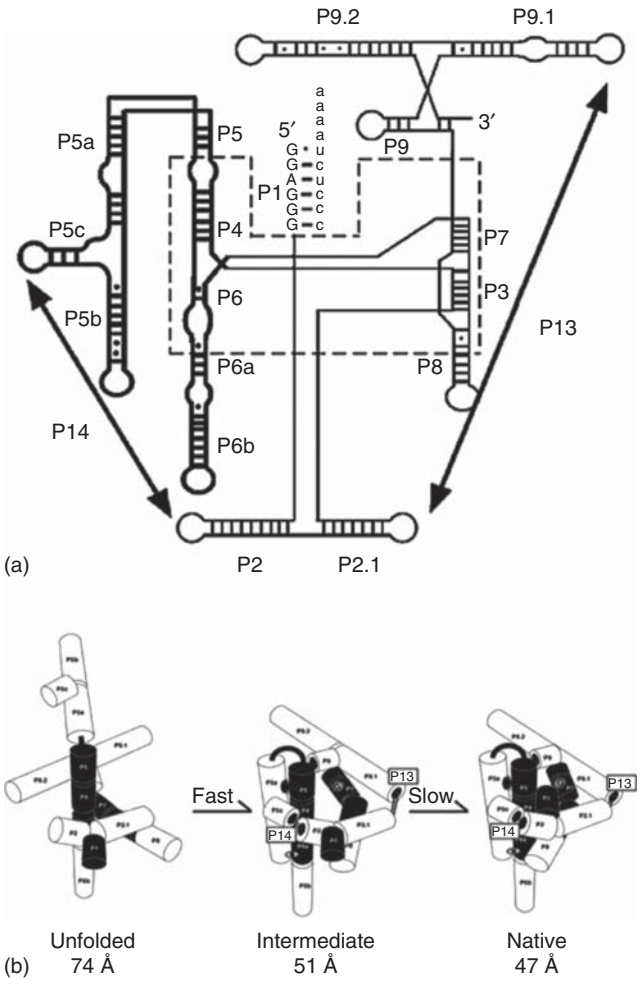

Figure 18.9 (a) The *Tetrahymena* ribozyme. P1–P13 represent different paired secondary structure elements in the ribozyme, and the long-range pairings P13 and P14 are indicated with arrows. The boxed portion is the ribozyme core, which is most highly conserved. The core is largely protected from solvent in the presence of Mg^{2+}. (b) A model in which compaction of the ribozyme is much faster than the overall folding to the native state. (Russell *et al*. 2000 [245]. Reproduced with permission of Nature Publishing Group.)

To reveal the interplay between core and peripheral elements in ribozyme folding, Baird *et al.* used SAXS combined with chemical and nuclease mapping, CD, and molecular modeling to investigate the folding intermediates of the specificity domain, or S-domain, of the *Bacillus subtilis* RNase P RNA [252]. The structure of this RNA is composed of four tertiary structural modules, including a rigid core, a four-way junction, a GAAA tetraloop–receptor, and an unusual motif involving two tertiary interacting loops (Figure 18.10a). Their findings suggested that in the thermodynamic folding pathway, an intermediate containing two of the four native tertiary modules was populated. The size and shape of the native RNA

and the intermediate structures were characterized by SAXS measurements. The results indicated that the size of the intermediate was bigger and the shape was more extended than those for the native RNA. The intermediate lacked the core, and folding from the intermediate to the native structure involved the formation of the core as well as significant conformational changes that bring two peripheral helices close to each other in order to form the tetraloop–receptor interaction (Figure 18.10b).

To compare how the charge and size of the cations influenced the collapse transition in different ribozymes, Moghaddam *et al.* used SAXS to monitor the

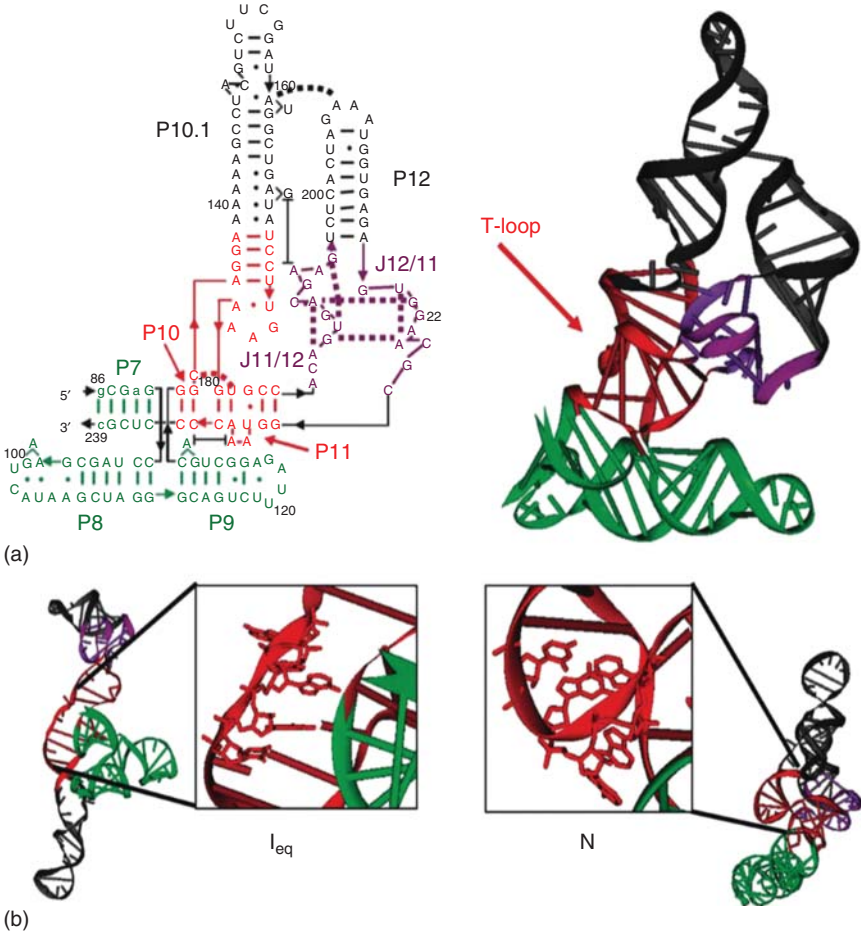

Figure 18.10 (a) Secondary structure of the RNase P from *Bacillus subtilis*, and its crystal structure containing the four-way junction (green), the core (red), the J11/12 junction (purple), and the TL-receptor (black). Broken lines represent tertiary interactions, while continuous lines indicate stacking interactions in the native structure. The T-loop in the core is composed of five nucleotides, and is of particular importance to the folding intermediate. (b) Comparison between the structure of the intermediate (I_{eq}) and the native structure (N). In the I_{eq} structure, the T-loop is extended whereas in the native structure it forms a compact loop. (Adapted from Baird *et al*. 2005 [252]. Reproduced with permission of Elsevier.)

changes in the R_g of the *Azoarcus* and *Tetrahymena* ribozymes with different cations [253]. Their findings suggested that both ribozymes underwent collapse transition to native conformations in all of the counterions they tested (Na^+, K^+, Mg^{2+}, Ca^{2+}, Co $(NH_3)_6^{3+}$, Ba^{2+}, Sr^{2+}, and spermidine^{3+}). Small, multivalent cations induced the collapse of both ribozymes more efficiently than monovalent ions. However, counterion-induced collapse and formation of tertiary interactions occurred at the same time for the *Azoarcus* ribozyme, while the folding of the *Tetrahymena* ribozyme was composed of two distinct transitions in the presence of increasing concentrations of Mg^{2+}, which was best explained by a three-state model.

Besides ribozymes, SAXS has also been used to study the thermodynamic folding pathways of riboswitches. For example, Lipfert *et al.* studied the folding of a glycine-dependent riboswitch (VCI-II) from *Vibrio cholerae* using SAXS in combination with hydroxyl radical footprinting [254, 255]. They proposed a three-state thermodynamic model for energy coupling between magnesium-induced folding and glycine binding. Under low salt conditions without any Mg^{2+}, the VCI-II riboswitch adopted an extended overall conformation indicating unfolded structures. Addition of millimolar concentrations of Mg^{2+} in the absence of glycine resulted in a significant compaction and partial folding. Addition of glycine in the presence of millimolar Mg^{2+} led to further compaction mediated by additional tertiary packing interactions and further binding of Mg^{2+}. Using a 3D reconstruction algorithm DAMMIN, they were able to obtain low-resolution 3D structures for all three states derived from SAXS measurements (Figure 18.11a).

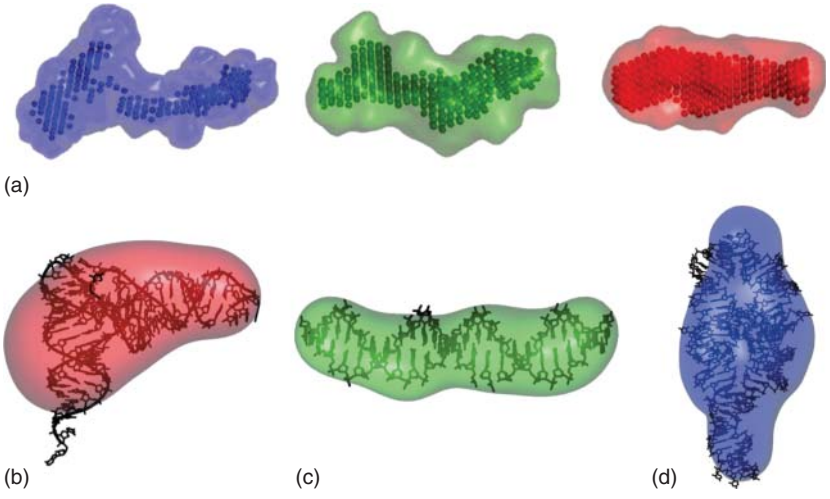

Figure 18.11 (a) Low-resolution structures of VCI-II riboswitch under different solution conditions, including average unfolded conformation (blue), conformation in the presence of 10 mM magnesium and absence of glycine (green), and glycine-bound structure (red). (b–d) Reconstructed density of (b) the yeast $tRNA_{Phe}$, (c) the 24 bp DNA duplex, and (d) the P4–P6 domain of the *Tetrahymena* group I intron. Atomic resolution structure (black sticks) and reconstructed density (colored transparent surfaces) are superimposed. (Adapted from Lipfert *et al*. 2007 [255] and Lipfert *et al*. 2007 [256].)

With the development of different algorithms for reconstructing 3D density maps from SAXS profiles [257, 258], the overall structures of several RNA and DNA molecules have also been successfully reconstructed from their SAXS data. Using bead model representations of the macromolecules as an input to calculation, which had been commonly used for reconstructing proteins and their complexes previously [259–262], Lipfert *et al*. reported reconstructed low-resolution density maps for three different types of RNA molecules, including yeast $tRNA^{phe}$, a 24 bp B-DNA duplex, and the P4–P6 domain of the *Tetrahymena* group I intron (Figure 18.11b–d) [256]. The reconstructed structures are in good agreement with actual crystal structures. Their approach demonstrated that besides being applied to proteins, low-resolution reconstruction methods could also be applied to nucleic acids. Such a method is potentially applicable to other biomolecules for obtaining structural information when the high-resolution structure is not available.

Although SAXS can provide reliable data for investigating RNA molecules, in practice, predicted shapes or conformations can be inconsistent with actual structures due to the existence of misfolded RNA molecules in a sample. To improve SAXS data for structural analyses, Rambo and Tainer reported using size exclusion chromatographic purification as a general approach to reduce the heterogeneity of the samples and therefore largely improve the accuracy of predicted shapes for a variety of RNA molecules, including ribosomal subunits, tRNAs, ribozymes, and riboswitches [263].

The past decade has witnessed significant improvements in SAXS data collection techniques and computational algorithms for analyzing SAXS data. With continuous development, SAXS can be an invaluable tool for providing structural insights into biomolecules in the absence of prior structural information.

18.4.2 Use of SAXS for Studying Noncanonical Structures of DNA and RNA Molecules

Besides forming right-handed double helices as genetic materials, nucleic acids have also been found to be capable of adopting a variety of noncanonical structures *in vitro* or *in vivo* for different functions. For example, eukaryotic chromosomes are terminated with telomeres containing small, tandemly repeated guanidine-rich DNA sequences [264]. *In vitro* biophysical characterization indicates that these G-rich sequences can form four-stranded structures, known as G-quadruplexes, under physiologically relevant conditions. Structures of G-quadruplexes usually include sets of four guanine bases held in plane through Hoogsteen hydrogen bonding and then stacked on top of each other. The quadruplex structures can be further stabilized by cations, especially K^+ ions, which are located in the central channel formed between each pair of tetrads. Recently, a low-resolution structure of a G-quadruplex derived from human telomere repeats, $d(TTAGGG)_4$, was obtained on the basis of SAXS data collected by Kozak *et al*. [265]. Together with crystal structures and NMR structures, the structure and potential conformational changes of G-quadruplex in solution were revealed, providing useful information for elucidating functions of G-quadruplexes *in vivo*.

In addition to G-quadruplexes, DNA molecules have also been shown to form an i-motif in solution. The i-motif is a four-stranded DNA structure formed by intramolecular noncanonical base-pair interactions between protonated and unprotonated cytosines under slightly acidic conditions (e.g., pH < 6.5). Based on the fact that the i-motif can reversibly undergo a structural change driven by a pH change, both DNA nanomachines that can generate motions for multiple cyclings and DNA nanodevices that can map intracellular pH gradient in real time have been demonstrated [266–268]. Detailed structural information of i-motif DNA in solution at various pH conditions was characterized using SAXS technique by Jin *et al*. [269]. Their observations indicated that the i-motif DNA molecules adopted multiple conformations over a wide pH range, providing structural basis for future design of DNA-based nanodevices.

Moreover, over the past two decades, there have been increasing efforts invested in isolating new types of functional nucleic acids *in vitro*. With a combinatorial method named *in vitro* selection [3] or SELEX [2], DNA or RNA molecules that can bind specific targets with high affinity or possess catalytic activities in the presence of metal ions or small molecules have been selected. Numerous kinds of sensors or targeted drug delivery systems have been designed based on these aptamers and DNAzymes [15, 21, 28, 270–276]. However, compared to the rapid development of sensor devices, little is known about the three-dimensional structures of these functional nucleic acids, and only a limited number of crystal structures of a few aptamers [277–292] and one misfolded DNAzyme [293] are available. In a complementary approach to fluorescence resonance energy transfer (FRET) studies on DNAzymes [294–297], SAXS combined with other characterization techniques have been shown to be possible to obtain the 3D structural information of aptamers alone or in complex with their targets. Using SAXS in combination with fluorescence correlation spectroscopy (FCS), Werner *et al.* characterized the structure of an RNA aptamer named SRB2m, which has a high affinity to a dye called sulforhodamine B [298]. The aptamer, as well as the sulforhodamine B-aptamer complex, was found to form dimers predominantly in solution (Figure 18.12). Interaction of another dye, named patent blue V (PBV), with the SRB2m led to a dissociation of the SRB2m dimers into monomers. More recently, Reinstein *et al.* used SAXS to characterize a cocaine-binding aptamer either in its free form or substrate-bound form [299]. Their *ab initio* shape reconstruction structures are also consistent with the structural-switching binding mechanism. With these latest examples, continuous progress in obtaining the structural information of these noncanonical nucleic acids is highly desired, since it can not only guide the future design and optimization of sensors, but also provide insights into the mechanisms behind the functions of aptamers and DNAzymes.

In addition to aptamers and DNAzymes, the relationship between the structure of DNA and its biological functions has been studied using polypod-shaped DNA molecules. Nishikawa *et al.* constructed polypod-like structures from oligonucleotides with cytosine–phosphate–guanosine (CpG) motif, and found that increasing pod number is directly correlated with increasing ability to induce immune stimulation through cytokine secretion [300]. As a step further, Sanada *et al.* carried out synchrotron X-ray scattering to investigate the

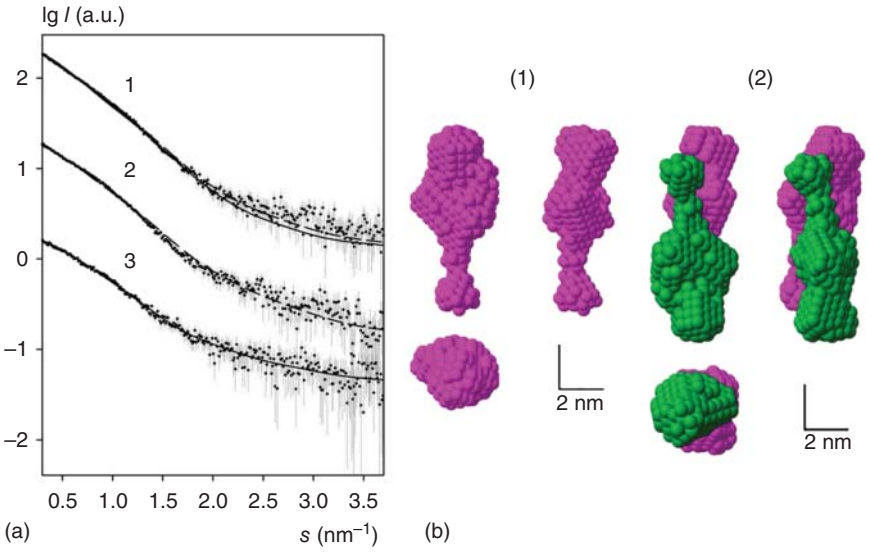

Figure 18.12 Structural characterization of SRB2m with SAXS. (a) Experimental X-ray scattering patterns from SRB2m alone (curve 1), SRB2m-sulfohodamine B complex (curve 2), and SRB2m with PBV (curve 3). (b) *Ab initio* models of SRB2m with (1) and without (2) PBV. The monomer model of SRB2m is shown in (b1) in magenta, and the dimer model of SRB2m is shown in (b2), with one monomer in magenta and the other one in green. The right and bottom slides show the model rotated by 90° around the *y* and *x* axes, respectively (scale bar = 2 nm). (Werner *et al*. 2009 [298]. Reproduced with permission of Elsevier.)

structures of four different tetrapod-shaped DNA molecules [301]. One of the tetrapodna with a larger R_g was found to induce more cytokine secretion. It was hypothesized that dissociation of dsDNA in the central connecting region of the tetrapod results in the larger R_g and the subsequent increased immunostimulatory activity.

18.5 Time-Resolved Synchrotron X-ray Footprinting in Studying the Folding of Nucleic Acid Structures

In addition to SAXS, another method that has been commonly used for probing nucleic acid structures is footprinting. The term "footprinting" describes a method for studying the sequence-specific binding of proteins to DNA [302, 303]. By utilizing DNase, a nuclease that can easily digest DNA exposed to the solvent but unable to cut DNA that is "protected" by proteins, scientists are able to see the protective "footprint" of the binding protein on the DNA sequence. Since then, footprinting has been used to examine ligand binding or conformational changes by quantifying the solvent accessibility of the backbone of nucleic acid through their sensitivity to enzymatic or chemical cleavage. The protected region with less solvent accessibility can be revealed by separating the reaction products using gel electrophoresis. Free linear nucleic acid molecules usually give bands with even intensity, since the probability of each nucleotide being attacked by nuclease is

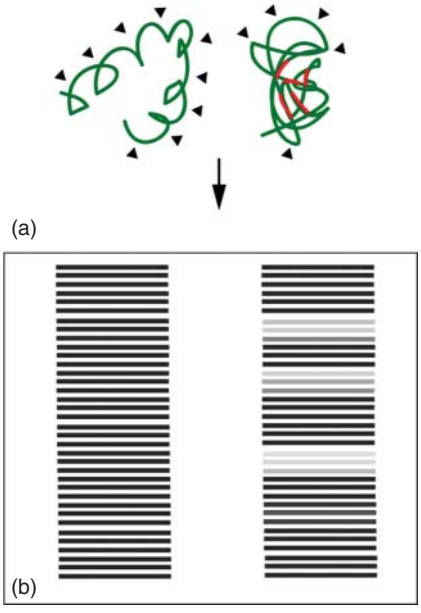

Figure 18.13 Hydroxyl radical footprinting of RNA. (a) Hydroxyl radicals (•OH) generated by synchrotron radiation attack backbones of unfolded (top left) and folded (top right) RNA molecules in solution. Owing to the formation of tertiary structures, folded RNA exhibits decreased solvent accessibility compared to unfolded RNA. Sequences buried inside the folded structures (shown in red) have less chance to be attacked by •OH, giving rise to less cleavage in these buried regions. (b) Cleavage products can be separated by gel electrophoresis. Unfolded RNA is cleaved uniformly and shows a ladder of bands with even intensity on the gel (bottom left). In contrast, the bands of folded RNA have several regions with less intensity, corresponding to sequences with decreased solvent accessibility and inhibited cleavage.

almost the same. In contrast, the "protected" nucleic acid molecules will show decreased intensity of certain bands, corresponding to the protected region that has less chance to be attacked (Figure 18.13).

Among different types of reagents used for footprinting assays, such as endonuclease DNase I and hydroxyl radical (•OH), •OH has proved to have significant advantages over other reagents, because it has van der Waals surface area and solvent properties similar to those of water molecules. Therefore, •OH is an ideal radical for probing solvent accessibility with single nucleotide resolution. It can react with DNA and RNA by attacking the phosphodiester backbone, and it is insensitive to base sequence or secondary structure. In the early days, •OH was usually generated by Fenton reaction using Fe–EDTA, or from homolytic dissociation of peroxynitrous acid. However, these two reagents commonly used to generate •OH could not be used for time-resolved footprinting with timescales of less than seconds. With the development of synchrotron facilities, researchers have been able to use high-flux synchrotron X-ray beam to generate •OH from water in milliseconds and map the dynamic structures of nucleic acid at subsecond timescale. High flux provided by white light X-ray beams shortened the reaction time for generating •OH tremendously and has led to many breakthroughs in the study of nucleic acid folding process. Compared with SAXS, which is commonly used for obtaining the overall shape of nucleic acid, synchrotron-generated hydroxyl radical footprinting provides a unique approach for probing RNA conformations with single nucleotide resolution.

Among many large RNA molecules, the *Tetrahymena thermophilia* ribozyme is one the best characterized ribozymes with regard to its structure, folding pathways, and enzymatic activity (Figure 18.14a). It is composed of at least three domains of tertiary structure, "P4–P6," "P1–P3," and "P3 + P7–P9." It was found

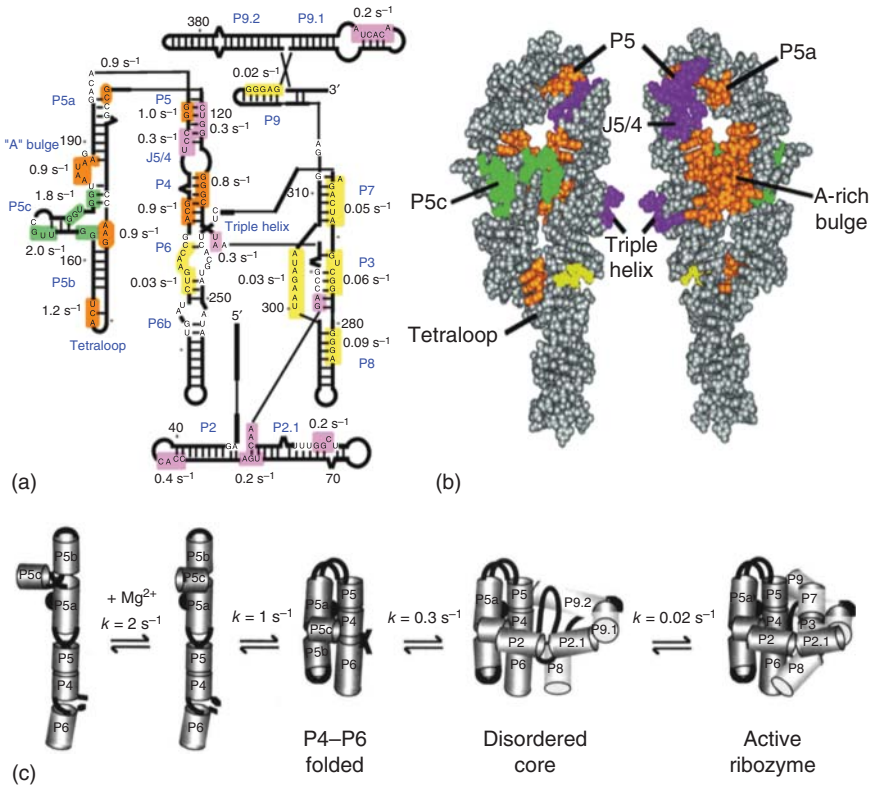

Figure 18.14 Synchrotron-generated hydroxyl radical footprinting of the *Tetrahymena* L-21 ribozyme. (a) Secondary structure of the ribozyme. Lettered bases were protected from hydroxyl radical cleavage in 10 mM Mg^{2+} at 42°C. Colored regions are regions with similar folding rates, with their rate constants labeled in numbers. (b) Front and back views of a space-filling model of the P4–P6 domain of the ribozyme. (c) A model for the early steps of the Mg^{2+}-dependent folding of the ribozyme. Residues in P5c were protected most rapidly, followed by the nucleotides in the interior of the P4–P6 domain. In comparison, nucleotides involved in interactions with P2–P2.1 and the P3–P9 domain were protected more slowly, and the ordering of the catalytic core occurred even slower, on the timescale of several minutes. (Adapted from Sclavi *et al*. 1998 [304].)

that these individual domains can reassemble into active ribozyme when they are mixed together. Of the three domains, P4–P6 is the only domain that can fold independently (Figure 18.14b). In addition to the folding mechanism for individual domains [305, 306], the complete folding pathway of Mg^{2+}-dependent *Tetrahymena* ribozyme was characterized by several groups using synchrotron footprinting (Figure 18.14c) [304, 307–310]. They determined the folding kinetics by monitoring the changes in solvent accessibility of individual sites as a function of time. The folding process starts with rapid collapse of the RNA molecule into a partially disordered state, followed by a slow step allowing RNA to rearrange into active structures. It was revealed that the most stable domain of the tertiary structure formed within 3 s, followed by sequential folding of

the peripheral helices and the catalytic core on the timescale of minutes. The different effects of monovalent and divalent ions on the rates and hierarchy of *Tetrahymena* ribozyme folding has been studied by Uchida *et al*. [311] and Shcherbakova *et al*. [312] The *Tetrahymena* ribozyme folds to the same overall structure in the presence of either divalent or monovalent ions. However, the rate of folding is much faster and the solvent accessibility of nucleotides is more in monovalent ions than in divalent ions.

Unlike many large RNAs such as the aforementioned *Tetrahymena* ribozyme, the *Azoarcus* group I ribozyme is small in size. It retains the conserved catalytic core common to all other group I ribozymes, but lacks the peripheral domains that stabilize folding intermediates of the large ribozymes. Rangan *et al.* used synchrotron footprinting to probe the assembly and tertiary folding of this ribozyme [313]. Their findings revealed that tertiary folding occurred much faster for *Azoarcus* ribozyme than other group I ribozymes, and assembly of helices happened before the formation of native tertiary structures. A 3D model was constructed based on the analysis, revealing distinct structural features that explained the unusual stability and cooperative folding of *Azoarcus* ribozyme.

More recently, the use of synchrotron footprinting has been extended to studying noncanonical DNA structures [314], characterizing the dynamics of ribosome RNA folding [315] and mapping structures of ribosomes and ribozymes inside cells [316, 317]. In particular, the development of *in vivo* footprinting using synchrotron radiation has provided structural biology with a new method for capturing the structural dynamics of nucleic acid in the cellular environment. With increasing interest in acquiring and interpreting biomolecular information at physiological conditions, synchrotron footprinting can be a valuable tool that paves the way for a large number of biological and biomaterial applications.

18.6 Synchrotron-Based Methods in Studying DNA-Functionalized Nanomaterials

The discovery of DNA double-helical structures has laid the cornerstone for molecular biology. The intrinsic programmable property of DNA to form Watson–Crick base pairs with complementary strands has also been shown to be a foundation for bionanotechnology. With a diameter of about 2 nm and a repeat of helical pitch every 3.4–3.6 nm, the stiff helical DNA molecule has proved to be a versatile building block for "bottom-up" constructions of complex structures with subnanometer precision [29, 30, 186, 318–322]. The concept of using approximately 200 short staple DNA strands to direct the folding of a long scaffold strand into the desired two- and three-dimensional nanostructures gave birth to the field of DNA origami [32]. Since then, there has been an explosive growth in the fabrication of custom-shaped structures comprised of DNA molecules. Since the early advent of individual DNA objects such as a quadrilateral and a cube [323, 324], numerous artificial DNA structures have been constructed, including tubes, 2D [32, 34, 35, 325–339] and 3D lattices, and

assemblies [33, 340–344]. Moreover, because of the special electronic, magnetic, and photonic properties of programmable assembly of nanomaterials, as well as the potential use of 3D DNA crystal lattices in structure biology for protein structure determination, many structural DNA and DNA origamis have been used as platforms to arrange functional nanomaterials such as metals [345], nanoparticles [321, 346–355], quantum dots [356–358], carbon nanotubes [359, 360], and proteins [318–320, 361–368] at the nanometer scale. It has been demonstrated that DNA-based nanomaterials can assemble into periodic macroscopic structures in a well-controlled manner, with the precision of such ordered structures being difficult to achieve by other means of fabrication.

The structures of DNA assembly and DNA-templated assembly of nanoparticles are usually characterized by atomic force microscopy (AFM) [326], transmission electron microscopy (TEM), and cryo-electron microscope (cryo-EM) [369]. These instruments are preferred because of their high spatial resolution that is comparable to the size of DNA and nanoparticles. However, despite their ability to provide high-resolution images of a sample, due to the drying process required during sample preparation and imaging conditions under high vacuum, the morphology of 3D superlattices may be distorted or destroyed as dehydration of the DNA would affect the structural integrity of the DNA. This limitation often resulted in many 3D assemblies of DNA-functionalized materials not suitable to be imaged directly using these imaging methods. Instead, SAXS is often used for providing structural information about 3D superlattice structures in solution. Here, we review the recent progress in using SAXS for characterizing DNA-based and DNA-functionalized 3D nanomaterial assemblies.

18.6.1 Use of SAXS for Characterizing DNA Nanostructures

Anderson *et al.* reported a covalently closed DNA nanocage constructed with eight 75-mer DNA strands assembled into a truncated octahedron structure by going through the annealing process followed by DNA ligation [344]. The 3D structure of the assembled DNA cage was characterized by SAXS in combination with single-particle image reconstruction based on cryo-TEM. SAXS data showed that the sample contained very well-defined hollow particles, and the inner diameter and overall dimensions of the nanocages were predicted with reasonable accuracy. The predicted model from SAXS data is also in good agreement with cryo-TEM analysis.

In building 3D structures with DNA origami, Anderson *et al.* created a DNA box by folding six DNA origami sheets along a long circular ssDNA. The lid was designed with a lock–key system, which could be opened in the presence of externally supplied DNA "keys." The structure of this DNA box was characterized by SAXS, cryo-EM, and AFM. SAXS measurement provided useful information about the native structure of the DNA origami box in solution without sample fixation. SAXS analysis indicated the sample was in well-defined shape and adopted a hollow structure. Theoretical modeling of the box derived from SAXS data gave the overall dimensions and wall thickness close to the expected size and was consistent with the size observed by cryo-EM.

18.6.2 Use of SAXS for Studying DNA-Functionalized Nanoparticle 3D Assemblies

Because of the unique physical and chemical properties exhibited by nanoarchitectures built from well-organized nanoparticle building blocks, assembling nanoparticles into designed 2D and 3D structures has attracted a lot of interest in scientific research [370]. Numerous attempts have been made to precisely control the localization of nanoparticles in 3D assemblies, including using small organic molecules, synthetic polymers, proteins [371], and DNA-functionalized nanoparticles as building blocks for use in therapeutic, spectroscopic, catalytic, and material applications. Among different strategies, DNA has been shown to be the most versatile material for positioning nanoparticles in a desired way due to its good programmability and tunability. Since the initial report on DNA-directed self-assembly of gold nanoparticles by Mirkin *et al*. [29] and Alivisatos *et al*. [30], a variety of nanostructures based on DNA-functionalized nanoparticles have been reported. The optical, electrical properties of these nanostructures have been utilized for colorimetric diagnosis, nanophotonic circuits, and high-efficiency energy-harvesting devices [22–24, 372, 373]. The SAXS, with its ability to provide information on parameters of crystalline lattices and quantitatively determine interparticle distances in periodic structures, served as one of the most widely used techniques for characterizing 3D nanoassemblies [374]. In a SAXS spectrum, the peak positions and relative heights indicate the structure of the assemblies, while the degree of ordering within the structure is reflected by peak numbers and their widths.

The electrical properties of gold nanoparticle assemblies linked by DNA were reported by Park *et al*. [375]. Since the electrical properties of gold nanoparticle assemblies are highly influenced by interparticle distances, the distance between the particles is of great interest to researchers. Such a property was characterized by SAXS in combination with other techniques. It was observed that in the solution, the distance between particles increased as the length of the linker DNA increased. However, for dried aggregates, the interparticle distance was no longer dependent on the length of the linker. The electrical properties of DNA-protected nanoparticles were also quite different from those of gold nanoparticle films, with the former behaving more as semiconductors and the latter exhibiting metallic behavior.

To understand the optical properties of DNA-linked gold nanoparticle aggregates and their relationships with structures at nanometer scale, Storhoff *et al.* characterized the aggregates formed by two types of DNA-functionalized gold nanoparticles linked by DNA linkers with three different lengths, 24, 48, and 72 base pairs (Figure 18.15) [376]. They observed that at room temperature, nanoparticle assemblies exhibited plasmon frequency changes that had an inverse relationship with the lengths of linkers. Twenty-four base linked aggregates showed the largest change, while the frequency shift for the 72 base linked gold nanoparticles was the smallest. However, upon annealing at temperatures near the melting temperature of the DNA, the plasmon frequency of longer DNA-linked assemblies (48 and 72 base pairs) further red shifted until they were similar to the assemblies formed with the shorter linkers (24 base pairs). This

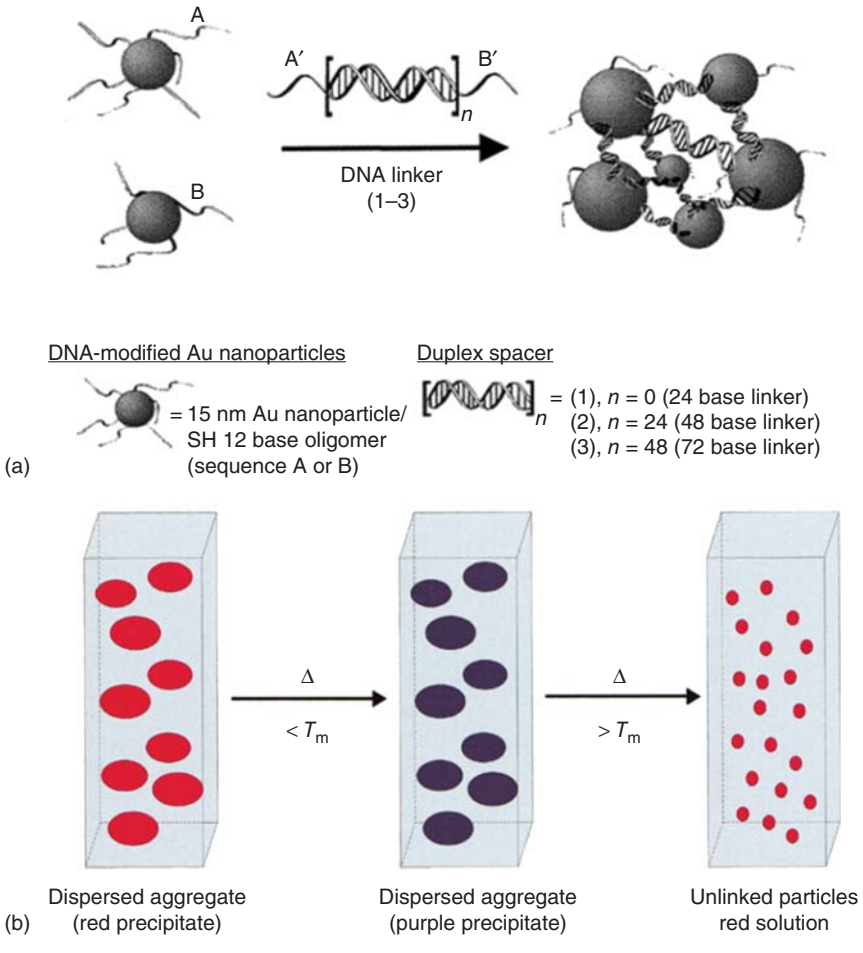

Figure 18.15 Optical properties of DNA-linked gold nanoparticle aggregates. (a) DNA-linked gold nanoparticle assemblies from 24, 48, and 72 base pair linkers; (b) regardless of linker length, DNA-linked aggregates turned into purple aggregates upon annealing at temperatures near the melting temperature of the DNA, and completely dissociated into unlinked particles as temperature was raised above the melting temperature. (Storhoff *et al*. 2000 [376]. Reproduced with permission of American Chemical Society.)

result suggested that under preannealing conditions, the 48 and 72 base linked aggregates formed kinetically stable structures, and these structures could be thermally transformed into thermodynamic aggregates upon annealing. The SAXS characterization showed that the first-order diffraction peak of the long DNA-linked aggregates did not shift upon annealing. This result suggested that the interparticle distance of these DNA-linked aggregates did not change significantly upon annealing. Instead, the optical properties of the assemblies were proved to be dependent on aggregate size rather than oligonucleotide linker length, upon characterization using sedimentation rate, TEM, dynamic light scattering, and UV–vis spectroscopy.

Chi *et al.* characterized the interparticle distance of a dimer of DNA-functionalized gold nanoparticles using synchrotron-based SAXS in combination with molecular simulations [377]. Their results indicated that the separation distance between the two nanoparticles depended on the length of ssDNA linker as well as the number of linkers connecting the nanoparticles. Longer ssDNA linkers resulted in larger intradimer distances, while multiple linkers between two particles led to smaller interparticle distances due to off-axis connections by the linker strands (Figure 18.16).

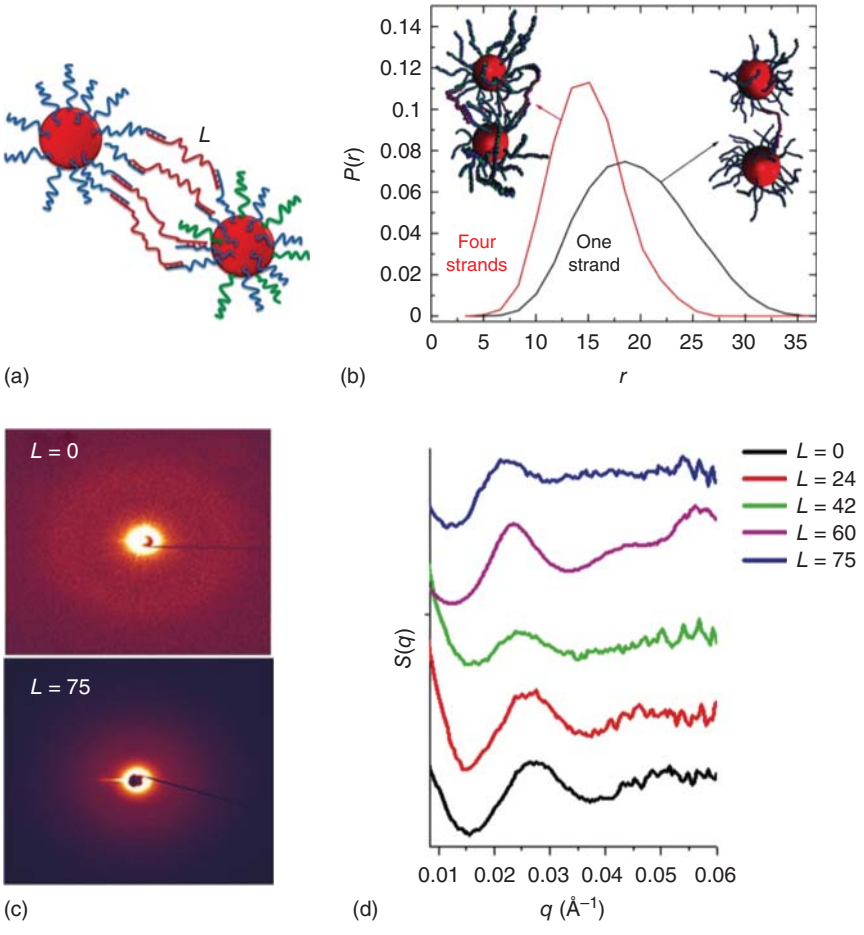

Figure 18.16 (a) Schematic of a dimer of gold nanoparticles connected by multiple ssDNA linkers (pink strand). *L* denotes the number of polythymine bases (T) in the ssDNA linker, excluding the recognition ends. (b) Computed distribution of the surface-to-surface distance *r* for a dimer linked by either one (black line) or four chains (red line) for linker length $L = 10$ bases. (c) Representative 2D SAXS pattern of dimers for $L = 0$ and $L = 75$. (d) Structural factors for the dimer systems with different linker lengths *L*. Monotonic shifts of the first $S(q)$ peak indicate an increase in the interparticle distance with increasing *L*. (Chi *et al*. 2012 [377]. Reproduced with permission of American Chemical Society.)

With the interparticle structure of 3D assemblies from DNA-functionalized nanoparticles thoroughly characterized by SAXS [378], researchers have been able to interpret how interparticle interactions and DNA–nanoparticle interactions can affect the 3D structures of these assemblies. In an early demonstration reported by Park *et al.*, the oligonucleotide-modified nanoparticle assemblies were found to adopt amorphous structures, with local structures exhibiting scattering patterns that revealed body-centered cubic (BCC), face-centered cubic (FCC) or body-centered tetragonal (BCT)-like structures [378]. In the same study, SAXS was used to probe the effects of oligonucleotide components on the assembled structures. Poly-A was found to have higher affinity for gold than poly-T, as poly-T spacer resulted in a significant increase in the interparticle distance. These findings provided useful insights into the structural basis for 3D assemblies for better control over their structures.

In more recent studies, by shortening the length of "sticky ends" of DNA linkers and allowing weaker DNA interactions between particles, Mirkin's and Gang's groups independently showed the formation of 3D crystalline assemblies of gold nanoparticles guided by the interactions between complementary DNA molecules conjugated on the surface of particles [379, 380]. To probe the internal structures of nanoassemblies into superlattices during heating and cooling processes in real time, both groups used SAXS for monitoring the phase behavior of their systems *in situ* (Figure 18.17). In the binary system reported by Gang and coworkers [379], five sets of DNA-capped gold nanoparticles were prepared. Each set contained two kinds of gold nanoparticles modified with different DNA molecules. At room temperature, nanoparticles assembled into amorphous structures by DNA hybridization. However, upon heating the assembly to DNA melting temperatures (T_m) and cooling the assembly below T_m, two sets of DNA-modified nanoparticles with longer flexible spacers showed crystalline organization, while systems with shorter DNA spacers remained amorphous. Clear SAXS patterns strongly indicated the reversible formation of BCC crystalline structures and remarkable degrees of long-range ordering during heating and cooling cycles (Figure 18.17b,c). In a parallel study [380], Mirkin's group demonstrated that it was possible to use DNA for directing the assembly of gold nanoparticles into two distinct crystalline structures (Figure 18.17a). By designing a linker sequence that was either self-complementary or non-self-complementary, a single-component system or a binary system could be achieved. Under thermodynamic control, the single-component system was expected to form a close-packed FCC structure with 12 nearest neighbors to maximize the number of hybridized DNA linkages and minimize the energy of the system, while the binary system was predicted to form a non-close-packed BCC structure with 8 nearest neighbors in order to achieve the maximum number of DNA hybridization. Through a careful heating and cooling process, they showed the formation of an FCC crystal using the single-component system. More interestingly, due to the competition between the entropic and enthalpic contributions involved in the assembly process at different temperatures, the binary system was found to form a BCC structure at room temperature, while it formed an FCC structure if it was treated with heating followed by slow cooling. Moreover, besides DNA linkage and

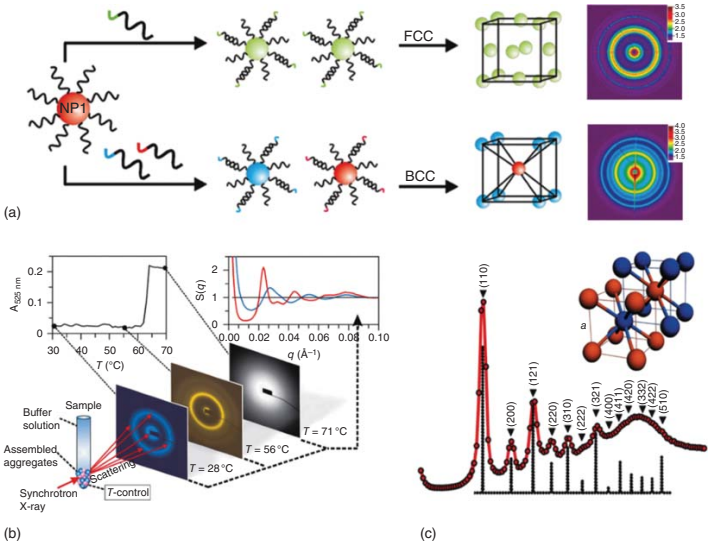

Figure 18.17 (a) Gold nanoparticle–DNA conjugates can be programmed to assemble into single-component assembly system (FCC) using one DNA sequence, or binary-component assembly system (BCC) using two different linkers. (Adapted from Park *et al*. 2008 [380].) (b) A typical example of an *in situ* SAXS measurement for probing the internal structure of gold nanoparticle–DNA conjugates as temperature changes. (c) Structural factors for gold nanoparticle–DNA conjugates with BCC structure. (Panels (b) and (c): Nykypanchuk *et al*. 2008 [379]. Reproduced with permission of Nature Publishing Group.)

temperature, many other variables were also found to participate in affecting the final structure of the DNA–AuNP assembly, such as the flexor between the DNA linker and AuNP, particle size, the sequence and the rigidity of hybridized DNA linkers, and the number of bound linker strands per particle [381, 382]. By varying the length of the DNA hybridization region in the single-component system, it has been demonstrated that the distance between AuNPs in the FCC crystals can be fine-tuned [383]. Longer DNA connections result in increased nanoparticle spacing as well as a decrease in the order of the lattice because the nanoparticles are less spatially constrained. Xiong *et al*. studied the effect of DNA linker length and the number of linkers per particle on the internal structure of DNA–AuNP assembly in a binary system using SAXS [384]. Their findings suggested that linker lengths should be constrained within a limited range for the formation of BCC crystal structure and that the density of linkers on nanoparticles controlled the onset of system crystallization.

Since the discovery of DNA-directed colloidal crystallization, the mechanism of crystal growth has been extensively studied. Macfarlane *et al*. discussed a three-step process for the formation of DNA–AuNP crystals derived from SAXS profiles, collected during the growth of crystal systems [385]. The whole process is composed of initial DNA–AuNP aggregation, formation of small, well-ordered crystalline domains, followed by small crystal–crystal aggregation, and final rearrangement into large crystal systems with long-range order. Luo and coworkers comprehensively studied the process of "soft" crystallization using DNA-capped nanoparticles, and during this process the deformation of soft corona made of DNA on the surface of nanoparticles was found to occur [386–388]. Using SAXS to probe the entire crystallization process in real time and *in situ*, they demonstrated that the soft crystals went through a gradual transition from "wet crystals" to "dry crystals" accompanied by elastic drying-mediated deformation of DNA molecules (Figure 18.18).

To fully understand the parameters involved in crystal assembly, Macfarlane *et al*. found general design rules that can address the control over lattice parameters [390, 391]. By varying particle size, length of DNA linkers, length of spacers, and number of sticky end types, nine different kinds of crystal lattices were obtained and characterized by SAXS under thermodynamic or kinetic controls. This discovery enables researchers to synthesize nanoassemblies in a predicted manner. Meanwhile, there is also an increasing interest in using simulations to characterize the process of DNA-programmable nanoparticle crystallization. Quantitative prediction of the phase behavior of DNA-functionalized colloids has been achieved through computational simulations based on a coarse-grain method [392, 393].

More recently, the concept of DNA–nanoparticle superlattice has been extended to using different types of building blocks, such as anisotropic nanorods, rhombic dodecahedra, and octahedral nanoparticles to synthesize novel crystalline structures [394]. Novel 2D and 3D structures were observed from anisotropic particle assemblies that could not be achieved by the assembly of symmetric spherical particles [395]. Spherical nucleic acid nanoparticle conjugates [396] have also been used as hollow spacers in the construction of nanoparticle superlattices, resulting in new crystalline structures with distinct

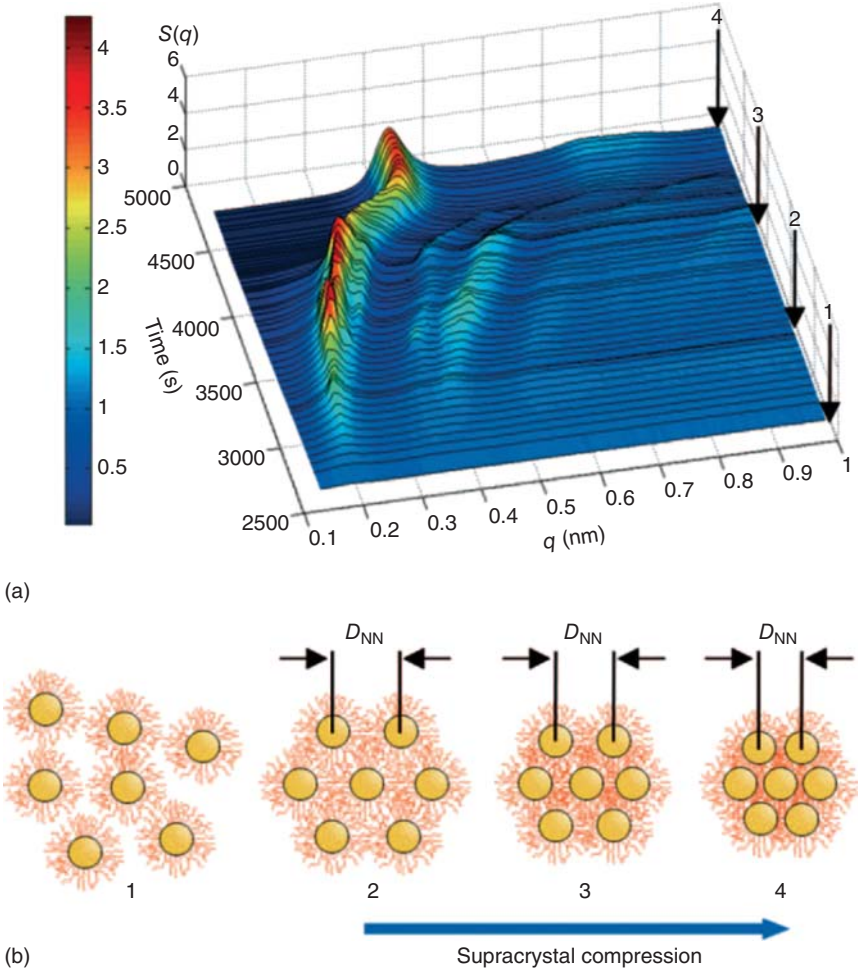

Figure 18.18 Soft crystallization of poly(dT)$_{15}$-capped nanoparticles in the contact-line region. (a) Series of 1D SAXS patterns recorded over drying time. (b) Schematic showing the maintenance of the FCC lattice during corona deformation. (Cheng *et al*. 2010 [389]. Reproduced with permission of John Wiley & Sons.)

symmetries that were difficult to obtain previously [397]. A general approach to functionalize a wide variety of nanoparticles with a dense shell of DNA has been reported, largely expanding the building blocks to nanoparticles of chemical species besides gold [398]. 3D nanoparticle assembly with controllable switching of interparticle distances in the superlattices has also been demonstrated by Maye *et al*. [399] and Xiong *et al*. [400]. Very recently, a topotactic intercalation strategy was reported by Mirkin and coworkers to create nanoparticle superlattices with greater complexity than simple binary systems [401]. This methodology allowed a third nanoparticle to be inserted into predetermined sites in the preformed binary lattice, and led to unique crystal structures with much increased complexity.

The SAXS, as a major tool in characterizing 3D structures of DNA nanostructures and DNA-programmable nanoparticle assemblies, has provided us with a comprehensive understanding of the structures constructed and guides us toward the field of building nanoarchitectures with greater complexity and functionality.

18.7 Synchrotron Radiation for Studying DNA–Lipid Interaction

The structures formed by DNA and lipids have attracted significant interest in the past decade after the discovery that lipids can be used as vehicles to deliver DNA into mammalian cells. As a major type of nonviral vectors, liposomes that are formed by closed bilayer membrane shells of lipids are very promising for gene therapy because they are easy to prepare and less immunogenic than viral vectors. Since the early work of using cationic lipids to form lipid–DNA complexes for gene delivery by Felgner *et al.* [402], tremendous efforts have been devoted to the search for new formulations of liposomes in order to increase the level of gene transfer efficiency. Meanwhile, targeted delivery has been proposed by conjugating lipids with different targeting groups, such as small molecules [403], peptides [404], antibodies [405], and aptamers [406]. To understand how the structures of lipid–DNA complexes would affect their transfection efficiency and uptake mechanism, the SAXS has been used as a major tool to characterize the nanostructures of self-assembled lipid–DNA complexes. These characterizations have helped to establish correlations between the structure of lipid–DNA complexes and their biological function. Moreover, the structural information also has provided deeper insights into rational optimization of formulation and transfection efficiency.

Depending on the lipid composition, the ratio of DNA to lipids, and the solution conditions, lipids and DNA can form different structures in solution. Radler *et al.* used SAXS to characterize the structure of cationic liposomes (CL) in complex with DNA [144]. The liposomes consisted of binary mixtures of neutral lipids dioleoyl phosphatidylcholine (DOPC) and cationic lipids dioleoyl trimethylammonium propane (DOTAP) with a 1: 1 ratio. They observed that addition of either linear λ-phage or plasmid DNA to the CL resulted in a transition from liposomes to a highly ordered multilamellar (L_α^c) structure with DNA sandwiched between cationic bilayers (Figure 18.19a). In a different study, Koltover *et al.* substituted DOPC with dioleoyl phosphatidylethanolamine (DOPE) to form a mixture of DOTAP and DOPC. At certain compositions, addition of DNA molecules into the system led to a completely different structure [407]. DNA was found to be coated by cationic lipid monolayers and form a columnar inverted hexagonal lattice (H_{II}^c) (Figure 18.19b). In addition to the composition and rigidity of the membrane, such different formations of structures were found to depend on the shape of lipid molecules. Because DOTAP and DOPC are cylindrical in shape, a mixture of these two gave zero spontaneous curvature and resulted in a multilamellar structure. However, since DOPE has a cone-like shape, leading to negative curvature, the mixture of DOTAP and DOPE favored the formation of a columnar

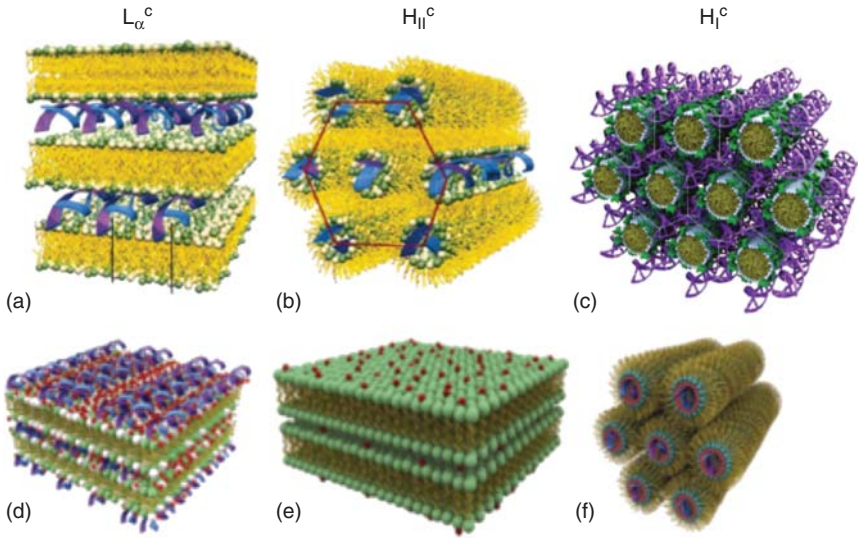

Figure 18.19 Schematics of cationic lipid–DNA (CL–DNA) complexes (a–c) and anionic lipid–DNA (AL–DNA) complexes (d–f). (a) Lamellar $L_\alpha{}^c$ phase of CL–DNA complexes; (b) columnar inverted hexagonal $H_{II}{}^c$ phase of CL–DNA complexes; (c) $H_I{}^c$ phase of CL–DNA complexes, in which tubular lipid micelles arrange in a hexagonal lattice while DNA rods arrange on a honeycomb lattice in the interstices of the lipid micelle arrangement; (d) condensed DNA–ion–AL lamellar structure with alternating layers of DNA and anionic membranes glued together by divalent cations; (e) condensed ion–AL membrane lamellar structure; (f) 2D inverted hexagonal structure of AL–DNA complexes, in which hexagonal arrays of divalent cations coated DNA strands wrapped in the anionic membrane monolayer tubes. (Adapted from Ref. [144, 407–409].)

inverted hexagonal shape. Such findings also explained the correlation between the nanostructure of CL–DNA complexes and transfection efficiency. Liposomes containing DOPE have been found to have good transfection efficiency, since they formed a $H_{II}{}^c$ structure that fused well with the cell membrane, while liposomes containing DOPC and adopting $L_\alpha{}^c$ structures had poor transfection efficiency because they fused poorly with the cell membrane.

Besides monovalent cationic lipids, multivalent cationic lipids have also been reported to form lamellar and micellar conformations in complex with DNA [410–417]. In contrast, self-assembled anionic lipids (ALs) and DNA complexes have been found to organize into different structures than the CL–DNA complex (Figure 18.19d–f) [409]. At low membrane charge densities, AL–DNA formed a lamellar structure of alternating DNA and membrane layers, while at high membrane charge densities, DNA was expelled from the complex and a lamellar stack of membranes was formed. More interestingly, at high concentration of Zn^{2+}, the system formed an inverted hexagonal phase in which DNA strands were coated with divalent cations and wrapped with anionic membrane monolayers to form hexagonal arrays.

In a more recent study, Ewert *et al*. discovered another new shape of CL–DNA complexes [418]. They synthesized a highly charged multivalent cationic

lipid (with 16 positive charges) with a dendritic head group, MVLBG2, and investigated the structure of the lipid–DNA complex by SAXS. At a narrow range of composition around 25 mol% MVLBG2 and 75 mol% DOPC, the complex exhibited the hexagonal phase $\left(H_I^C\right)$, in which hexagonally arranged tubular lipid micelles were surrounded by DNA rods with honeycomb symmetry (Figure 18.19c).

In another recent study, the discovery that short complementary B-form DNA (with 6–20 base pairs in length) could exhibit nematic and columnar liquid crystal phases has led to a study of the packing of short DNA with nonpairing overhangs in CL–DNA complexes [419, 420]. Employing SAXS, Bouxsein *et al*. found that the formation of nematic liquid crystal phases in the CL–DNA system was influenced by many parameters, such as the length of DNA and the length of nonsticky ends. Such structure may find its use in delivery of short anisotropic biomolecules with nanoparticle membranes for gene silencing in the future. As our understanding of the structures of lipid–DNA complexes increases with the help of SAXS, lipid-based delivery approach will be more optimized and better designed for therapeutic applications.

More recently, Angelov *et al.* employed time-resolved SAXS to study the structural changes during uptake of plasmid DNA by cationic lipid nanocarriers [421]. They coupled a rapid-mixing stopped-flow technique to SAXS to achieve 4 ms time resolution, which allowed the capture of structural information at a very early stage. The obtained results suggest that the inner membrane of lipid nanocarriers rearranges its architecture upon loading of the plasmids in less than 150 ms. In addition, Pozzi *et al.* compared the structure and transfection process of multicomponent (MC) lipoplexes and multicomponent envelope-type nanoparticle systems (MENS) [422]. Synchrotron SAXS and AFM revealed that MC lipoplexes form onion-like multilamellar structures, while MENS adopt a core–shell structure with condensed DNA/protamine as the core covered with a lipid shell. They proposed that the structure of the nanocarrier plays a role in the transfection efficiency (TE), since it determines the dissociation and transport process of DNA inside cells. Based on their observation, MENS are found to have a much greater TE than MC lipoplexes, and the molecular mechanism behind such phenomenon is under investigation.

18.8 Summary and Outlook

In this review, we have summarized the progress made in using synchrotron-based spectroscopic techniques for the characterization of nucleic acids and related nucleic-acids-based or -templated nanomaterials. In comparison to the study of other molecules such as organic polymers and proteins, the use synchrotron-based spectroscopic techniques to study nucleic acids is relatively new and cases of study are not as many. Despite this situation, the power of synchrotron-based spectroscopic methods has already been demonstrated to reveal many interesting properties such as the electronic structures of nucleobases and dsDNA, the secondary structure of DNA molecules, the

orientation of surface-bound nucleic acids, the metal-binding sites in nucleic acids, conformations of nucleic acids in solution including intermediates in RNA folding, and noncanonical structures of DNA and RNA molecules. In addition, time-resolved synchrotron X-ray footprinting in studying the folding of nucleic acid structures is also described. Finally, application of synchrotron radiation in studying DNA-based functional materials, including DNA nanostructures, such as DNA 3D origami structures and DNA-functionalized nanoparticle 3D assemblies, as well as DNA–lipid interactions, have also been covered. These results have provided deeper insights into the structure and function of nucleic acids, allowing their applications as building blocks for biochemical, biomedical, and bionanotechnological applications.

With so many synchrotron-based spectroscopic techniques available, the choice of a particular method will depend on molecules to be studied and information to be obtained. To take full advantage of these techniques for nucleic acid research, further exploration of the capability of these methods is required, including optimization of the conditions under which the data are collected, accumulation of reference data for fingerprint comparison, and development of theoretical framework to interpret the results.

With the continuous development of synchrotron facilities aiming at providing light sources with higher flux, higher brightness, and more continuous tunability, these synchrotron-based techniques can find an even wider range of uses as nondestructive, high-resolution, real-time and *in situ* analytical methods in biochemical, biomedical, and nanomaterial characterizations of even more nucleic acids.

Acknowledgments

The Lu group research described in this review is supported by the US Department of Energy (DE-FG02-08ER64568), National Science Foundation (CTS-0120978, CMMI 0749028, and DMR-0117792), and National Institute of Health (GM124316 and MH110975).

References

1 Ebashi, S., Koch, M., and Rubenstein, E. (eds) (1991) *Handbook on Synchrotron Radiation*, vol. 4, North Holland, New York.
2 Tuerk, C. and Gold, L. (1990) Systematic evolution of ligands by exponential enrichment – RNA ligands to bacteriophage-T4 DNA-polymerase. *Science*, **249** (4968), 505–510.
3 Ellington, A.D. and Szostak, J.W. (1990) *In vitro* selection of RNA molecules that bind specific ligands. *Nature*, **346** (6287), 818–822.
4 Joyce, G.F. (1994) *In vitro* evolution of nucleic-acids. *Curr. Opin. Struct. Biol.*, **4** (3), 331–336.
5 Breaker, R.R. (1997) *In vitro* selection of catalytic polynucleotides. *Chem. Rev.*, **97** (2), 371–390.

6 Wilson, D.S. and Szostak, J.W. (1999) *In vitro* selection of functional nucleic acids. *Annu. Rev. Biochem.*, **68**, 611–647.

7 Joyce, G.F. (2004) Directed evolution of nucleic acid enzymes. *Annu. Rev. Biochem.*, **73**, 791–836.

8 Silverman, S.K. (2005) *In vitro* selection, characterization, and application of deoxyribozymes that cleave RNA. *Nucleic Acids Res.*, **33** (19), 6151–6163.

9 Breaker, R.R. and Joyce, G.F. (1994) A DNA enzyme that cleaves RNA. *Chem. Biol.*, **1** (4), 223–229.

10 Santoro, S.W. and Joyce, G.F. (1997) A general purpose RNA-cleaving DNA enzyme. *Proc. Natl. Acad. Sci. U.S.A.*, **94** (9), 4262–4266.

11 Li, J., Zheng, W.C., Kwon, A.H., and Lu, Y. (2000) *In vitro* selection and characterization of a highly efficient Zn(II)-dependent RNA-cleaving deoxyribozyme. *Nucleic Acids Res.*, **28** (2), 481–488.

12 Torabi, S.F., Wu, P., McGhee, C.E., Chen, L., Hwang, K., Zheng, N., Cheng, J., and Lu, Y. (2015) *In vitro* selection of a sodium-specific DNAzyme and its application in intracellular sensing. *Proc. Natl. Acad. Sci. U.S.A.*, **112** (19), 5903–5908.

13 Huang, P.J., Vazin, M., and Liu, J. (2014) *In vitro* selection of a new lanthanide-dependent DNAzyme for ratiometric sensing lanthanides. *Anal. Chem.*, **86** (19), 9993–9999.

14 Saran, R. and Liu, J. (2016) A silver DNAzyme. *Anal. Chem.*, **88** (7), 4014–4020.

15 Liu, J., Cao, Z., and Lu, Y. (2009) Functional nucleic acid sensors. *Chem. Rev.*, **109** (5), 1948–1998.

16 Li, J. and Lu, Y. (2000) A highly sensitive and selective catalytic DNA biosensor for lead ions. *J. Am. Chem. Soc.*, **122** (42), 10466–10467.

17 Liu, J. and Lu, Y. (2007) A DNAzyme catalytic beacon sensor for paramagnetic Cu^{2+} ions in aqueous solution with high sensitivity and selectivity. *J. Am. Chem. Soc.*, **129** (32), 9838–9839.

18 Liu, J.W., Brown, A.K., Meng, X.L., Cropek, D.M., Istok, J.D., Watson, D.B., and Lu, Y. (2007) A catalytic beacon sensor for uranium with parts-per-trillion sensitivity and millionfold selectivity. *Proc. Natl. Acad. Sci. U.S.A.*, **104** (7), 2056–2061.

19 Xiang, Y., Tong, A.J., and Lu, Y. (2009) Abasic site-containing DNAzyme and aptamer for label-free fluorescent detection of Pb^{2+} and adenosine with high sensitivity, selectivity, and tunable dynamic range. *J. Am. Chem. Soc.*, **131** (42), 15352–15357.

20 Hwang, K., Wu, P.W., Kim, T., Lei, L., Tian, S.L., Wang, Y.X., and Lu, Y. (2014) Photocaged DNAzymes as a general method for sensing metal ions in living cells. *Angew. Chem. Int. Ed.*, **53** (50), 13798–13802.

21 Wu, P., Hwang, K., Lan, T., and Lu, Y. (2013) A DNAzyme-gold nanoparticle probe for uranyl ion in living cells. *J. Am. Chem. Soc.*, **135** (14), 5254–5257.

22 Liu, J.W. and Lu, Y. (2003) A colorimetric lead biosensor using DNAzyme-directed assembly of gold nanoparticles. *J. Am. Chem. Soc.*, **125** (22), 6642–6643.

23 Lee, J.H., Wang, Z.D., Liu, J.W., and Lu, Y. (2008) Highly sensitive and selective colorimetric sensors for uranyl (UO_2^{2+}): development and comparison of labeled and label-free DNAzyme-gold nanoparticle systems. *J. Am. Chem. Soc.*, **130** (43), 14217–14226.

24 Wang, Z.D., Lee, J.H., and Lu, Y. (2008) Label-free colorimetric detection of lead ions with a nanomolar detection limit and tunable dynamic range by using gold nanoparticles and DNAzyme. *Adv. Mater.*, **20** (17), 3263–3267.

25 Xiao, Y., Rowe, A.A., and Plaxco, K.W. (2007) Electrochemical detection of parts-per-billion lead via an electrode-bound DNAzyme assembly. *J. Am. Chem. Soc.*, **129** (2), 262–263.

26 Lan, T., Zhang, J., and Lu, Y. (2016) Transforming the blood glucose meter into a general healthcare meter for *in vitro* diagnostics in mobile health. *Biotechnol. Adv.*, **34** (3), 331–341.

27 Zhang, J., Xiang, Y., Wang, M., Basu, A., and Lu, Y. (2016) Dose-dependent response of personal glucose meters to nicotinamide coenzymes: applications to point-of-care diagnostics of many non-glucose targets in a single step. *Angew. Chem. Int. Ed.*, **55** (2), 732–736.

28 Xiang, Y. and Lu, Y. (2011) Using personal glucose meters and functional DNA sensors to quantify a variety of analytical targets. *Nat. Chem.*, **3** (9), 697–703.

29 Mirkin, C.A., Letsinger, R.L., Mucic, R.C., and Storhoff, J.J. (1996) A DNA-based method for rationally assembling nanoparticles into macroscopic materials. *Nature*, **382** (6592), 607–609.

30 Alivisatos, A.P., Johnsson, K.P., Peng, X.G., Wilson, T.E., Loweth, C.J., Bruchez, M.P., and Schultz, P.G. (1996) Organization of "nanocrystal molecules" using DNA. *Nature*, **382** (6592), 609–611.

31 Seeman, N.C. (1982) Nucleic-acid junctions and lattices. *J. Theor. Biol.*, **99** (2), 237–247.

32 Rothemund, P.W.K. (2006) Folding DNA to create nanoscale shapes and patterns. *Nature*, **440** (7082), 297–302.

33 He, Y., Ye, T., Su, M., Zhang, C., Ribbe, A.E., Jiang, W., and Mao, C.D. (2008) Hierarchical self-assembly of DNA into symmetric supramolecular polyhedra. *Nature*, **452** (7184), 198–201.

34 Dietz, H., Douglas, S.M., and Shih, W.M. (2009) Folding DNA into twisted and curved nanoscale shapes. *Science*, **325** (5941), 725–730.

35 Han, D.R., Pal, S., Nangreave, J., Deng, Z.T., Liu, Y., and Yan, H. (2011) DNA origami with complex curvatures in three-dimensional space. *Science*, **332** (6027), 342–346.

36 Adleman, L.M. (1994) Molecular computation of solutions to combinatorial problems. *Science*, **266** (5187), 1021–1024.

37 Braich, R.S., Chelyapov, N., Johnson, C., Rothemund, P.W.K., and Adleman, L. (2002) Solution of a 20-variable 3-SAT problem on a DNA computer. *Science*, **296** (5567), 499–502.

38 Shlyahovsky, B., Li, Y., Lioubashevski, O., Elbaz, J., and Willner, I. (2009) Logic gates and antisense DNA devices operating on a translator nucleic acid scaffold. *ACS Nano*, **3** (7), 1831–1843.

39 Chen, X. and Ellington, A.D. (2010) Shaping up nucleic acid computation. *Curr. Opin. Biotechnol.*, **21** (4), 392–400.
40 Brown, G.S. and Moncton, D.E. (eds) (1991) *Handbook on Synchrotron Radiation*, vol. **3**, North Holland.
41 Margaritondo, G. (1988) *Introduction to Synchrotron Radiation*, Oxford University Press.
42 Stöhr, J. (1992) *NEXAFS Spectroscopy*, Berlin, Springer-Verlag.
43 Chen, J.G. (1997) NEXAFS investigations of transition metal oxides, nitrides, carbides, sulfides and other interstitial compounds. *Surf. Sci. Rep.*, **30** (1–3), 1–152.
44 de Groot, F. (2001) High resolution X-ray emission and X-ray absorption spectroscopy. *Chem. Rev.*, **101** (6), 1779–1808.
45 Rehr, J.J. (2000) Theoretical approaches to X-ray absorption fine structure. *Rev. Mod. Phys.*, **72**, 621–654.
46 Åberg, T. (1967) Theory of X-ray satellites. *Phys. Rev.*, **156** (1), 35–41.
47 Hollander, J.M. and Jolly, W.L. (1970) X-ray photoelectron spectroscopy. *Acc. Chem. Res.*, **3** (6), 193–200.
48 Fadley, C.S. (1984) Angle-resolved X-ray photoelectron-spectroscopy. *Prog. Surf. Sci.*, **16** (3), 275–388.
49 Powell, C.J. and Seah, M.P. (1990) Precision, accuracy, and uncertainty in quantitative surface-analyses by auger-electron spectroscopy and X-ray photoelectron-spectroscopy. *J. Vac. Sci. Technol., A*, **8** (2), 735–763.
50 Gao, L., Li, L.L., Wang, X.L., Wu, P.W., Cao, Y., Liang, B., Li, X., Lin, Y.W., Lu, Y., and Guo, X.F. (2015) Graphene–DNAzyme junctions: a platform for direct metal ion detection with ultrahigh sensitivity. *Chem. Sci.*, **6** (4), 2469–2473.
51 Slinker, J.D., Muren, N.B., Renfrew, S.E., and Barton, J.K. (2011) DNA charge transport over 34 nm. *Nat. Chem.*, **3** (3), 228–233.
52 Sontz, P.A., Muren, N.B., and Barton, J.K. (2012) DNA charge transport for sensing and signaling. *Acc. Chem. Res.*, **45** (10), 1792–1800.
53 Hua, W.J., Gao, B., Li, S.H., Agren, H., and Luo, Y. (2010) Refinement of DNA structures through near-edge X-ray absorption fine structure analysis: applications on guanine and cytosine nucleobases, nucleosides, and nucleotides. *J. Phys. Chem. B*, **114** (41), 13214–13222.
54 Kirtley, S.M., Mullins, O.C., Chen, J., van Elp, J., George, S.J., Chen, C.T., O'Halloran, T., and Cramer, S.P. (1992) Nitrogen chemical structure in DNA and related molecules by X-ray absorption spectroscopy. *Biochim. Biophys. Acta*, **1132** (3), 249–254.
55 Moewes, A., MacNaughton, J., Wilks, R., Lee, J.S., Wettig, S.D., Kraatz, H.B., and Kurmaev, E.Z. (2004) Soft X-ray spectroscopy of nucleobases, B-DNA and ferrocene-proline conjugates. *J. Electron Spectrosc. Relat. Phenom.*, **137**, 817–822.
56 MacNaughton, J., Moewes, A., and Kurmaev, E.Z. (2005) Electronic structure of the nucleobases. *J. Phys. Chem. B*, **109** (16), 7749–7757.
57 Zubavichus, Y., Shaporenko, A., Korolkov, V., Grunze, M., and Zharnikov, M. (2008) X-ray absorption spectroscopy of the nucleotide bases at the carbon, nitrogen, and oxygen K-edges. *J. Phys. Chem. B*, **112** (44), 13711–13716.

58 Hua, W.J., Yamane, H., Gao, B., Jiang, J., Li, S.H., Kato, H.S., Kawai, M., Hatsui, T., Luo, Y., Kosugi, N., and Agren, H. (2010) Systematic study of soft X-ray spectra of poly(Dg)center dot poly(Dc) and poly(Da)center dot poly(Dt) DNA duplexes. *J. Phys. Chem. B*, **114** (20), 7016–7021.

59 MacNaughton, J.B., Moewes, A., Lee, J.S., Wettig, S.D., Kraatz, H.B., Ouyang, L.Z., Ching, W.Y., and Kurmaev, E.Z. (2006) Dependence of DNA electronic structure on environmental and structural variations. *J. Phys. Chem. B*, **110** (32), 15742–15748.

60 Genereux, J.C. and Barton, J.K. (2009) Mechanisms for DNA charge transport. *Chem. Rev.*, **110** (3), 1642–1662.

61 Braun, E., Eichen, Y., Sivan, U., and Ben-Yoseph, G. (1998) DNA-templated assembly and electrode attachment of a conducting silver wire. *Nature*, **391** (6669), 775–778.

62 de Pablo, P.J., Moreno-Herrero, F., Colchero, J., Gomez-Herrero, J., Herrero, P., Baro, A.M., Ordejon, P., Soler, J.M., and Artacho, E. (2000) Absence of dc-conductivity in lambda-DNA. *Phys. Rev. Lett.*, **85** (23), 4992–4995.

63 Yoo, K.H., Ha, D.H., Lee, J.O., Park, J.W., Kim, J., Kim, J.J., Lee, H.Y., Kawai, T., and Choi, H.Y. (2001) Electrical conduction through poly(dA)-poly(dT) and poly(dG)-poly(dC) DNA molecules. *Phys. Rev. Lett.*, **87** (19). doi: 10.1103/physrevlett.87.198102

64 Kasumov, A.Y., Kociak, M., Gueron, S., Reulet, B., Volkov, V.T., Klinov, D.V., and Bouchiat, H. (2001) Proximity-induced superconductivity in DNA. *Science*, **291** (5502), 280–282.

65 Guo, J.H., Kastanov, S., Soderstom, J., Glans, P.A., West, M., Learmonth, T., Chiou, J.W., Luo, Y., Nordgren, J., Smith, K., Pong, W.F., Cheng, H., and Griffiss, J.M. (2010) Electronic structure study of the bases in DNA duplexes by in situ photon-in/photon-out soft X-ray spectroscopy. *J. Electron Spectrosc. Relat. Phenom.*, **181** (2–3), 197–201.

66 Kummer, K., Vyalikh, D.V., Gavrila, G., Preobrajenski, A.B., Kick, A., Bonsch, M., Mertig, M., and Molodtsov, S.L. (2010) Electronic structure of genomic DNA: a photoemission and X-ray absorption study. *J. Phys. Chem. B*, **114** (29), 9645–9652.

67 Johnson, C.W. (1978) Circular dichroism spectroscopy and the vacuum ultraviolet region. *Annu. Rev. Phys. Chem.*, **29** (1), 93–114.

68 Gray, D.M., Johnson, K.H., Vaughan, M.R., Morris, P.A., Sutherland, J.C., and Ratliff, R.L. (1990) The vacuum UV CD bands of repeating DNA sequences are dependent on sequence and conformation. *Biopolymers*, **29** (2), 317–323.

69 Johnson, K.H., Gray, D.M., and Sutherland, J.C. (1991) Vacuum UV CD spectra of homopolymer duplexes and triplexes containing A.T or A.U base pairs. *Nucleic Acids Res.*, **19** (9), 2275–2280.

70 Sutherland, J.C., Griffin, K.P., Keck, P.C., and Takacs, P.Z. (1981) Z-DNA: vacuum ultraviolet circular dichroism. *Proc. Natl. Acad. Sci. U.S.A.*, **78** (8), 4801–4804.

71 Gray, D.M., Ratliff, R.L., and Vaughan, M.R. (1992) Circular-dichroism spectroscopy of DNA. *Methods Enzymol.*, **211**, 389–406.

72 Williams, A.L., Cheong, C., Tinoco, I., and Clark, L.B. (1986) Vacuum ultraviolet circular-dichroism as an indicator of helical handedness in nucleic-acids. *Nucleic Acids Res.*, **14** (16), 6649–6659.

73 Jones, G.R. and Clarke, D.T. (2004) Applications of extended ultra-violet circular dichroism spectroscopy in biology and medicine. *Faraday Discuss.*, **126**, 223–236.

74 Munksgaard, N.L., Holm, A.I.S., Varsano, D., Kadhane, U., Vroenning, H.S., Di, F.R., Rubio, A., and Broendsted, N.S. (2009) Fingerprints of bonding motifs in DNA duplexes of adenine and thymine revealed from circular dichroism: synchrotron radiation experiments and TDDFT calculations. *J. Phys. Chem. B*, **113**, 9614–9619.

75 Holm, A.I.S., Kohler, B., Vroenning, H.S., and Broendsted, N.S. (2010) Synchrotron radiation circular dichroism of various G-quadruplex structures. *Biopolymers*, **93**, 429–433.

76 Holm, A.I.S., Nielsen, L.M., Hoffmann, S.V., and Nielsen, S.B. (2010) Vacuum-ultraviolet circular dichroism spectroscopy of DNA: a valuable tool to elucidate topology and electronic coupling in DNA. *Phys. Chem. Chem. Phys.*, **12** (33), 9581–9596.

77 Holm, A.I.S., Nielsen, L.M., Kohler, B., Hoffmann, S.V., and Nielsen, S.B. (2010) Electronic coupling between cytosine bases in DNA single strands and i-motifs revealed from synchrotron radiation circular dichroism experiments. *Phys. Chem. Chem. Phys.*, **12**, 3426–3430.

78 Nielsen, L.M., Hoffmann, S.V., and Nielsen, S.B. (2012) Probing electronic coupling between adenine bases in RNA strands from synchrotron radiation circular dichroism experiments. *Chem. Commun.*, **48**, 10425–10427.

79 Gao, X.Y., Xing, G.M., Yang, Y.L., Shi, X.L., Liu, R., Chu, W.G., Jing, L., Zhao, F., Ye, C., Yuan, H., Fang, X.H., Wang, C., and Zhao, Y.L. (2008) Detection of trace Hg^{2+} via induced circular dichroism of DNA wrapped around single-walled carbon nanotubes. *J. Am. Chem. Soc.*, **130** (29), 9190–9191.

80 Gurung, S.P., Schwarz, C., Hall, J.P., Cardin, C.J., and Brazier, J.A. (2015) The importance of loop length on the stability of i-motif structures. *Chem. Commun.*, **51** (26), 5630–5632.

81 Wang, J. (2000) From DNA biosensors to gene chips. *Nucleic Acids Res.*, **28** (16), 3011–3016.

82 Nelson, B.P., Grimsrud, T.E., Liles, M.R., Goodman, R.M., and Corn, R.M. (2001) Surface plasmon resonance imaging measurements of DNA and RNA hybridization adsorption onto DNA microarrays. *Anal. Chem.*, **73** (1), 1–7.

83 Katz, E. and Willner, I. (2003) Probing biomolecular interactions at conductive and semiconductive surfaces by impedance spectroscopy: routes to impedimetric immunosensors, DNA-sensors, and enzyme biosensors. *Electroanalysis*, **15** (11), 913–947.

84 Schuck, P. (1997) Use of surface plasmon resonance to probe the equilibrium and dynamic aspects of interactions between biological macromolecules. *Annu. Rev. Biophys. Biomol. Struct.*, **26**, 541–566.

85 Liu, X.S., Zheng, F., Jurgensen, A., Perez-Dieste, V., Petrovykh, D.Y., Abbott, N.L., and Himpsel, F.J. (2007) Self-assembly of biomolecules at surfaces characterized by NEXAFS. *Can. J. Chem.*, **85** (10), 793–800.

86 Fujii, K., Akamatsu, K., and Yokoya, A. (2004) Near-edge X-ray absorption fine structure of DNA nucleobases thin film in the nitrogen and oxygen K-edge region. *J. Phys. Chem. B*, **108** (23), 8031–8035.

87 Furukawa, M., Yamada, T., Katano, S., Kawai, M., Ogasawara, H., and Nilsson, A. (2007) Geometrical characterization of adenine and guanine on Cu(110) by NEXAFS, XPS, and DFT calculation. *Surf. Sci.*, **601** (23), 5433–5440.

88 Seifert, S., Gavrila, G.N., Zahn, D.R.T., and Braun, W. (2007) The molecular orientation of DNA bases on H-passivated Si(111) surfaces investigated by means of near edge X-ray absorption fine structure spectroscopy. *Surf. Sci.*, **601** (11), 2291–2296.

89 O. Plekan, V. Feyer, S. Ptasinska, N. Tsud, V. Chab, V. Matolin, K. C. Prince, Photoemission study of thymidine adsorbed on Au(111) and Cu(110). *J. Phys. Chem. C* 2010, **114** (35), 15036-15041.

90 Herne, T.M. and Tarlov, M.J. (1997) Characterization of DNA probes immobilized on gold surfaces. *J. Am. Chem. Soc.*, **119** (38), 8916–8920.

91 Peterlinz, K.A., Georgiadis, R.M., Herne, T.M., and Tarlov, M.J. (1997) Observation of hybridization and dehybridization of thiol-tethered DNA using two-color surface plasmon resonance spectroscopy. *J. Am. Chem. Soc.*, **119** (14), 3401–3402.

92 Levicky, R., Herne, T.M., Tarlov, M.J., and Satija, S.K. (1998) Using self-assembly to control the structure of DNA monolayers on gold: a neutron reflectivity study. *J. Am. Chem. Soc.*, **120** (38), 9787–9792.

93 Lee, C.Y., Gong, P., Harbers, G.M., Grainger, D.W., Castner, D.G., and Gamble, L.J. (2006) Surface coverage and structure of mixed DNA/alkylthiol monolayers on gold: characterization by XPS, NEXAFS, and fluorescence intensity measurements. *Anal. Chem.*, **78** (10), 3316–3325.

94 Schreiner, S.M., Hatch, A.L., Shudy, D.F., Howard, D.R., Howell, C., Zhao, J.L., Koelsch, P., Zharnikov, M., Petrovykh, D.Y., and Opdahl, A. (2011) Impact of DNA-surface interactions on the stability of DNA hybrids. *Anal. Chem.*, **83** (11), 4288–4295.

95 Mateo-Martía, E., Rogero, C., Briones, C., and Martín-Gago, J.A. (2007) Do peptide nucleic acids form self-assembled monolayers on pyrite surfaces? *Surf. Sci.*, **601** (18), 4195–4199.

96 Cho, E., Brown, A., and Kuech, T.F. (2012) Chemical characterization of DNA-immobilized InAs surfaces using X-ray photoelectron spectroscopy and near-edge X-ray absorption fine structure. *Langmuir*, **28**, 11890–11898.

97 Bertoncini, C.R.A., Meneghini, R., and Tolentino, H. (2010) Nearest-neighbor nitrogen and oxygen distances in the iron(II)–DNA complex studied by extended X-ray absorption fine structure. *Spectrochim. Acta, Part A*, **77** (4), 908–910.

98 Bertoncini, C., Meneghini, R., Cruz, D.Z., Alves, M.C.M., and Tolentino, H. (1999) Studies of Fe(II) and Fe(III)–DNA complexes by XANES spectroscopy. *J. Synchrotron Radiat.*, **6**, 417–418.

99 Andrews, N.C. and Schmidt, P.J. (2007) Iron homeostasis. *Annu. Rev. Physiol.*, **69**, 69–85.

100 Meneghini, R. (1997) Iron homeostasis, oxidative stress, and DNA damage. *Free Radical Biol. Med.*, **23** (5), 783–792.

101 Galaris, D. and Pantopoulos, K. (2008) Oxidative stress and iron homeostasis: mechanistic and health aspects. *Crit. Rev. Clin. Lab. Sci.*, **45** (1), 1–23.

102 Koutmou, K.S., Casiano-Negroni, A., Getz, M.M., Pazicni, S., Andrews, A.J., Penner-Hahn, J.E., Al-Hashimi, H.M., and Fireke, C.A. (2010) NMR and XAS reveal an inner-sphere metal binding site in the P4 helix of the metallo-ribozyme ribonuclease P. *Proc. Natl. Acad. Sci. U.S.A.*, **107** (6), 2479–2484.

103 Lippard, S.J. (1978) Platinum complexes: probes of polynucleotide structure and antitumor drugs. *Acc. Chem. Res.*, **11** (5), 211–217.

104 Sundquist, W.I. and Lippard, S.J. (1990) The coordination chemistry of platinum anticancer drugs and related compounds with DNA. *Coord. Chem. Rev.*, **100**, 293–322.

105 Sherman, S., Gibson, D., Wang, A., and Lippard, S. (1985) X-ray structure of the major adduct of the anticancer drug cisplatin with DNA: *cis*-[$Pt(NH_3)_2$(d(pGpG))]. *Science*, **230** (4724), 412–417.

106 Van der Veer, J.L., Ligtvoet, G.J., Van den Elst, H., and Reedijk, J. (1986) *trans*-Diamminedichloroplatinum(II) can chelate d(GpTpG) via both guanines in a similar fashion as the cis isomer. *J. Am. Chem. Soc.*, **108** (13), 3860–3862.

107 Lepre, C.A., Strothkamp, K.G., and Lippard, S.J. (1987) Synthesis and proton NMR spectroscopic characterization of trans-[$Pt(NH_3)_2$[d(ApGpGpCpCpT)-N7-A(1),N7-G(3)]]. *Biochemistry*, **26** (18), 5651–5657.

108 Gibson, D. and Lippard, S.J. (1987) Synthesis and NMR structural studies of the adduct of *trans*-diamminedichloroplatinum(II) with the DNA fragment d(GpCpG). *Inorg. Chem.*, **26** (14), 2275–2279.

109 Lepre, C.A. and Lippard, S.J. (1990) in *Nucleic Acids and Molecular Biology*, vol. 4 (eds F. Eckstein and D.J. Lilley), Springer-Verlag, Berlin Heidelberg, pp. 9–38.

110 Teo, B.-K., Eisenberger, P., Reed, J., Barton, J.K., and Lippard, S.J. (1978) Study of the binding of *cis*- and *trans*-dichlorodiammineplatinum(II) to calf thymus DNA by extended X-ray absorption fine structure spectroscopy. *J. Am. Chem. Soc.*, **100** (10), 3225–3227.

111 Hitchcock, A.P., Lock, C.J.L., and Pratt, W.M.C. (1982) EXAFS studies of a Pt-dimer-DNA complex. *Inorg. Chim. Acta*, **66** (3), L45–L47.

112 Kobayashi, K., Frohlich, H., Usami, N., Takakura, K., and Le Sech, C. (2002) Enhancement of X-ray-induced breaks in DNA bound to molecules containing platinum: a possible application to hadrontherapy. *Radiat. Res.*, **157** (1), 32–37.

113 Kemsley, J.N., Zaleski, K.L., Chow, M.S., Decker, A., Shishova, E.Y., Wasinger, E.C., Hedman, B., Hodgson, K.O., and Solomon, E.I. (2003) Spectroscopic studies of the interaction of ferrous bleomycin with DNA. *J. Am. Chem. Soc.*, **125** (36), 10810–10821.

114 Bock, L.C., Griffin, L.C., Latham, J.A., Vermaas, E.H., and Toole, J.J. (1992) Selection of single-stranded DNA molecules that bind and inhibit human thrombin. *Nature*, **355** (6360), 564–566.

115 Russo Krauss, I., Merlino, A., Giancola, C., Randazzo, A., Mazzarella, L., and Sica, F. (2011) Thrombin–aptamer recognition: a revealed ambiguity. *Nucleic Acids Res.*, **39** (17), 7858–7867.

116 Smirnov, I.V., Kotch, F.W., Pickering, I.J., Davis, J.T., and Shafer, R.H. (2002) Pb EXAFS studies on DNA quadruplexes: identification of metal ion binding site. *Biochemistry*, **41** (40), 12133–12139.

117 Liu, J. and Lu, Y. (2007) Rational design of "Turn-On" allosteric DNAzyme catalytic beacons for aqueous mercury ions with ultrahigh sensitivity and selectivity. *Angew. Chem. Int. Ed.*, **46** (40), 7587–7590.

118 Lou, X., Zhao, T., Liu, R., Ma, J., and Xiao, Y. (2013) Self-assembled DNA monolayer buffered dynamic ranges of mercuric electrochemical sensor. *Anal. Chem.*, **85** (15), 7574–7580.

119 Wen, S., Zeng, T., Liu, L., Zhao, K., Zhao, Y., Liu, X., and Wu, H.C. (2011) Highly sensitive and selective DNA-based detection of mercury(II) with alpha-hemolysin nanopore. *J. Am. Chem. Soc.*, **133** (45), 18312–18317.

120 Wang, Z., Heon Lee, J., and Lu, Y. (2008) Highly sensitive "turn-on" fluorescent sensor for Hg^{2+} in aqueous solution based on structure-switching DNA. *Chem. Commun.*, **45**, 6005–6007.

121 L. Deng, Z. Zhou, J. Li, T. Li, S. Dong, Fluorescent silver nanoclusters in hybridized DNA duplexes for the turn-on detection of Hg^{2+} ions. *Chem. Commun.*. 2011, **47** (39), 11065-11067.

122 Wu, D., Zhang, Q., Chu, X., Wang, H., Shen, G., and Yu, R. (2010) Ultrasensitive electrochemical sensor for mercury (II) based on target-induced structure-switching DNA. *Biosens. Bioelectron.*, **25** (5), 1025–1031.

123 Xu, X., Wang, J., Jiao, K., and Yang, X. (2009) Colorimetric detection of mercury ion (Hg^{2+}) based on DNA oligonucleotides and unmodified gold nanoparticles sensing system with a tunable detection range. *Biosens. Bioelectron.*, **24** (10), 3153–3158.

124 Dave, N., Chan, M.Y., Huang, P.J., Smith, B.D., and Liu, J. (2010) Regenerable DNA-functionalized hydrogels for ultrasensitive, instrument-free mercury(II) detection and removal in water. *J. Am. Chem. Soc.*, **132** (36), 12668–12673.

125 Zhang, L., Li, T., Li, B., Li, J., and Wang, E. (2010) Carbon nanotube-DNA hybrid fluorescent sensor for sensitive and selective detection of mercury(II) ion. *Chem. Commun.*, **46** (9), 1476–1478.

126 Torabi, S.F. and Lu, Y. (2011) Small-molecule diagnostics based on functional DNA nanotechnology: a dipstick test for mercury. *Faraday Discuss.*, **149**, 125–135; discussion 137-157.

127 Ravel, B., Slimmer, S.C., Meng, X., Wong, G.C.L., and Lu, Y. (2009) EXAFS studies of catalytic DNA sensors for mercury contamination of water. *Radiat. Phys. Chem.*, **78**, S75–S79.

128 Ravel, B. and Newville, M. (2005) ATHENA, ARTEMIS, HEPHAESTUS: data analysis for X-ray absorption spectroscopy using IFEFFIT. *J. Synchrotron Radiat.*, **12** (4), 537–541.

129 Miyake, Y., Togashi, H., Tashiro, M., Yamaguchi, H., Oda, S., Kudo, M., Tanaka, Y., Kondo, Y., Sawa, R., Fujimoto, T., Machinami, T., and Ono, A. (2006) MercuryII-mediated formation of thymine–HgII–thymine base Pairs in DNA duplexes. *J. Am. Chem. Soc.*, **128** (7), 2172–2173.

130 Tanaka, Y., Yamaguchi, H., Oda, S., Kondo, Y., Nomura, M., Kojima, C., and Ono, A. (2006) NMR spectroscopic study of a DNA duplex with mercury-mediated T–T base Pairs. *Nucleosides Nucleotides Nucleic Acids*, **25** (4–6), 613–624.

131 Tanaka, Y., Oda, S., Yamaguchi, H., Kondo, Y., Kojima, C., and Ono, A. (2006) ^{15}N–^{15}N *J*-coupling across Hg^{II}: direct observation of Hg^{II}-mediated T–T base Pairs in a DNA duplex. *J. Am. Chem. Soc.*, **129** (2), 244–245.

132 Wong, G.C.L. and Pollack, L. (2010) Electrostatics of strongly charged biological polymers: ion-mediated interactions and self-organization in nucleic acids and proteins. *Annu. Rev. Phys. Chem.*, **61**, 171–189.

133 Fuoss, R.M., Katchalsky, A., and Lifson, S. (1951) The potential of an infinite rod-like molecule and the distribution of the counter ions. *Proc. Natl. Acad. Sci. U.S.A.*, **37** (9), 579–589.

134 Manning, G.S. (1972) Polyelectrolytes. *Annu. Rev. Phys. Chem.*, **23** (1), 117–140.

135 Anderson, C.F. and Record, M.T. (1990) Ion distributions around DNA and other cylindrical polyions – theoretical descriptions and physical implications. *Annu. Rev. Biophys. Biophys. Chem.*, **19**, 423–465.

136 Draper, D.E., Grilley, D., and Soto, A.M. (2005) Ions and RNA folding. *Annu. Rev. Biophys. Biomol. Struct.*, **34**, 221–243.

137 Sharp, K.A. and Honig, B. (1990) Electrostatic interactions in macromolecules theory and applications. *Annu. Rev. Biophys. Biophys. Chem.*, **19**, 301–332.

138 Angelini, T.E., Liang, H., Wriggers, W., and Wong, G.C.L. (2003) Like-charge attraction between polyelectrolytes induced by counterion charge density waves. *Proc. Natl. Acad. Sci. U.S.A.*, **100** (15), 8634–8637.

139 Needleman, D.J., Ojeda-Lopez, M.A., Raviv, U., Miller, H.P., Wilson, L., and Safinya, C.R. (2004) Higher-order assembly of microtubules by counterions: from hexagonal bundles to living necklaces. *Proc. Natl. Acad. Sci. U.S.A.*, **101**, 16099–16103.

140 Kindt, J., Tzlil, S., Ben-Shaul, A., and Gelbart, W.M. (2001) DNA packaging and ejection forces in bacteriophage. *Proc. Natl. Acad. Sci. U.S.A.*, **98** (24), 13671–13674.

141 Olson, W.K. and Zhurkin, V.B. (2000) Modeling DNA deformations. *Curr. Opin. Struct. Biol.*, **10**, 286–297.

142 Minsky, A. (2004) Information content and complexity in the high-order organization of DNA. *Annu. Rev. Biophys. Biomol. Struct.*, **33** (1), 317–342.

143 Reich, Z., Wachtel, E.J., and Minsky, A. (1994) Liquid-crystalline mesophases of plasmid DNA in bacteria. *Science*, **264** (5164), 1460–1463.

144 Radler, J.O., Koltover, I., Salditt, T., and Safinya, C.R. (1997) Structure of DNA-cationic liposome complexes: DNA intercalation in multilamellar membranes in distinct interhelical packing regimes. *Science*, **275** (5301), 810–814.

145 Evans, H.M., Ahmad, A., Ewert, K., Pfohl, T., Martin-Herranz, A., Bruinsma, R.F., and Safinya, C.R. (2003) Structural polymorphism of DNA-dendrimer complexes. *Phys. Rev. Lett.*, **91** (7), 075501.

146 O. Boussif, F. Lezoualch, M. A. Zanta, M. D. Mergny, D. Scherman, B. Demeneix, J. P. Behr, A versatile vector for gene and oligonucleotide transfer into cells in culture and *in vivo* – polyethylenimine. *Proc. Natl. Acad. Sci. U.S.A.* 1995, **92** (16), 7297-7301.

147 DeRouchey, J., Netz, R.R., and Rädler, J.O. (2005) Structural investigations of DNA–polycation complexes. *Eur. Phys. J. E*, **16** (1), 17–28.

148 KukowskaLatallo, J.F., Bielinska, A.U., Johnson, J., Spindler, R., Tomalia, D.A., and Baker, J.R. (1996) Efficient transfer of genetic material into mammalian cells using Starburst polyamidoamine dendrimers. *Proc. Natl. Acad. Sci. U.S.A.*, **93** (10), 4897–4902.

149 Conwell, C.C., Vilfan, I.D., and Hud, N.V. (2003) Controlling the size of nanoscale toroidal DNA condensates with static curvature and ionic strength. *Proc. Natl. Acad. Sci. U.S.A.*, **100** (16), 9296–9301.

150 Mohammad-Rafiee, F. and Golestanian, R. (2005) Elastic correlations in nucleosomal DNA structure. *Phys. Rev. Lett.*, **94** (23). doi: 10.1103/physrevlett.94.238102

151 Schiessel, H. (2006) The nucleosome: a transparent, slippery, sticky and yet stable DNA–protein complex. *Eur. Phys. J. E*, **19** (3), 251–262.

152 Grønbech-Jensen, N., Mashl, R.J., Bruinsma, R.F., and Gelbart, W.M. (1997) Counterion-induced attraction between rigid polyelectrolytes. *Phys. Rev. Lett.*, **78**, 2477–2480.

153 Zhang, R. and Shklovskii, B.I. (2005) Long-range polarization attraction between two different like-charged macroions. *Phys. Rev. E*, **72** (2), 021405.

154 Kjellander, R. and Marcělja, S. (1984) Correlation and image charge effects in electric double layers. *Chem. Phys. Lett.*, **112** (1), 49–53.

155 Gulbrand, L., Nilsson, L.G., and Nordenskiold, L. (1986) A Monte Carlo simulation study of electrostatic forces between hexagonally packed DNA double helices. *J. Chem. Phys.*, **85**, 6686–6698.

156 Lyubartsev, A.P. and Nordenskiöld, L. (1997) Monte Carlo simulation study of DNA polyelectrolyte properties in the presence of multivalent polyamine ions. *J. Phys. Chem. B*, **101**, 4335–4342.

157 Rouzina, I. and Bloomfield, V.A. (1996) Macroion attraction due to electrostatic correlation between screening counterions. 1. Mobile surface-adsorbed ions and diffuse ion cloud. *J. Phys. Chem.*, **100** (23), 9977–9989.

158 Kanduc, M., Dobnikar, J., and Podgornik, R. (2009) Counterion-mediated electrostatic interactions between helical molecules. *Soft Matter*, **5**, 868–877, **5** (24), 5042.

159 Solis, F.J. and de la Cruz, M.O. (2000) Collapse of flexible polyelectrolytes in multivalent salt solutions. *J. Chem. Phys.*, **112** (4), 2030–2035.

160 Stevens, M.J. (1999) Bundle binding in polyelectrolyte solutions. *Phys. Rev. Lett.*, **82**, 101–104.

161 Arenzon, J.J., Stilck, J.F., and Levin, Y. (1999) Simple model for attraction between like-charged polyion. *Eur. Phys. J. B*, **12**, 79–82.

162 Diehl, A., Carmona, H.A., and Levin, Y. (2001) Counterion correlations and attraction between like-charged macromolecules. *Phys. Rev. E*, **64**, 011804.

163 Deserno, M., Arnold, A., and Holm, C. (2003) Attraction and ionic correlations between charged stiff polyelectrolytes. *Macromolecules*, **36**, 249–259.

164 Wong, G.C.L., Tang, J.X., Lin, A., Li, Y., Janmey, P.A., and Safinya, C.R. (2000) Hierarchical self-assembly of F-actin cationic lipid complexes: stacked three-layer tubule networks. *Science*, **288**, 2035–2039.

165 Tang, J.X., Wong, S., Tran, P.T., and Janmey, P.A. (1996) Counterion induced bundle formation of rodlike polyelectrolytes. *Ber. Bunsen Ges. Phys. Chem.*, **100**, 796–806.

166 Sanders, L.K., Guaqueta, C., Angelini, T.E., Lee, J.W., Slimmer, S.C., Luijten, E., and Wong, G.C.L. (2005) Structure and stability of self-assembled actin–lysozyme complexes in salty water. *Phys. Rev. Lett.*, **95** (10). doi: 10.1103/physrevlett.95.108302

167 Wong, G.C.L., Lin, A., Tang, J.X., Li, Y., Janmey, P.A., and Safinya, C.R. (2003) Lamellar phase of stacked two-dimensional rafts of actin filaments. *Phys. Rev. Lett.*, **91** (1), 018103.

168 Lai, G.H., Coridan, R., Zribi, O.V., Golestanian, R., and Wong, G.C.L. (2007) Evolution of growth modes for polyelectrolyte bundles. *Phys. Rev. Lett.*, **98** (18). doi: 10.1103/physrevlett.98.187802

169 Oosawa, F. (1968) Interaction between parallel rodlike macroions. *Biopolymers*, **6**, 1633–1647.

170 Golestanian, R., Kardar, M., and Liverpool, T.B. (1999) Collapse of Stiff polyelectrolytes due to counterion fluctuations. *Phys. Rev. Lett.*, **82** (22), 4456–4459.

171 Ha, B.Y. and Liu, A.J. (1997) Counterion-mediated attraction between two like-charged rods. *Phys. Rev. Lett.*, **79** (7), 1289–1292.

172 Oosawa, F. (1997) *Polyelectrolytes*, Marcel Dekker, New York.

173 Shklovskii, B.I. (1999) Wigner crystal model of counterion induced bundle formation of rodlike polyelectrolytes. *Phys. Rev. Lett.*, **82** (16), 3268–3271.

174 Lau, A.W.C., Levine, D., and Pincus, P. (2000) Novel electrostatic attraction from plasmon fluctuations. *Phys. Rev. Lett.*, **84** (18), 4116–4119.

175 Moreira, A.G. and Netz, R.R. (2000) Strong-coupling theory for counter-ion distributions. *Europhys. Lett. (EPL)*, **52**, 705–711.

176 Moreira, A.G. and Netz, R.R. (2001) Binding of similarly charged plates with counterions only. *Phys. Rev. Lett.*, **87** (7). doi: 10.1103/physrevlett.87.078301

177 Naji, A. and Netz, R.R. (2005) Counterions at charged cylinders: criticality and universality beyond mean-field theory. *Phys. Rev. Lett.*, **95**. doi: 10.1103/physrevlett.95.185703

178 Naji, A., Jungblut, S., Moreira, A.G., and Netz, R.R. (2005) Electrostatic interactions in strongly coupled soft matter. *Physica A*, **352**, 131–170.

179 Šamaj, L. and Trizac, E. (2011) Counterions at highly charged interfaces: from one plate to like-charge attraction. *Phys. Rev. Lett.*, **106** (7). doi: 10.1103/physrevlett.106.078301
180 Manning, G.S. (1988) Three persistence lengths for a stiff polymer with an application to DNA B–Z junctions. *Biopolymers*, **27**, 1529–1542.
181 Crothers, D.M., Bloomfield, V.A., and Tinoco, I. (2000) *Nucleic Acids: Structures, Properties, and Functions*, University Science Books.
182 Bloomfield, V.A. (1997) DNA condensation by multivalent cations. *Biopolymers*, **44**, 269–282.
183 Williams, M.C. (2007) Stuffing a virus with DNA: dissecting viral genome packaging. *Proc. Natl. Acad. Sci. U.S.A.*, **104**, 11125–11126.
184 Bloomfield, V.A. (1991) Condensation of DNA by multivalent cations: considerations on mechanism. *Biopolymers*, **31**, 1471–1481.
185 Sikorav, J.L., Pelta, J., and Livolant, F. (1994) A liquid-crystalline phase in spermidine-condensed DNA. *Biophys. J.*, **67**, 1387–1392.
186 Seeman, N.C. (1998) DNA nanotechnology: novel DNA constructions. *Annu. Rev. Biophys. Biomol. Struct.*, **27**, 225–248.
187 Pelta, J., Durand, D., Doucet, J., and Livolant, F. (1996) DNA mesophases induced by spermidine: structural properties and biological implications. *Biophys. J.*, **71**, 48–63.
188 Raspaud, E., Durand, D., and Livolant, F. (2005) Interhelical spacing in liquid crystalline spermine and spermidine-DNA precipitates. *Biophys. J.*, **88**, 392–403.
189 Livolant, F. and Leforestier, A. (1996) Condensed phases of DNA: structures and phase transitions. *Prog. Polym. Sci.*, **21** (6), 1115–1164.
190 Mangenot, S., Leforestier, A., Durand, D., and Livolant, F. (2003) X-ray diffraction characterization of the dense phases formed by nucleosome core particles. *Biophys. J.*, **84** (4), 2570–2584.
191 Kornyshev, A.A., Lee, D.J., Leikin, S., and Wynveen, A. (2007) Structure and interactions of biological helices. *Rev. Mod. Phys.*, **79**, 943–996.
192 Pelta, J., Livolant, F., and Sikorav, J.L. (1996) DNA aggregation induced by polyamines and cobalthexamine. *J. Biol. Chem.*, **271**, 5656–5662.
193 Burak, Y., Ariel, G., and Andelman, D. (2003) Onset of DNA aggregation in presence of monovalent and multivalent counterions. *Biophys. J.*, **85**, 2100–2110.
194 Kankia, B.I., Buckin, V., and Bloomfield, V.A. (2001) Hexamminecobalt(III)-induced condensation of calf thymus DNA: circular dichroism and hydration measurements. *Nucleic Acids Res.*, **29**, 2795–2801.
195 Pabit, S.A., Qiu, X.Y., Lamb, J.S., Li, L., Meisburger, S.P., and Pollack, L. (2009) Both helix topology and counter-ion distribution contribute to the more effective charge screening in dsRNA compared with dsDNA. *Nucleic Acids Res.*, **37**, 3887–3896.
196 Podgornik, R., Rau, D.C., and Parsegian, V.A. (1989) The action of interhelical forces on the organization of DNA double helixes: fluctuation-enhanced decay of electrostatic double-layer and hydration forces. *Macromolecules*, **22** (4), 1780–1786.

197 Pollack, L., Anderson, C.F., and Record, M.T. (2011) SAXS studies of ion–nucleic acid interactions ion distributions around DNA and other cylindrical polyions – theoretical descriptions and physical implications. *Annu. Rev. Biophys.*, **40** (1), 225–242.

198 Andresen, K., Das, R., Park, H.Y., Smith, H., Kwok, L.W., Lamb, J.S., Kirkland, E.J., Herschlag, D., Finkelstein, K.D., and Pollack, L. (2004) Spatial distribution of competing ions around DNA in solution. *Phys. Rev. Lett.*, **93** (24). doi: 10.1103/physrevlett.93.248103

199 Das, R., Mills, T.T., Kwok, L.W., Maskel, G.S., and Millett, I.S. (2003) The counterion distribution around DNA probed by solution X-ray scattering. *Phys. Rev. Lett.*, **90** (18). doi: 10.1103/physrevlett.90.188103

200 Pabit, S.A., Finkelstein, K.D., and Pollack, L. (2009) Using anomalous small angle X-ray scattering to probe the ion atmosphere around nucleic acids. *Methods Enzymol.*, **469**, 391–410.

201 Andresen, K., Qiu, X., Pabit, S.A., Lamb, J.S., Park, H.Y., Kwok, L.W., and Pollack, L. (2008) Mono- and trivalent ions around DNA: a small-angle scattering study of competition and interactions. *Biophys. J.*, **95** (1), 287–295.

202 Pabit, S.A., Meisburger, S.P., Li, L., Blose, J.M., Jones, C.D., and Pollack, L. (2010) Counting ions around DNA with anomalous small angle X-ray scattering. *J. Am. Chem. Soc.*, **132**, 16334–16336.

203 Chin, K., Sharp, K.A., Honig, B., and Pyle, A.M. (1999) Calculating the electrostatic properties of RNA provides new insights into molecular interactions and function. *Nat. Struct. Biol.*, **6**, 1055–1061.

204 Duckett, D.R., Murchie, A.I.H., Clegg, R.M., Bassi, G.S., Giraud-Panis, M.J.E., and Lilley, D.M.J. (1997) Nucleic acid structure and recognition. *Biophys. Chem.*, **68**, 53–62.

205 Cate, J.H., Hanna, R.L., and Doudna, J.A. (1997) A magnesium ion core at the heart of a ribozyme domain. *Nat. Struct. Biol.*, **4**, 553–558.

206 Draper, D.E. (2008) RNA folding: thermodynamic and molecular descriptions of the roles of ions. *Biophys. J.*, **95**, 5489–5495.

207 Heilman-Miller, S.L., Thirumalai, D., and Woodson, S.A. (2001) Role of counterion condensation in folding of the *Tetrahymena* ribozyme. I. Equilibrium stabilization by cations. *J. Mol. Biol.*, **306**, 1157–1166.

208 Murthy, V.L. and Rose, G.D. (2000) Is counterion delocalization responsible for collapse in RNA folding? *Biochemistry*, **39**, 14365–14370.

209 Grilley, D., Soto, A.M., and Draper, D.E. (2009) Direct quantitation of Mg^{2+}-RNA interactions by use of a fluorescent dye. *Methods Enzymol.*, **455**, 71–94.

210 Grilley, D., Soto, A.M., and Draper, D.E. (2006) Mg^{2+}-RNA interaction free energies and their relationship to the folding of RNA tertiary structures. *Proc. Natl. Acad. Sci. U.S.A.*, **103**, 14003–14008.

211 Parsegian, V.A., Rand, R.P., Fuller, N.L., and Rau, D.C. (1986) Osmotic stress for the direct measurement of intermolecular forces. *Methods Enzymol.*, **127**, 400–416.

212 Strzelecka, T.E., Davidson, M.W., and Rill, R.L. (1988) Multiple liquid crystal phases of DNA at high concentrations. *Nature*, **331** (6155), 457–460.

213 Leforestier, A. and Livolant, F. (1993) Supramolecular ordering of DNA in the cholesteric liquid crystalline phase: an ultrastructural study. *Biophys. J.*, **65** (1), 56–72.

214 Lai, G.H., Butler, J.C., Zribi, O.V., Smalyukh, I.I., Angelini, T.E., Purdy, K.R., Golestanian, R., and Wong, G.C.L. (2008) Self-organized gels in DNA/F-actin mixtures without crosslinkers: networks of induced nematic domains with tunable density. *Phys. Rev. Lett.*, **101** (21). doi: 10.1103/physrevlett.101.218303

215 Dorschner, R.A., Pestonjamasp, V.K., Tamakuwala, S., Ohtake, T., Rudisill, J., Nizet, V., Agerberth, B., Gudmundsson, G.H., and Gallo, R.L. (2001) Cutaneous injury induces the release of cathelicidin anti-microbial peptides active against group A Streptococcus. *J. Invest. Dermatol.*, **117** (1), 91–97.

216 Gallo, R.L., Ono, M., Povsic, T., Page, C., Eriksson, E., Klagsbrun, M., and Bernfield, M. (1994) Syndecans, cell surface heparan sulfate proteoglycans, are induced by a proline-rich antimicrobial peptide from wounds. *Proc. Natl. Acad. Sci. U.S.A.*, **91** (23), 11035–11039.

217 Harder, J., Bartels, J., Christophers, E., and Schroder, J.M. (1997) A peptide antibiotic from human skin. *Nature*, **387** (6636), 861.

218 Liu, L., Wang, L.N., Jia, H.P., Zhao, C.Q., Heng, H.H.Q., Schutte, B.C., McCray, P.B., and Ganz, T. (1998) Structure and mapping of the human beta-defensin HBD-2 gene and its expression at sites of inflammation. *Gene*, **222** (2), 237–244.

219 Ong, P.Y., Ohtake, T., Brandt, C., Strickland, I., Boguniewicz, M., Ganz, T., Gallo, R.L., and Leung, D.Y.M. (2002) Endogenous antimicrobial peptides and skin infections in atopic dermatitis. *N. Engl. J. Med.*, **347** (15), 1151–1160.

220 Kahlenberg, J.M. and Kaplan, M.J. (2013) Little peptide, big effects: the role of LL-37 in inflammation and autoimmune disease. *J. Immunol.*, **191** (10), 4895–4901.

221 Lande, R., Gregorio, J., Facchinetti, V., Chatterjee, B., Wang, Y.H., Homey, B., Cao, W., Wang, Y.H., Su, B., Nestle, F.O., Zal, T., Mellman, I., Schroder, J.M., Liu, Y.J., and Gilliet, M. (2007) Plasmacytoid dendritic cells sense self-DNA coupled with antimicrobial peptide. *Nature*, **449** (7162), 564–569.

222 Gilliet, M., Cao, W., and Liu, Y.J. (2008) Plasmacytoid dendritic cells: sensing nucleic acids in viral infection and autoimmune diseases. *Nat. Rev. Immunol.*, **8** (8), 594–606.

223 Theofilopoulos, A.N., Gonzalez-Quintial, R., Lawson, B.R., Koh, Y.T., Stern, M.E., Kono, D.H., Beutler, B., and Baccala, R. (2010) Sensors of the innate immune system: their link to rheumatic diseases. *Nat. Rev. Rheumatol.*, **6** (3), 146–156.

224 Heil, F., Hemmi, H., Hochrein, H., Ampenberger, F., Kirschning, C., Akira, S., Lipford, G., Wagner, H., and Bauer, S. (2004) Species-specific recognition of single-stranded RNA via toll-like receptor 7 and 8. *Science*, **303** (5663), 1526–1529.

225 Hemmi, H., Takeuchi, O., Kawai, T., Kaisho, T., Sato, S., Sanjo, H., Matsumoto, M., Hoshino, K., Wagner, H., Takeda, K., and Akira, S. (2000) A toll-like receptor recognizes bacterial DNA. *Nature*, **408** (6813), 740–745.

226 Barrat, F.J., Meeker, T., Gregorio, J., Chan, J.H., Uematsu, S., Akira, S., Chang, B., Duramad, O., and Coffman, R.L. (2005) Nucleic acids of mammalian origin can act as endogenous ligands for toll-like receptors and may promote systemic lupus erythematosus. *J. Exp. Med.*, **202** (8), 1131–1139.

227 Means, T.K., Latz, E., Hayashi, F., Murali, M.R., Golenbock, D.T., and Luster, A.D. (2005) Human lupus autoantibody-DNA complexes activate DCs through cooperation of CD32 and TLR9. *J. Clin Invest.*, **115** (2), 407–417.

228 Lande, R., Ganguly, D., Facchinetti, V., Frasca, L., Conrad, C., Gregorio, J., Meller, S., Chamilos, G., Sebasigari, R., and Riccieri, V. (2011) Neutrophils activate plasmacytoid dendritic cells by releasing self-DNA–peptide complexes in systemic lupus erythematosus. *Sci. Transl. Med.*, **3** (73), 73ra19.

229 Tewary, P., de la Rosa, G., Sharma, N., Rodriguez, L.G., Tarasov, S.G., Howard, O.M.Z., Shirota, H., Steinhagen, F., Klinman, D.M., and Yang, D. (2013) β-Defensin 2 and 3 promote the uptake of self or CpG DNA, enhance IFN-α production by human plasmacytoid dendritic cells, and promote inflammation. *J. Immunol.*, **191** (2), 865–874.

230 Li, Y., Berke, I.C., and Modis, Y. (2012) DNA binding to proteolytically activated TLR9 is sequence − independent and enhanced by DNA curvature. *EMBO J.*, **31** (4), 919–931.

231 Tian, J., Avalos, A.M., Mao, S.-Y., Chen, B., Senthil, K., Wu, H., Parroche, P., Drabic, S., Golenbock, D., and Sirois, C. (2007) Toll-like receptor 9-dependent activation by DNA-containing immune complexes is mediated by HMGB1 and RAGE. *Nat. Immunol.*, **8** (5), 487–496.

232 Yanai, H., Ban, T., Wang, Z.C., Choi, M.K., Kawamura, T., Negishi, H., Nakasato, M., Lu, Y., Hangai, S., and Koshiba, R. (2009) HMGB proteins function as universal sentinels for nucleic-acid-mediated innate immune responses. *Nature*, **462** (7269), 99–103.

233 Gilliet, M. and Lande, R. (2008) Antimicrobial peptides and self-DNA in autoimmune skin inflammation. *Curr. Opin. Immunol.*, **20** (4), 401–407.

234 Schmidt, N.W., Jin, F., Lande, R., Curk, T., Xian, W.J., Lee, C., Frasca, L., Frenkel, D., Dobnikar, J., and Gilliet, M. (2015) Liquid-crystalline ordering of antimicrobial peptide–DNA complexes controls TLR9 activation. *Nat. Mater.*, **14** (7), 696–700.

235 Marcelli, A., Innocenzi, P., Malfatti, L., Newton, M.A., Rau, J.V., Ritter, E., Schade, U., and Xu, W. (2012) IR and X-ray time-resolved simultaneous experiments: an opportunity to investigate the dynamics of complex systems and non-equilibrium phenomena using third-generation synchrotron radiation sources. *J. Synchrotron Radiat.*, **19**, 892–904.

236 Koch, M.H.J., Vachette, P., and Svergun, D.I. (2003) Small-angle scattering: a view on the properties, structures and structural changes of biological macromolecules in solution. *Q. Rev. Biophys.*, **36** (2), 147–227.

237 Svergun, D.I. and Koch, M.H.J. (2003) Small-angle scattering studies of biological macromolecules in solution. *Rep. Prog. Phys.*, **66** (10), 1735–1782.

238 Cech, T.R. and Bass, B.L. (1986) Biological catalysis by RNA. *Annu. Rev. Biochem.*, **55**, 599–629.

239 Altman, S. and Smith, J.D. (1971) Tyrosine tRNA precursor molecule polynucleotide sequence. *Nat. New Biol.*, **233** (36), 35–39.

240 Mandal, M. and Breaker, R.R. (2004) Gene regulation by riboswitches. *Nat. Rev. Mol. Cell Biol.*, **5** (6), 451–463.

241 Serganov, A. and Patel, D.J. (2012) Metabolite recognition principles and molecular mechanisms underlying riboswitch function. *Annu. Rev. Biophys.*, **41**, 343–370.

242 Serganov, A. and Nudler, E. (2013) A decade of riboswitches. *Cell*, **152** (1–2), 17–24.

243 Montange, R.K. and Batey, R.T. (2008) Riboswitches: emerging themes in RNA structure and function. *Annu. Rev. Biophys.*, **37**, 117–133.

244 Brion, P. and Westhof, E. (1997) Hierarchy and dynamics of RNA folding. *Annu. Rev. Biophys. Biomol. Struct.*, **26**, 113–137.

245 Russell, R., Millett, I.S., Doniach, S., and Herschlag, D. (2000) Small angle X-ray scattering reveals a compact intermediate in RNA folding. *Nat. Struct. Biol.*, **7** (5), 367–370.

246 Russell, R., Millettt, I.S., Tate, M.W., Kwok, L.W., Nakatani, B., Gruner, S.M., Mochrie, S.G.J., Pande, V., Doniach, S., Herschlag, D., and Pollack, L. (2002) Rapid compaction during RNA folding. *Proc. Natl. Acad. Sci. U.S.A.*, **99** (7), 4266–4271.

247 Das, R., Kwok, L.W., Millett, I.S., Bai, Y., Mills, T.T., Jacob, J., Maskel, G.S., Seifert, S., Mochrie, S.G.J., Thiyagarajan, P., Doniach, S., Pollack, L., and Herschlag, D. (2003) The fastest global events in RNA folding: electrostatic relaxation and tertiary collapse of the *Tetrahymena* ribozyme. *J. Mol. Biol.*, **332** (2), 311–319.

248 Fang, X., Littrell, K., Yang, X.J., Henderson, S.J., Siefert, S., Thiyagarajan, P., Pan, T., and Sosnick, T.R. (2000) Mg^{2+}-dependent compaction and folding of yeast $tRNA^{Phe}$ and the catalytic domain of the *B. subtilis* RNase P RNA determined by small-angle X-ray scattering. *Biochemistry*, **39** (36), 11107–11113.

249 Xiao, M., Leibowitz, M.J., and Zhang, Y. (2003) Concerted folding of a *Candida* ribozyme into the catalytically active structure posterior to a rapid RNA compaction. *Nucleic Acids Res.*, **31** (14), 3901–3908.

250 Perez-Salas, U.A., Rangan, P., Krueger, S., Briber, R.M., Thirumalai, D., and Woodson, S.A. (2004) Compaction of a bacterial group I ribozyme coincides with the assembly of core helices. *Biochemistry*, **43** (6), 1746–1753.

251 Chauhan, S., Caliskan, G., Briber, R.M., Perez-Salas, U., Rangan, P., Thirumalai, D., and Woodson, S.A. (2005) RNA tertiary interactions mediate native collapse of a bacterial group I ribozyme. *J. Mol. Biol.*, **353** (5), 1199–1209.

252 Baird, N.J., Westhof, E., Qin, H., Pan, T., and Sosnick, T.R. (2005) Structure of a folding intermediate reveals the interplay between core and peripheral elements in RNA folding. *J. Mol. Biol.*, **352** (3), 712–722.

253 Moghaddam, S., Caliskan, G., Chauhan, S., Hyeon, C., Briber, R.M., Thirumalai, D., and Woodson, S.A. (2009) Metal ion dependence of cooperative collapse transitions in RNA. *J. Mol. Biol.*, **393**, 753–764.

254 Mandal, M., Lee, M., Barrick, J.E., Weinberg, Z., Emilsson, G.M., Ruzzo, W.L., and Breaker, R.R. (2004) A glycine-dependent riboswitch that uses

cooperative binding to control gene expression. *Science*, **306**, 275–279, **306** (5701), 1477.

255 Lipfert, J., Das, R., Chu, V.B., Kudaravalli, M., Boyd, N., Herschlag, D., and Doniach, S. (2007) Structural transitions and thermodynamics of a glycine-dependent riboswitch from *Vibrio cholerae*. *J. Mol. Biol.*, **365** (5), 1393–1406.

256 Lipfert, J., Chu, V.B., Bai, Y., Herschlag, D., and Doniach, S. (2007) Low-resolution models for nucleic acids from small-angle X-ray scattering with applications to electrostatic modeling. *J. Appl. Crystallogr.*, **40**, S229–S234.

257 Svergun, D., Barberato, C., and Koch, M.H.J. (1995) CRYSOL – a program to evaluate X-ray solution scattering of biological macromolecules from atomic coordinates. *J. Appl. Crystallogr.*, **28**, 768–773.

258 Konarev, P.V., Volkov, V.V., Sokolova, A.V., Koch, M.H.J., and Svergun, D.I. (2003) PRIMUS: a Windows PC-based system for small-angle scattering data analysis. *J. Appl. Crystallogr.*, **36**, 1277–1282.

259 Chacon, P., Moran, F., Diaz, J.F., Pantos, E., and Andreu, J.M. (1998) Low-resolution structures of proteins in solution retrieved from X-ray scattering with a genetic algorithm. *Biophys. J.*, **74** (6), 2760–2775.

260 Svergun, D.I. (1999) Restoring low resolution structure of biological macromolecules from solution scattering using simulated annealing. *Biophys. J.*, **76**, 2879–2886, **77** (5), 2896.

261 Walther, D., Cohen, F.E., and Doniach, S. (2000) Reconstruction of low-resolution three-dimensional density maps from one-dimensional small-angle X-ray solution scattering data for biomolecules. *J. Appl. Crystallogr.*, **33**, 350–363.

262 Svergun, D.I., Petoukhov, M.V., and Koch, M.H.J. (2001) Determination of domain structure of proteins from X-ray solution scattering. *Biophys. J.*, **80** (6), 2946–2953.

263 Rambo, R.P. and Tainer, J.A. (2010) Improving small-angle X-ray scattering data for structural analyses of the RNA world. *RNA*, **16** (3), 638–646.

264 Patel, D.J., Phan, A.T., and Kuryavyi, V. (2007) Human telomere, oncogenic promoter and 5′-UTR G-quadruplexes: diverse higher order DNA and RNA targets for cancer therapeutics. *Nucleic Acids Res.*, **35** (22), 7429–7455.

265 Kozak, M., Wlodarczyk, A., and Dobek, A. (2009) Synchrotron radiation small angle scattering studies of d(TTAGGG)(4) oligomer in solution. *Radiat. Phys. Chem.*, **78**, S134–S136.

266 Liu, D.S. and Balasubramanian, S. (2003) A proton-fuelled DNA nanomachine. *Angew. Chem. Int. Ed.*, **42** (46), 5734–5736.

267 Modi, S., Swetha, M.G., Goswami, D., Gupta, G.D., Mayor, S., and Krishnan, Y. (2009) A DNA nanomachine that maps spatial and temporal pH changes inside living cells. *Nat. Nanotechnol.*, **4** (5), 325–330.

268 Modi, S., Nizak, C., Surana, S., Halder, S., and Krishnan, Y. (2013) Two DNA nanomachines map pH changes along intersecting endocytic pathways inside the same cell. *Nat. Nanotechnol.*, **8** (6), 459–467.

269 Jin, K.S., Shin, S.R., Ahn, B., Rho, Y., Kim, S.J., and Ree, M. (2009) pH-dependent structures of an i-Motif DNA in solution. *J. Phys. Chem. B*, **113**, 1852–1856.

270 Xiang, Y. and Lu, Y. (2013) An invasive DNA approach toward a general method for portable quantification of metal ions using a personal glucose meter. *Chem. Commun.*, **49** (6), 585–587.

271 Xiang, Y., Wang, Z.D., Xing, H., and Lu, Y. (2013) Expanding DNAzyme functionality through enzyme cascades with applications in single nucleotide repair and tunable DNA-directed assembly of nanomaterials. *Chem. Sci.*, **4** (1), 398–404.

272 Torabi, S.F. and Lu, Y. (2014) Functional DNA nanomaterials for sensing and imaging in living cells. *Curr. Opin. Biotechnol.*, **28C**, 88–95.

273 Xiang, Y. and Lu, Y. (2014) DNA as sensors and imaging agents for metal ions. *Inorg. Chem.*, **53** (4), 1925–1942.

274 Xing, H., Hwang, K., Li, J., Torabi, S.F., and Lu, Y. (2014) DNA aptamer technology for personalized medicine. *Curr. Opin. Chem. Eng.*, **4**, 79–87.

275 Wang, R., Zhu, G., Mei, L., Xie, Y., Ma, H., Ye, M., Qing, F.L., and Tan, W. (2014) Automated modular synthesis of aptamer-drug conjugates for targeted drug delivery. *J. Am. Chem. Soc.*, **136** (7), 2731–2734.

276 McManus, S.A. and Li, Y.F. (2013) Turning a kinase deoxyribozyme into a sensor. *J. Am. Chem. Soc.*, **135** (19), 7181–7186.

277 Padmanabhan, K., Padmanabhan, K.P., Ferrara, J.D., Sadler, J.E., and Tulinsky, A. (1993) The structure of alpha-thrombin inhibited by a 15-mer single-stranded-DNA aptamer. *J. Biol. Chem.*, **268** (24), 17651–17654.

278 Convery, M.A., Rowsell, S., Stonehouse, N.J., Ellington, A.D., Hirao, I., Murray, J.B., Peabody, D.S., Phillips, S.E.V., and Stockley, P.G. (1998) Crystal structure of an RNA aptamer protein complex at 2.8 angstrom resolution. *Nat. Struct. Biol.*, **5** (2), 133–139.

279 Rowsell, S., Stonehouse, N.J., Convery, M.A., Adams, C.J., Ellington, A.D., Hirao, I., Peabody, D.S., Stockley, P.G., and Phillips, S.E.V. (1998) Crystal structures of a series of RNA aptamers complexed to the same protein target. *Nat. Struct. Biol.*, **5** (11), 970–975.

280 Baugh, C., Grate, D., and Wilson, C. (2000) 2.8 angstrom crystal structure of the malachite green aptamer. *J. Mol. Biol.*, **301** (1), 117–128.

281 Nix, J., Sussman, D., and Wilson, C. (2000) The 1.3 angstrom crystal structure of a biotin-binding pseudoknot and the basis for RNA molecular recognition. *J. Mol. Biol.*, **296** (5), 1235–1244.

282 Sussman, D., Nix, J.C., and Wilson, C. (2000) The structural basis for molecular recognition by the vitamin B-12 RNA aptamer. *Nat. Struct. Biol.*, **7** (1), 53–57.

283 Huang, D.B., Vu, D., Cassiday, L.A., Zimmerman, J.M., Maher, L.J., and Ghosh, G. (2003) Crystal structure of NF-kappa B $(p50)_2$ complexed to a high-affinity RNA aptamer. *Proc. Natl. Acad. Sci. U.S.A.*, **100** (16), 9268–9273.

284 Tereshko, V., Skripkin, E., and Patel, D.J. (2003) Encapsulating streptomycin within a small 40-mer RNA. *Chem. Biol.*, **10** (2), 175–187.

285 Horn, W.T., Convery, M.A., Stonehouse, N.J., Adams, C.J., Liljas, L., Phillips, S.E.V., and Stockley, P.G. (2004) The crystal structure of a high affinity RNA stem-loop complexed with the bacteriophage MS2 capsid: further challenges in the modeling of ligand–RNA interactions. *RNA*, **10** (11), 1776–1782.

286 Moorthy, A.K., Huang, D.B., Wang, V.Y., Vu, D., and Ghosh, G. (2007) X-ray structure of a NF-kappaB p50/RelB/DNA complex reveals assembly of multiple dimers on tandem kappaB sites. *J. Mol. Biol.*, **373** (3), 723–734.

287 Long, S.B., Long, M.B., White, R.R., and Sullenger, B.A. (2008) Crystal structure of an RNA aptamer bound to thrombin. *RNA*, **14** (12), 2504–2512.

288 Huang, R.H., Fremont, D.H., Diener, J.L., Schaub, R.G., and Sadler, J.E. (2009) A structural explanation for the antithrombotic activity of ARC1172, a DNA aptamer that binds von Willebrand factor domain A1. *Structure*, **17** (11), 1476–1484.

289 Nomura, Y., Sugiyama, S., Sakamoto, T., Miyakawa, S., Adachi, H., Takano, K., Murakami, S., Inoue, T., Mori, Y., Nakamura, Y., and Matsumura, H. (2010) Conformational plasticity of RNA for target recognition as revealed by the 2.15 angstrom crystal structure of a human IgG-aptamer complex. *Nucleic Acids Res.*, **38** (21), 7822–7829.

290 Krauss, I.R., Merlino, A., Giancola, C., Randazzo, A., Mazzarella, L., and Sica, F. (2011) Thrombin-aptamer recognition: a revealed ambiguity. *Nucleic Acids Res.*, **39** (17), 7858–7867.

291 Krauss, I.R., Merlino, A., Randazzo, A., Novellino, E., Mazzarella, L., and Sica, F. (2012) High-resolution structures of two complexes between thrombin and thrombin-binding aptamer shed light on the role of cations in the aptamer inhibitory activity. *Nucleic Acids Res.*, **40** (16), 8119–8128.

292 Someya, T., Baba, S., Fujimoto, M., Kawai, G., Kumasaka, T., and Nakamura, K. (2012) Crystal structure of Hfq from *Bacillus subtilis* in complex with SELEX-derived RNA aptamer: insight into RNA-binding properties of bacterial Hfq. *Nucleic Acids Res.*, **40** (4), 1856–1867.

293 Nowakowski, J., Shim, P.J., Prasad, G.S., Stout, C.D., and Joyce, G.F. (1999) Crystal structure of an 82-nucleotide RNA–DNA complex formed by the 10–23 DNA enzyme. *Nat. Struct. Biol.*, **6** (2), 151–156.

294 Kim, H.K., Liu, J.W., Li, J., Nagraj, N., Li, M.X., Pavot, C.M.B., and Lu, Y. (2007) Metal-dependent global folding and activity of the 8–17 DNAzyme studied by fluorescence resonance energy transfer. *J. Am. Chem. Soc.*, **129** (21), 6896–6902.

295 Kim, H.K., Rasnik, I., Liu, J.W., Ha, T.J., and Lu, Y. (2007) Dissecting metal ion-dependent folding and catalysis of a single DNAzyme. *Nat. Chem. Biol.*, **3** (12), 763–768.

296 He, Y. and Lu, Y. (2011) Metal-ion-dependent folding of a uranyl-specific DNAzyme: insight into function from fluorescence resonance energy transfer studies. *Chem. Eur. J.*, **17** (49), 13732–13742.

297 Liu, J. and Lu, Y. (2002) FRET study of a trifluorophore-labeled DNAzyme. *J. Am. Chem. Soc.*, **124** (51), 15208–15216.

298 Werner, A., Konarev, P.V., Svergun, D.I., and Hahn, U. (2009) Characterization of a fluorophore binding RNA aptamer by fluorescence correlation

spectroscopy and small angle X-ray scattering. *Anal. Biochem.*, **389** (1), 52–62.

299 Reinstein, O., Yoo, M., Han, C., Palmo, T., Beckham, S.A., Wilce, M.C., and Johnson, P.E. (2013) Quinine binding by the cocaine-binding aptamer. Thermodynamic and hydrodynamic analysis of high-affinity binding of an off-target ligand. *Biochemistry*, **52** (48), 8652–8662.

300 Mohri, K., Nishikawa, M., Takahashi, N., Shiomi, T., Matsuoka, N., Ogawa, K., Endo, M., Hidaka, K., Sugiyama, H., Takahashi, Y., and Takakura, Y. (2012) Design and development of nanosized DNA assemblies in polypod-like structures as efficient vehicles for immunostimulatory CpG motifs to immune cells. *ACS Nano*, **6** (7), 5931–5940.

301 Sanada, Y., Sakamoto, S., Shiomi, T., Okobira, T., Mylonas, E., Ohta, N., Yagi, N., Nishikawa, M., Akiba, I., Takakura, Y., and Sakurai, K. (2014) X-ray scattering from immunostimulatory tetrapod-shaped DNA in aqueous solution to explore its biological activity-conformation relationship. *J. Phys. Chem. B*, **118** (35), 10373–10379.

302 Galas, D.J. and Schmitz, A. (1978) DNAse footprinting: a simple method for the detection of protein–DNA binding specificity. *Nucleic Acids Res.*, **5** (9), 3157–3170.

303 Schmitz, A. and Galas, D.J. (1980) Sequence-specific interactions of the tight-binding I12-X86 lac repressor with non-operator DNA. *Nucleic Acids Res.*, **8** (3), 487–506.

304 Sclavi, B., Sullivan, M., Chance, M.R., Brenowitz, M., and Woodson, S.A. (1998) RNA folding at millisecond intervals by synchrotron hydroxyl radical footprinting. *Science*, **279** (5358), 1940–1943.

305 Deras, M.L., Brenowitz, M., Ralston, C.Y., Chance, M.R., and Woodson, S.A. (2000) Folding mechanism of the *Tetrahymena* ribozyme P4–P6 domain. *Biochemistry*, **39** (36), 10975–10985.

306 Silverman, S.K., Deras, M.L., Woodson, S.A., Scaringe, S.A., and Cech, T.R. (2000) Multiple folding pathways for the P4–P6 RNA domain. *Biochemistry*, **39** (40), 12465–12475.

307 Sclavi, B., Woodson, S., Sullivan, M., Chance, M.R., and Brenowitz, M. (1997) Time-resolved synchrotron X-ray "footprinting", a new approach to the study of nucleic acid structure and function: application to protein–DNA interactions and RNA folding. *J. Mol. Biol.*, **266** (1), 144–159.

308 Sclavi, B., Woodson, S., Sullivan, M., Chance, M., and Brenowitz, M. (1998) Following the folding of RNA with time-resolved synchrotron X-ray footprinting. *Methods Enzymol.*, **295**, 379–402.

309 Ralston, C.Y., Sclavi, B., Brenowitz, M., Sullivan, M., and Chance, M.R. (2000) The early folding intermediates of the *Tetrahymena* ribozyme are kinetically trapped. *J. Biomol. Struct. Dyn.*, 195–200.

310 Ralston, C.Y., Sclavi, B., Sullivan, M., Deras, M.L., Woodson, S.A., Chance, M.R., and Brenowitz, M. (2000) Time-resolved synchrotron X-ray footprinting and its application to RNA folding. *Methods Enzymol.*, **317**, 353–368.

311 Uchida, T., Takamoto, K., He, Q., Chance, M.R., and Brenowitz, M. (2003) Multiple monovalent ion-dependent pathways for the folding of the L-21 *Tetrahymena* thermophila ribozyme. *J. Mol. Biol.*, **328**, 463–478.

312 Shcherbakova, I., Gupta, S., Chance, M.R., and Brenowitz, M. (2004) Monovalent ion-mediated folding of the *Tetrahymena* thermophila ribozyme. *J. Mol. Biol.*, **342** (5), 1431–1442.

313 Rangan, P., Masquida, B., Westhof, E., and Woodson, S.A. (2003) Assembly of core helices and rapid tertiary folding of a small bacterial group I ribozyme. *Proc. Natl. Acad. Sci. U.S.A.*, **100** (4), 1574–1579.

314 Swinger, K.K. and Rice, P.A. (2004) IHF and HU: flexible architects of bent DNA. *Curr. Opin. Struct. Biol.*, **14** (1), 28–35.

315 Nguyenle, T., Laurberg, M., Brenowitz, M., and Noller, H.F. (2006) Following the dynamics of changes in solvent accessibility of 16 S and 23 S rRNA during ribosomal subunit association using synchrotron-generated hydroxyl radicals. *J. Mol. Biol.*, **359** (5), 1235–1248.

316 Adilakshmi, T., Lease, R.A., and Woodson, S.A. (2006) Hydroxyl radical footprinting *in vivo*: mapping macromolecular structures with synchrotron radiation. *Nucleic Acids Res.*, **34** (8), e64.

317 Adilakshmi, T., Soper, S.F.C., and Woodson, S.A. (2009) Structural analysis of RNA in living cells by *in vivo* synchrotron X-ray footprinting. *Methods Enzymol.*, **468**, 239–258.

318 Lee, J.H., Wong, N.Y., Tan, L.H., Wang, Z., and Lu, Y. (2010) Controlled alignment of multiple proteins and nanoparticles with nanometer resolution via backbone-modified phosphorothioate DNA and bifunctional linkers. *J. Am. Chem. Soc.*, **132** (26), 8906–8908.

319 Wong, N.Y., Xing, H., Tan, L.H., and Lu, Y. (2013) Nano-encrypted Morse code: a versatile approach to programmable and reversible nanoscale assembly and disassembly. *J. Am. Chem. Soc.*, **135** (8), 2931–2934.

320 Wong, N.Y., Zhang, C., Tan, L.H., and Lu, Y. (2011) Site-specific attachment of proteins onto a 3D DNA tetrahedron through backbone-modified phosphorothioate DNA. *Small*, **7** (10), 1427–1430.

321 Lee, J.H., Wernette, D.P., Yigit, M.V., Liu, J., Wang, Z., and Lu, Y. (2007) Site-specific control of distances between gold nanoparticles using phosphorothioate anchors on DNA and a short bifunctional molecular fastener. *Angew. Chem. Int. Ed.*, **46** (47), 9006–9010.

322 Loweth, C.J., Caldwell, W.B., Peng, X.G., Alivisatos, A.P., and Schultz, P.G. (1999) DNA-based assembly of gold nanocrystals. *Angew. Chem. Int. Ed.*, **38** (12), 1808–1812.

323 Chen, J.H. and Seeman, N.C. (1991) Synthesis from DNA of a molecule with the connectivity of a cube. *Nature*, **350** (6319), 631–633.

324 Chen, J.H., Kallenbach, N.R., and Seeman, N.C. (1989) A specific quadrilateral synthesized from DNA branched junctions. *J. Am. Chem. Soc.*, **111** (16), 6402–6407.

325 Li, X.J., Yang, X.P., Qi, J., and Seeman, N.C. (1996) Antiparallel DNA double crossover molecules as components for nanoconstruction. *J. Am. Chem. Soc.*, **118** (26), 6131–6140.

326 Liu, W.Y., Zhong, H., Wang, R.S., and Seeman, N.C. (2011) Crystalline two-dimensional DNA-origami arrays. *Angew. Chem. Int. Ed.*, **50** (1), 264–267.

327 Hogberg, B., Liedl, T., and Shih, W.M. (2009) Folding DNA origami from a double-stranded source of scaffold. *J. Am. Chem. Soc.*, **131** (26), 9154–9155.
328 Yan, H., LaBean, T.H., Feng, L.P., and Reif, J.H. (2003) Directed nucleation assembly of DNA tile complexes for barcode-patterned lattices. *Proc. Natl. Acad. Sci. U.S.A.*, **100** (14), 8103–8108.
329 Ke, Y.G., Douglas, S.M., Liu, M.H., Sharma, J., Cheng, A.C., Leung, A., Liu, Y., Shih, W.M., and Yan, H. (2009) Multilayer DNA origami packed on a square lattice. *J. Am. Chem. Soc.*, **131** (43), 15903–15908.
330 Endo, M., Hidaka, K., Kato, T., Namba, K., and Sugiyama, H. (2009) DNA prism structures constructed by folding of multiple rectangular arms. *J. Am. Chem. Soc.*, **131** (43), 15570–15571.
331 Andersen, E.S., Dong, M., Nielsen, M.M., Jahn, K., Subramani, R., Mamdouh, W., Golas, M.M., Sander, B., Stark, H., Oliveira, C.L.P., Pedersen, J.S., Birkedal, V., Besenbacher, F., Gothelf, K.V., and Kjems, J. (2009) Self-assembly of a nanoscale DNA box with a controllable lid. *Nature*, **459** (7243), 73–76.
332 Andersen, E.S., Dong, M.D., Nielsen, M.M., Jahn, K., Lind-Thomsen, A., Mamdouh, W., Gothelf, K.V., Besenbacher, F., and Kjems, J. (2008) DNA origami design of dolphin-shaped structures with flexible tails. *ACS Nano*, **2** (6), 1213–1218.
333 Ke, Y.G., Sharma, J., Liu, M.H., Jahn, K., Liu, Y., and Yan, H. (2009) Scaffolded DNA origami of a DNA tetrahedron molecular container. *Nano Lett.*, **9** (6), 2445–2447.
334 Douglas, S.M., Marblestone, A.H., Teerapittayanon, S., Vazquez, A., Church, G.M., and Shih, W.M. (2009) Rapid prototyping of 3D DNA-origami shapes with caDNAno. *Nucleic Acids Res.*, **37** (15), 5001–5006.
335 Pound, E., Ashton, J.R., Becerril, H.A., and Woolley, A.T. (2009) Polymerase chain reaction based scaffold preparation for the production of thin, branched DNA origami nanostructures of arbitrary sizes. *Nano Lett.*, **9** (12), 4302–4305.
336 Kuzuya, A. and Komiyama, M. (2009) Design and construction of a box-shaped 3D-DNA origami. *Chem. Commun.*, **28**, 4182–4184.
337 Liedl, T., Hogberg, B., Tytell, J., Ingber, D.E., and Shih, W.M. (2010) Self-assembly of three-dimensional prestressed tensegrity structures from DNA. *Nat. Nanotechnol.*, **5** (7), 520–524.
338 Han, D.R., Pal, S., Liu, Y., and Yan, H. (2010) Folding and cutting DNA into reconfigurable topological nanostructures. *Nat. Nanotechnol.*, **5** (10), 712–717.
339 Shih, W.M. and Lin, C.X. (2010) Knitting complex weaves with DNA origami. *Curr. Opin. Struct. Biol.*, **20** (3), 276–282.
340 Du, S.M. and Seeman, N.C. (1992) Synthesis of a DNA knot containing both positive and negative nodes. *J. Am. Chem. Soc.*, **114** (24), 9652–9655.
341 Du, S.M., Stollar, B.D., and Seeman, N.C. (1995) A synthetic DNA molecule in 3 knotted topologies. *J. Am. Chem. Soc.*, **117** (4), 1194–1200.
342 Zhang, Y.W. and Seeman, N.C. (1994) Construction of a DNA-truncated octahedron. *J. Am. Chem. Soc.*, **116** (5), 1661–1669.

343 Shih, W.M., Quispe, J.D., and Joyce, G.F. (2004) A 1.7-kilobase single-stranded DNA that folds into a nanoscale octahedron. *Nature*, **427** (6975), 618–621.

344 Andersen, F.F., Knudsen, B., Oliveira, C.L.P., Frohlich, R.F., Kruger, D., Bungert, J., Agbandje-McKenna, M., McKenna, R., Juul, S., Veigaard, C., Koch, J., Rubinstein, J.L., Guldbrandtsen, B., Hede, M.S., Karlsson, G., Andersen, A.H., Pedersen, J.S., and Knudsen, B.R. (2008) Assembly and structural analysis of a covalently closed nano-scale DNA cage. *Nucleic Acids Res.*, **36** (4), 1113–1119.

345 Yang, H. and Sleiman, H.F. (2008) Templated synthesis of highly stable, electroactive, and dynamic metal–DNA branched junctions. *Angew. Chem. Int. Ed.*, **47** (13), 2443–2446.

346 Ding, B.Q., Deng, Z.T., Yan, H., Cabrini, S., Zuckermann, R.N., and Bokor, J. (2010) Gold nanoparticle self-similar chain structure organized by DNA origami. *J. Am. Chem. Soc.*, **132** (10), 3248–3249.

347 Pal, S., Deng, Z.T., Ding, B.Q., Yan, H., and Liu, Y. (2010) DNA-origami-directed self-assembly of discrete silver-nanoparticle architectures. *Angew. Chem. Int. Ed.*, **49** (15), 2700–2704.

348 Acuna, G.P., Bucher, M., Stein, I.H., Steinhauer, C., Kuzyk, A., Holzmeister, P., Schreiber, R., Moroz, A., Stefani, F.D., Liedl, T., Simmel, F.C., and Tinnefeld, P. (2012) Distance dependence of single-fluorophore quenching by gold nanoparticles studied on DNA origami. *ACS Nano*, **6** (4), 3189–3195.

349 Pal, S., Varghese, R., Deng, Z.T., Zhao, Z., Kumar, A., Yan, H., and Liu, Y. (2011) Site-specific synthesis and *in situ* immobilization of fluorescent silver nanoclusters on DNA nanoscaffolds by use of the tollens reaction. *Angew. Chem. Int. Ed.*, **50** (18), 4176–4179.

350 Zhao, W.A., Gao, Y., Kandadai, S.A., Brook, M.A., and Li, Y.F. (2006) DNA polymerization on gold nanoparticles through rolling circle amplification: towards novel scaffolds for three-dimensional periodic nanoassemblies. *Angew. Chem. Int. Ed.*, **45** (15), 2409–2413.

351 Shen, X.B., Asenjo-Garcia, A., Liu, Q., Jiang, Q., de Abajo, F.J.G., Liu, N., and Ding, B.Q. (2013) Three-dimensional plasmonic chiral tetramers assembled by DNA origami. *Nano Lett.*, **13** (5), 2128–2133.

352 Sharma, J., Chhabra, R., Andersen, C.S., Gothelf, K.V., Yan, H., and Liu, Y. (2008) Toward reliable gold nanoparticle patterning on self-assembled DNA nanoscaffold. *J. Am. Chem. Soc.*, **130** (25), 7820–7821.

353 Stearns, L.A., Chhabra, R., Sharma, J., Liu, Y., Petuskey, W.T., Yan, H., and Chaput, J.C. (2009) Template-directed nucleation and growth of inorganic nanoparticles on DNA scaffolds. *Angew. Chem. Int. Ed.*, **48** (45), 8494–8496.

354 Hung, A.M., Micheel, C.M., Bozano, L.D., Osterbur, L.W., Wallraff, G.M., and Cha, J.N. (2010) Large-area spatially ordered arrays of gold nanoparticles directed by lithographically confined DNA origami. *Nat. Nanotechnol.*, **5** (2), 121–126.

355 Shen, X.B., Song, C., Wang, J.Y., Shi, D.W., Wang, Z.A., Liu, N., and Ding, B.Q. (2012) Rolling up gold nanoparticle-dressed DNA origami into three-dimensional plasmonic chiral nanostructures. *J. Am. Chem. Soc.*, **134** (1), 146–149.

356 Wang, R.S., Nuckolls, C., and Wind, S.J. (2012) Assembly of heterogeneous functional nanomaterials on DNA origami scaffolds. *Angew. Chem. Int. Ed.*, **51** (45), 11325–11327.

357 Ko, S.H., Gallatin, G.M., and Liddle, J.A. (2012) Nanomanufacturing with DNA origami: factors affecting the kinetics and yield of quantum dot binding. *Adv. Funct. Mater.*, **22** (5), 1015–1023.

358 Bui, H., Onodera, C., Kidwell, C., Tan, Y., Graugnard, E., Kuang, W., Lee, J., Knowlton, W.B., Yurke, B., and Hughes, W.L. (2010) Programmable periodicity of quantum dot arrays with DNA origami nanotubes. *Nano Lett.*, **10** (9), 3367–3372.

359 Maune, H.T., Han, S.P., Barish, R.D., Bockrath, M., Goddard, W.A., Rothemund, P.W.K., and Winfree, E. (2010) Self-assembly of carbon nanotubes into two-dimensional geometries using DNA origami templates. *Nat. Nanotechnol.*, **5** (1), 61–66.

360 Chen, Y., Liu, H.P., Ye, T., Kim, J., and Mao, C.D. (2007) DNA-directed assembly of single-wall carbon nanotubes. *J. Am. Chem. Soc.*, **129** (28), 8696–8697.

361 Douglas, S.M., Chou, J.J., and Shih, W.M. (2007) DNA-nanotube-induced alignment of membrane proteins for NMR structure determination. *Proc. Natl. Acad. Sci. U.S.A.*, **104** (16), 6644–6648.

362 Derr, N.D., Goodman, B.S., Jungmann, R., Leschziner, A.E., Shih, W.M., and Reck-Peterson, S.L. (2012) Tug-of-war in motor protein ensembles revealed with a programmable DNA origami scaffold. *Science*, **338** (6107), 662–665.

363 Chhabra, R., Sharma, J., Ke, Y.G., Liu, Y., Rinker, S., Lindsay, S., and Yan, H. (2007) Spatially addressable multiprotein nanoarrays templated by aptamer-tagged DNA nanoarchitectures. *J. Am. Chem. Soc.*, **129** (34), 10304–10305.

364 Kuzyk, A., Laitinen, K.T., and Torma, P. (2009) DNA origami as a nanoscale template for protein assembly. *Nanotechnology*, **20** (23), 235305.

365 Kuzuya, A., Kimura, M., Numajiri, K., Koshi, N., Ohnishi, T., Okada, F., and Komiyama, M. (2009) Precisely programmed and robust 2D streptavidin nanoarrays by using periodical nanometer-scale wells embedded in DNA origami assembly. *ChemBioChem*, **10** (11), 1811–1815.

366 Nakata, E., Liew, F.F., Uwatoko, C., Kiyonaka, S., Mori, Y., Katsuda, Y., Endo, M., Sugiyama, H., and Morii, T. (2012) Zinc-finger proteins for site-specific protein positioning on DNA-origami structures. *Angew. Chem. Int. Ed.*, **51** (10), 2421–2424.

367 Sacca, B., Meyer, R., Erkelenz, M., Kiko, K., Arndt, A., Schroeder, H., Rabe, K.S., and Niemeyer, C.M. (2010) Orthogonal protein decoration of DNA origami. *Angew. Chem. Int. Ed.*, **49** (49), 9378–9383.

368 Shen, W.Q., Zhong, H., Neff, D., and Norton, M.L. (2009) NTA directed protein nanopatterning on DNA origami nanoconstructs. *J. Am. Chem. Soc.*, **131** (19), 6660–6661.

369 Bai, X.C., Martin, T.G., Scheres, S.H.W., and Dietz, H. (2012) Cryo-EM structure of a 3D DNA-origami object. *Proc. Natl. Acad. Sci. U.S.A.*, **109** (49), 20012–20017.

370 Wang, Y.F., Wang, Y., Breed, D.R., Manoharan, V.N., Feng, L., Hollingsworth, A.D., Weck, M., and Pine, D.J. (2012) Colloids with valence and specific directional bonding. *Nature*, **491** (7422), 51–55.

371 Aili, D., Gryko, P., Sepulveda, B., Dick, J.A.G., Kirby, N., Heenan, R., Baltzer, L., Liedberg, B., Ryan, M.P., and Stevens, M.M. (2011) Polypeptide folding-mediated tuning of the optical and structural properties of gold nanoparticle assemblies. *Nano Lett.*, **11** (12), 5564–5573.

372 Liu, J.W. and Lu, Y. (2004) Accelerated color change of gold nanoparticles assembled by DNAzymes for simple and fast colorimetric Pb^{2+} detection. *J. Am. Chem. Soc.*, **126** (39), 12298–12305.

373 Liu, J. and Lu, Y. (2005) Stimuli-responsive disassembly of nanoparticle aggregates for light-up colorimetric sensing. *J. Am. Chem. Soc.*, **127** (36), 12677–12683.

374 Lu, C.G., Akey, A.J., Dahlman, C.J., Zhang, D.T., and Herman, I.P. (2012) Resolving the growth of 3D colloidal nanoparticle superlattices by real-time small-angle X-ray scattering. *J. Am. Chem. Soc.*, **134** (45), 18732–18738.

375 Park, S.-J., Lazarides, A.A., Mirkin, C.A., Brazis, P.W., Kannewurf, C.R., and Letsinger, R.L. (2000) The electrical properties of gold nanoparticle assemblies linked by DNA. *Angew. Chem. Int. Ed.*, **39** (21), 3845–3848.

376 Storhoff, J.J., Lazarides, A.A., Mucic, R.C., Mirkin, C.A., Letsinger, R.L., and Schatz, G.C. (2000) What controls the optical properties of DNA-linked gold nanoparticle assemblies? *J. Am. Chem. Soc.*, **122** (19), 4640–4650.

377 Chi, C., Vargas-Lara, F., Tkachenko, A.V., Starr, F.W., and Gang, O. (2012) Internal structure of nanoparticle dimers linked by DNA. *ACS Nano*, **6** (8), 6793–6802.

378 Park, S.J., Lazarides, A.A., Storhoff, J.J., Pesce, L., and Mirkin, C.A. (2004) The structural characterization of oligonucleotide-modified gold nanoparticle networks formed by DNA hybridization. *J. Phys. Chem. B*, **108** (33), 12375–12380.

379 Nykypanchuk, D., Maye, M.M., van der Lelie, D., and Gang, O. (2008) DNA-guided crystallization of colloidal nanoparticles. *Nature*, **451** (7178), 549–552.

380 Park, S.Y., Lytton-Jean, A.K.R., Lee, B., Weigand, S., Schatz, G.C., and Mirkin, C.A. (2008) DNA-programmable nanoparticle crystallization. *Nature*, **451** (7178), 553–556.

381 Macfarlane, R.J., Thaner, R.V., Brown, K.A., Zhang, J., Lee, B., Nguyen, S.T., and Mirkin, C.A. (2014) Importance of the DNA "bond" in programmable nanoparticle crystallization. *Proc. Natl. Acad. Sci. U.S.A.*, **111** (42), 14995–15000.

382 Senesi, A.J., Eichelsdoerfer, D.J., Brown, K.A., Lee, B., Auyeung, E., Choi, C.H., Macfarlane, R.J., Young, K.L., and Mirkin, C.A. (2014) Oligonucleotide flexibility dictates crystal quality in DNA-programmable nanoparticle superlattices. *Adv. Mater.*, **26** (42), 7235–7240.

383 Hill, H.D., Macfarlane, R.J., Senesi, A.J., Lee, B., Park, S.Y., and Mirkin, C.A. (2008) Controlling the lattice parameters of gold nanoparticle FCC crystals with duplex DNA linkers. *Nano Lett.*, **8** (8), 2341–2344.

384 Xiong, H.M., van der Lelie, D., and Gang, O. (2009) Phase behavior of nanoparticles assembled by DNA linkers. *Phys. Rev. Lett.*, **102** (1). doi: 10.1103/physrevlett.102.015504

385 Macfarlane, R.J., Lee, B., Hill, H.D., Senesi, A.J., Seifert, S., and Mirkin, C.A. (2009) Assembly and organization processes in DNA-directed colloidal crystallization. *Proc. Natl. Acad. Sci. U.S.A.*, **106** (26), 10493–10498.

386 Rabani, E., Reichman, D.R., Geissler, P.L., and Brus, L.E. (2003) Drying-mediated self-assembly of nanoparticles. *Nature*, **426** (6964), 271–274.

387 Cheng, W.L., Campolongo, M.J., Cha, J.J., Tan, S.J., Umbach, C.C., Muller, D.A., and Luo, D. (2009) Free-standing nanoparticle superlattice sheets controlled by DNA. *Nat. Mater.*, **8** (6), 519–525.

388 Cheng, W.L., Park, N.Y., Walter, M.T., Hartman, M.R., and Luo, D. (2008) Nanopatterning self-assembled nanoparticle superlattices by moulding microdroplets. *Nat. Nanotechnol.*, **3** (11), 682–690.

389 Cheng, W.L., Hartman, M.R., Smilgies, D.M., Long, R., Campolongo, M.J., Li, R.P., Sekar, K., Hui, C.Y., and Luo, D. (2010) Probing in real time the soft crystallization of DNA-capped nanoparticles. *Angew. Chem. Int. Ed.*, **49** (2), 380–384.

390 Macfarlane, R.J., Lee, B., Jones, M.R., Harris, N., Schatz, G.C., and Mirkin, C.A. (2011) Nanoparticle superlattice engineering with DNA. *Science*, **334** (6053), 204–208.

391 Macfarlane, R.J., O'Brien, M.N., Petrosko, S.H., and Mirkin, C.A. (2013) Nucleic acid-modified nanostructures as programmable atom equivalents: forging a new "table of elements". *Angew. Chem. Int. Ed.*, **52** (22), 5688–5698.

392 Knorowski, C., Burleigh, S., and Travesset, A. (2011) Dynamics and statics of DNA-programmable nanoparticle self-assembly and crystallization. *Phys. Rev. Lett.*, **106** (21). doi: 10.1103/physrevlett.106.215501

393 Mladek, B.M., Fornleitner, J., Martinez-Veracoechea, F.J., Dawid, A., and Frenkel, D. (2012) Quantitative prediction of the phase diagram of DNA-functionalized nanosized colloids. *Phys. Rev. Lett.*, **108** (26). doi: 10.1103/physrevlett.108.268301

394 Jones, M.R., Macfarlane, R.J., Lee, B., Zhang, J.A., Young, K.L., Senesi, A.J., and Mirkin, C.A. (2010) DNA-nanoparticle superlattices formed from anisotropic building blocks. *Nat. Mater.*, **9** (11), 913–917.

395 Vial, S., Nykypanchuk, D., Yager, K.G., Tkachenko, A.V., and Gang, O. (2013) Linear mesostructures in DNA nanorod self-assembly. *ACS Nano*, **7** (6), 5437–5445.

396 Cutler, J.I., Auyeung, E., and Mirkin, C.A. (2012) Spherical nucleic acids. *J. Am. Chem. Soc.*, **134** (3), 1376–1391.

397 Auyeung, E., Cutler, J.I., Macfarlane, R.J., Jones, M.R., Wu, J.S., Liu, G., Zhang, K., Osberg, K.D., and Mirkin, C.A. (2012) Synthetically programmable nanoparticle superlattices using a hollow three-dimensional spacer approach. *Nat. Nanotechnol.*, **7** (1), 24–28.

398 Zhang, C., Macfarlane, R.J., Young, K.L., Choi, C.H.J., Hao, L.L., Auyeung, E., Liu, G.L., Zhou, X.Z., and Mirkin, C.A. (2013) A general approach to DNA-programmable atom equivalents. *Nat. Mater.*, **12** (8), 741–746.

399 Maye, M.M., Kumara, M.T., Nykypanchuk, D., Sherman, W.B., and Gang, O. (2010) Switching binary states of nanoparticle superlattices and dimer clusters by DNA strands. *Nat. Nanotechnol.*, **5** (2), 116–120.

400 Xiong, H.M., Sfeir, M.Y., and Gang, O. (2010) Assembly, structure and optical response of three-dimensional dynamically tunable multicomponent superlattices. *Nano Lett.*, **10** (11), 4456–4462.

401 Macfarlane, R.J., Jones, M.R., Lee, B., Auyeung, E., and Mirkin, C.A. (2013) Topotactic interconversion of nanoparticle superlattices. *Science*, **341** (6151), 1222–1225.

402 Felgner, P.L., Gadek, T.R., Holm, M., Roman, R., Chan, H.W., Wenz, M., Northrop, J.P., Ringold, G.M., and Danielsen, M. (1987) Lipofection: a highly efficient, lipid-mediated DNA-transfection procedure. *Proc. Natl. Acad. Sci. U.S.A.*, **84** (21), 7413–7417.

403 Zhang, J.M., Yang, P.L., and Gray, N.S. (2009) Targeting cancer with small molecule kinase inhibitors. *Nat. Rev. Cancer*, **9** (1), 28–39.

404 Reubi, J.C. (2003) Peptide receptors as molecular targets for cancer diagnosis and therapy. *Endocr. Rev.*, **24** (4), 389–427.

405 Schrama, D., Reisfeld, R.A., and Becker, J.C. (2006) Antibody targeted drugs as cancer therapeutics. *Nat. Rev. Drug Discov.*, **5** (2), 147–159.

406 Xing, H., Tang, L., Yang, X., Hwang, K., Wang, W., Yin, Q., Wong, N.Y., Dobrucki, L.W., Yasui, N., Katzenellenbogen, J.A., Helferich, W.G., Cheng, J., and Lu, Y. (2013) Selective delivery of an anticancer drug with aptamer-functionalized liposomes to breast cancer cells *in vitro* and *in vivo*. *J. Mater. Chem. B*, **1** (39), 5288.

407 Koltover, I., Salditt, T., Radler, J.O., and Safinya, C.R. (1998) An inverted hexagonal phase of cationic liposome–DNA complexes related to DNA release and delivery. *Science*, **281** (5373), 78–81.

408 Dan, N. (1998) The structure of DNA complexes with cationic liposomes-cylindrical or flat bilayers? *Biochim. Biophys. Acta, Biomembr.*, **1369** (1), 34–38.

409 Liang, H.J., Harries, D., and Wong, G.C.L. (2005) Polymorphism of DNA-anionic liposome complexes reveals hierarchy of ion-mediated interactions. *Proc. Natl. Acad. Sci. U.S.A.*, **102** (32), 11173–11178.

410 Boukhnikachvili, T., AguerreChariol, O., Airiau, M., Lesieur, S., Ollivon, M., and Vacus, J. (1997) Structure of in-serum transfecting DNA–cationic lipid complexes. *FEBS Lett.*, **409** (2), 188–194.

411 Pitard, B., Aguerre, O., Airiau, M., Lachages, A.M., Boukhnikachvili, T., Byk, G., Dubertret, C., Herviou, C., Scherman, D., Mayaux, J.F., and Crouzet, J. (1997) Virus-sized self-assembling lamellar complexes between plasmid DNA and cationic micelles promote gene transfer. *Proc. Natl. Acad. Sci. U.S.A.*, **94** (26), 14412–14417.

412 Pitard, B., Oudrhiri, N., Vigneron, J.P., Hauchecorne, M., Aguerre, O., Toury, R., Airiau, M., Ramasawmy, R., Scherman, D., Crouzet, J., Lehn, J.M., and Lehn, P. (1999) Structural characteristics of supramolecular assemblies formed by guanidinium-cholesterol reagents for gene transfection. *Proc. Natl. Acad. Sci. U.S.A.*, **96** (6), 2621–2626.

413 Ewert, K., Ahmad, A., Evans, H.M., Schmidt, H.W., and Safinya, C.R. (2002) Efficient synthesis and cell-transfection properties of a new multivalent cationic lipid for nonviral gene delivery. *J. Med. Chem.*, **45** (23), 5023–5029.

414 Ahmad, A., Evans, H.M., Ewert, K., George, C.X., Samuel, C.E., and Safinya, C.R. (2005) New multivalent cationic lipids reveal bell curve for transfection efficiency versus membrane charge density: lipid–DNA complexes for gene delivery. *J. Gene Med.*, **7** (6), 739–748.

415 Ewert, K.K., Evans, H.M., Bouxsein, N.F., and Safinya, C.R. (2006) Dendritic cationic lipids with highly charged headgroups for efficient gene delivery. *Bioconjugate Chem.*, **17** (4), 877–888.

416 Farago, O., Ewert, K., Ahmad, A., Evans, H.M., Gronbech-Jensen, N., and Safinya, C.R. (2008) Transitions between distinct compaction regimes in complexes of multivalent cationic lipids and DNA. *Biophys. J.*, **95** (2), 836–846.

417 Shirazi, R.S., Ewert, K.K., Leal, C., Majzoub, R.N., Bouxsein, N.F., and Safinya, C.R. (2011) Synthesis and characterization of degradable multivalent cationic lipids with disulfide-bond spacers for gene delivery. *Biochim. Biophys. Acta, Biomembr.*, **1808** (9), 2156–2166.

418 Ewert, K.K., Evans, H.M., Zidovska, A., Bouxsein, N.F., Ahmad, A., and Safinya, C.R. (2006) A columnar phase of dendritic lipid-based cationic liposome–DNA complexes for gene delivery: hexagonally ordered cylindrical micelles embedded in a DNA honeycomb lattice. *J. Am. Chem. Soc.*, **128** (12), 3998–4006.

419 Nakata, M., Zanchetta, G., Chapman, B.D., Jones, C.D., Cross, J.O., Pindak, R., Bellini, T., and Clark, N.A. (2007) End-to-end stacking and liquid crystal condensation of 6-to 20-base pair DNA duplexes. *Science*, **318** (5854), 1276–1279.

420 Bouxsein, N.F., Leal, C., McAllister, C.S., Ewert, K.K., Li, Y.L., Samuel, C.E., and Safinya, C.R. (2011) Two-dimensional packing of short DNA with non-pairing overhangs in cationic liposome–DNA complexes: from onsager nematics to columnar nematics with finite-length columns. *J. Am. Chem. Soc.*, **133** (19), 7585–7595.

421 Angelov, B., Angelova, A., Filippov, S.K., Narayanan, T., Drechsler, M., Stepanek, P., Couvreur, P., and Lesieur, S. (2013) DNA/fusogenic lipid nanocarrier assembly: millisecond structural dynamics. *J. Phys. Chem. Lett.*, **4** (11), 1959–1964.

422 Pozzi, D., Marchini, C., Cardarelli, F., Rossetta, A., Colapicchioni, V., Amici, A., Montani, M., Motta, S., Brocca, P., Cantu, L., and Caracciolo, G. (2013) Mechanistic understanding of gene delivery mediated by highly efficient multicomponent envelope-type nanoparticle systems. *Mol. Pharm.*, **10** (12), 4654–4665.